Winter 2005

Nonlinear dynamics of blood flow in simple microvascular networks

Fan Wu

University of New Hampshire, Durham

NONLINEAR DYNAMICS OF BLOOD FLOW IN
SIMPLE MICROVASCULAR NETWORKS

BY

Fan Wu

MS in Chemical Engineering (2002)

BS in Chemical Engineering (1999)

East China University of Science and Technology, Shanghai, China

DISSERTATION

Submitted to the University of New Hampshire

in partial fulfillment of

the requirements for the degree of

Doctor of Philosophy

in

Chemical Engineering

December, 2005

UMI Number: 3198017

INFORMATION TO USERS

The quality of this reproduction is dependent upon the quality of the copy
submitted. Broken or indistinct print, colored or poor quality illustrations and
photographs, print bleed-through, substandard margins, and improper
alignment can adversely affect reproduction.

In the unlikely event that the author did not send a complete manuscript
and there are missing pages, these will be noted. Also, if unauthorized
copyright material had to be removed, a note will indicate the deletion.
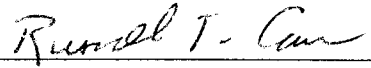
UMI®

UMI Microform 3198017
Copyright 2006 by ProQuest Information and Learning Company.
All rights reserved. This microform edition is protected against
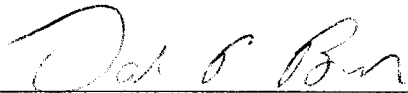unauthorized copying under Title 17, United States Code.

ProQuest Information and Learning Company
300 North Zeeb Road
P.O. Box 1346
Ann Arbor, MI 48106-1346

This dissertation has been examined and approved.
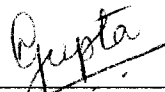
Russell T. Carr

Dissertation director, Dr. Russell T. Carr
Professor of Chemical Engineering

Dale P. Barkey

Dr. Dale P. Barkey
Professor of Chemical Engineering

Gupta

Dr. Nivedita Gupta
Assistant Professor of Chemical Engineering

John B. Geddes

Dr. John. B. Geddes
Associate Professor of Mathematics

Gregory P. Chini

Dr. Gregory P. Chini
Assistant Professor of Mechanical Engineering

2 December 2005

Date

DEDICATION

To My Parents and My Wife

ACKNOWLEDGEMENT

First, I am greatly indebted to my advisor, Dr. Russell T. Carr. It is his guidance and support that have allowed me to successfully complete my doctoral study. I am honorable to have an opportunity to enter the field of microcirculation under his direction.
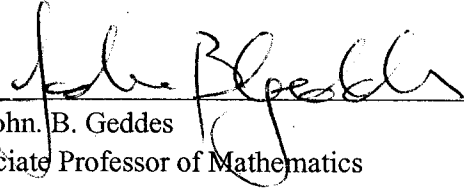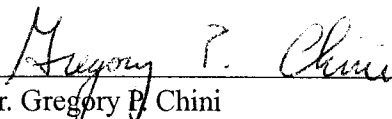
I would like to thank Dr. Dale P. Barkey, Dr. Gregory P. Chini, Dr. John. B. Geddes, Dr. Nivedita Gupta for serving on the dissertation committee and for their valuable advice and suggestion.

I am fortunate to have received generous help from Dr. Geddes. I have learned lots of useful mathematics knowledge through cooperation and communication with him.

I am grateful to have been kindly allowed to work in Dr. Gupta's Lab, where I have learned to make *in vitro* replicas of simple microvascular networks using soft lithography method.

I also thank Mr. Gabriel D. Withington, Ms. Yingyi Lao, Mr. Eric C. Beauregard, Mr. Michael O'Connor, Mr. Robert A. Coggon, and other people who have given me precious assistance during my project research.

I would like to thank Mr. John E. Newell for his technical assistance at experiment set-up.

I want to thank all members of faculty for their teaching and help during my study at the University of New Hampshire.

Finally, I would like to thank my wife, Xin Li, for her love, understanding and patience throughout these years.

TABLE OF CONTENTS

TABLE OF CONTENTS (CONTINUED)

LIST OF TABLES

LIST OF FIGURES

viii

LIST OF FIGURES (CONTINUED)

NOMENCLATURE

A	-	cross sectional area
A_i, C, C_i	-	constant coefficients
a, b, c, d	-	dimensionless parameters in stability analysis
d_i	-	diameter of branch i
F	-	fractional red cell flow
H	-	local hematocrit – volume fraction of red cells in blood
$H_{i\ (i=A,B,..)}$	-	hematocrit of blood flow in branch i
$H_{i(i=1,2,..)}$	-	hematocrit of blood flow in inlet i
H_D	-	discharge hematocrit
H_T	-	tube hematocrit
$\text{Im}(\lambda)$	-	imaginary parts of eigenvalues
l_i	-	length of branch i
m	-	number of exterior nodes
n	-	number of interior nodes
N_C	-	number of specified flows at external nodes
N_{com}	-	number of delays on a pathway
N_E	-	number of equations
N_F	-	degrees of freedom
N_p	-	number of pathways
N_{total}	-	total number of delays
N_V	-	number of variables
$\mathbf{N}^k$	-	k-dimensional vector space over the integers
$\mathbf{N}^1$	-	1-dimensional scalor space over the integers
p_i	-	plasma skimming parameters at node i
Q, Q^*	-	fractional blood flow
$\tilde{Q}, \tilde{Q}^*$	-	fractional blood flow at stead states
$Q_{i\ (i=A,B,..)}$	-	volumetric flow rate of blood flow in branch i
$Q_{i\ (i=1,2,..)}$	-	volumetric flow rate of blood flow in inlet i
R_i	-	hydraulic resistance in branch i
$\mathbf{R}^k$	-	k-dimensional vector space over the reals
$\mathbf{R}^1$	-	1-dimensional scalar space over the reals
$r, \text{Re}(\lambda)$	-	real parts of eigenvalues
s	-	dimensionless time variable
t	-	time variable
$T_{1/2}, T_{1/2}^*$	-	doubling time
v	-	local blood velocity
v_i	-	blood flow rate in branch i
y_q, y_h, y_{com}	-	specified ratios

Greek symbols

α, β	-	constant coefficients
β_i	-	the first derivative of viscosity with respect to the average hematocrit in branch i
$\tilde{\beta}_i$	-	β_i at steady states
η, μ	-	apparent viscosity
η_p	-	viscosity of plasma
η_r	-	relative apparent viscosity
μ_i	-	viscosity in branch i
ω	-	imaginary parts of eigenvalues
τ_i	-	time delay in branch i
$\tilde{\tau}_i$	-	time delay in branch i at steady states
θ_i	-	dimensionless time delay in branch i
$\tilde{\theta}_i$	-	dimensionless time delay in branch i at steady states
γ, δ	-	dimensionless time delays
λ	-	characteristic roots

ABSTRACT

NONLINEAR DYNAMICS OF BLOOD FLOW IN SIMPLE MICROVASCULAR NETWORKS

BY

Fan Wu

University of New Hampshire, December, 2005

It has been found that spontaneous oscillations of nodal pressures, hematocrit, and blood velocity can occur in microvascular networks in the absence of biological control. In this paper, both analytical and numerical methods have been used to investigate the nonlinear dynamics of microvascular blood flow in simple networks. First, the steady state solutions for the system are found. Then the governing coupled PDE's are transformed into state dependent time delay differential equations, DDE's. The DDE's are then linearized about a steady state and normalized.

The characteristic equation for the network is found by assuming the linearized DDE's have a nontrivial exponential solution. The solutions of the characteristic equation are also called the eigenvalues for the network dynamics at that steady state. It is known that the steady state is unstable when the real part of the rightmost eigenvalue is positive. Thus, a theoretical prediction of the stability of the blood flow in the network can be based on the rightmost eigenvalues. The analysis has been performed on the networks with two node topology and with three node topology.

Due to the nonlinearity of the characteristic equation, solutions are found numerically using a software package called "DDE-BIFTOOL". After the eigenvalues are found, predictions of the stability of steady states are compared to

direct numerical simulations for blood flow in the networks. Effects of physical parameters and inlet conditions on hemodynamics are investigated in the two node microvascular networks and the three node microvascular networks (2 inlets).

For the two node networks, the region of instability in parameter space is quite narrow. This means that experimental verification of spontaneous blood flow oscillations will be very difficult for the two node topology. The numerical results for the three node networks showed the three node system has instabilities over a much wider parameter ranges than the two node network. However, one of the most critical parameters, inlet hematocrit, is still quite high. This means such experiments are still very challenging.

Future work may involve continuing the search in wider parameter ranges and testing more complicated topologies to find realized conditions. Then *in vitro* experiments may be conducted to verify results of the linear stability analysis.

CHAPTER I

INTRODUCTION AND BACKGROUND

1.1 Purposes

The aim of this paper is to theoretically investigate the nonlinear dynamics of blood flow in simple microvascular networks via linear stability analysis. For a long time, the fluctuations in microvessel networks have been thought to result from biological actions, but recent numerical simulations suggest that spontaneous oscillations in microvessel networks could be caused by the nonlinear physical properties of the systems with no biological controls. (Kiani *et al.*, 1994; Carr and LeCoin, 2000)[1, 2] However, the underlying mechanisms for the oscillations are still unclear, motivating further theoretical studies of this phenomenon. This paper investigates the nonlinear dynamics of blood flow by combining analytical and numerical approaches.

A computational model is formulated, which consists of a set of partial differential equations and initial and boundary conditions. A linear stability analysis around steady-state solutions of the mathematical model is performed. The stability results can be utilized to predict the nonlinear dynamic behavior of the systems. The predictions can be further verified in future *in vitro* experimental work, which can be conducted in replicas of simple microvascular networks. Here, simple networks include the two node network, three node network or more complex ones. Necessary conditions for the oscillations are considered. The effects of physical parameters on the dynamic behavior are also investigated.

1

1.2 Rheological Properties of Blood Flow

1.2.1 Blood Composition and Rehology

In vivo blood can be regarded as a suspension of cells in fluid. The fluid portion is named plasma that is nearly 90% water and 10% solutes, such as proteins, glucose, minerals, and other substances. The cellular portion consists of different types of cells and is divided into two major classifications, erythrocytes and leukocytes, which are also called red blood cells (RBCs) and white blood cells (WBCs) respectively. (McCall and Tankersley, 2002)[3] Typical values of red blood cells, plasma, and whole blood are 1125 kg/m^3, 1025 kg/m^3, and 1056 ~ 1066 kg/m^3 respectively.[4] In a normal adult body, RBCs are the most numerous cells in blood (4.5 ~ 5 million/cm^3 of blood), and compared with the number of WBCs (5,000 ~ 10,000/cm^3 of blood), we neglect the effects of WBCs during *in vitro* rheological studies of blood.

In microcirculation systems consisting of tubes < 0.3mm diameter, non-uniform distribution of the red cells was observed, which intend to migrate toward tube axis. (Goldsmith *et al.*, 1989)[5] This non-uniform distribution of RBCs in microvessels leads to blood rheological characteristics, including the Fåhraeus effect, the Fåhraeus-Lindqvist effect, and plasma skimming. Here, the microcirculation comprised microvessels including arterioles (10 to 100 microns), venules (< 100 microns), and capillaries (> 5 microns).

Some researchers have tried to explain the redistribution of the red blood cells in microvessels by considering fluid mechanical mechanisms. (Fung, 1969; Lew and Fung, 1970; Goldsmith *et al.*, 1971)[6,7,8] It was found that fluid stresses play an important role in a dilute solution of neutrally buoyant particles, which drive deformable particles like red blood cells move laterally toward the tube axis.

2

(Goldsmith *et al.*, 1989)[5] However, particle collisions are probably more important in concentrated solutions. Goldsmith investigated interactions between red cells and rigid walls in tube flow, and discovered inward immigration of red blood cells take places over a very wide range of Reynolds number and results in cell-free layers close to walls, but when the cells are crowded, the collisions and interactions among red blood cells lead to their sideways and radial movements. Goldsmith further analyzed the sideways movements as Brownian motion of small particles in suspension and calculated a dispersion coefficient for RBCs, which is equal to 3.9×10^{-10} cm^2/sec. (Goldsmith, 1971)[8] Based on Goldsmith's observation, Carr modeled the dispersion of blood cells in microvessels as a diffusion process, and found that red cells frequently exhibit asymmetric distributions in the microcirculation. (Carr, 1989)[9]

1.2.2 Fåhraeus Effect

The Fåhraeus effect is used to name a phenomenon that plasma and red blood cells move along vessels with a different average velocity in the blood circulation (Fåhraeus, 1929).[10] The tube and discharge hematocrits are defined respectively to illustrate this effect as follows, where H denotes local hematocrit and A refers to a cross sectional area of the tube.

● Tube hematocrits

$$H_T = \frac{\int_A H(A)dA}{\int_A dA} \tag{1.2.1}$$

● Discharge hematocrits

$$H_D = \frac{\int_A H(A)v(A)dA}{\int_A v(A)dA} \tag{1.2.2}$$

3

The tube hematocrit is defined as the volumetric proportion of RBCs in a vessel, while the discharge hematocrit is defined as the ratio of RBC flow rate to the whole blood flow rate. In vessels with large diameters, the RBCs (about 7 to 8 microns in diameter) are comparatively small, so the tube and discharge hematocrits have little difference. For smaller blood vessels, RBCs are excluded from the wall and accordingly flow in the center region of the vessels. Since the cells tend to flow in the faster flow regions, the discharge hematocrit is greater than the tube hematocrit. For capillaries with diameter near to the RBC's, plasma and RBC have approximately the same velocity since almost the whole vessel section is occupied by the RBC.

1.2.3 Fåhraeus-Lindqvist Effect

The Fåhraeus-Lindqvist effect refers to the functional dependence of the apparent viscosity on hematocrit and vessel diameter (Fåhraeus and Lindqvist, 1931)[11]. In small bore vessels, cells tend to flow in the regions closer to the axis, plasma acts as a lubricating layer near the wall and thus the apparent viscosity of the blood flow is reduced in the tube. Both cell and tube diameters determine the thickness of the lubricating layer. Blood is a suspension of cells in fluid, and the blood viscosity depends on hematocrit, i.e. the concentration of the suspended RBCs. The above causes lead to the Fåhraeus-Lindqvist effect.

Several empirical correlations are available based on *in vitro* tube flow measurements (Kiani and Hudetz, 1991; Pries *et al.*, 1992)[12,13]. Pries *et al.* have also published an empirical *in vivo* viscosity correlation via indirect *in vivo* experiments (Pries *et al.*, 1994)[14]. Both the Pries's *in vitro* and the Pries's *in vivo* viscosity models are adopted in this paper and listed below.

4

- Pries's *in vivo* viscosity model:

$$\eta_r = (\frac{d}{d-1.1})^2[1+(\eta_{0.45}^* -1)\frac{(1-H_D)^C -1}{(1-0.45)^C -1}(\frac{d}{d-1.1})^2]$$

$$C = \frac{1}{1+10^{-11}d^{12}} + (\frac{1}{1+10^{-11}d^{12}} -1)(0.8+e^{-0.075d})$$

$$\eta_{0.45}^* = 6e^{-0.085d} +3.2-2.44e^{-0.06d^{0.645}}$$ (1.2.3)

- Pries's *in vitro* viscosity model:

$$\eta_r = 1+(\eta_{0.45}^* -1)\frac{(1-H_D)^C -1}{(1-0.45)^C -1}$$

$$C = \frac{1}{1+10^{-11}d^{12}} + (\frac{1}{1+10^{-11}d^{12}} -1)(0.8+e^{-0.075d})$$

$$\eta_{0.45}^* = 220e^{-1.3d} +3.2-2.44e^{-0.06d^{0.645}}$$ (1.2.4)

In the above two correlations, η_r is the relative apparent viscosity. The apparent viscosity is

$$\mu = \eta_r \eta_p.$$ (1.2.5)

η_p is the viscosity of plasma (1.3 – 1.7 cp). H_D is the hematocrit in the vessel and

d is the diameter of the vessel with a unit of "micron". Once the apparent viscosity

is obtained, assuming Poiseuille flow in a blood vessel, the hydraulic resistance of a

vessel derived from the Hagen-Poiseuille equation (Bird *et. al.*, 2002)[15] is

$$R = \frac{\Delta P}{Q} = \frac{128l\mu}{\pi d^4},$$ (1.2.6)

where R and l denote hydraulic resistance and length of the vessel respectively,

ΔP is the pressure drop over the vessel and Q is the flow rate of blood in the vessel.

5
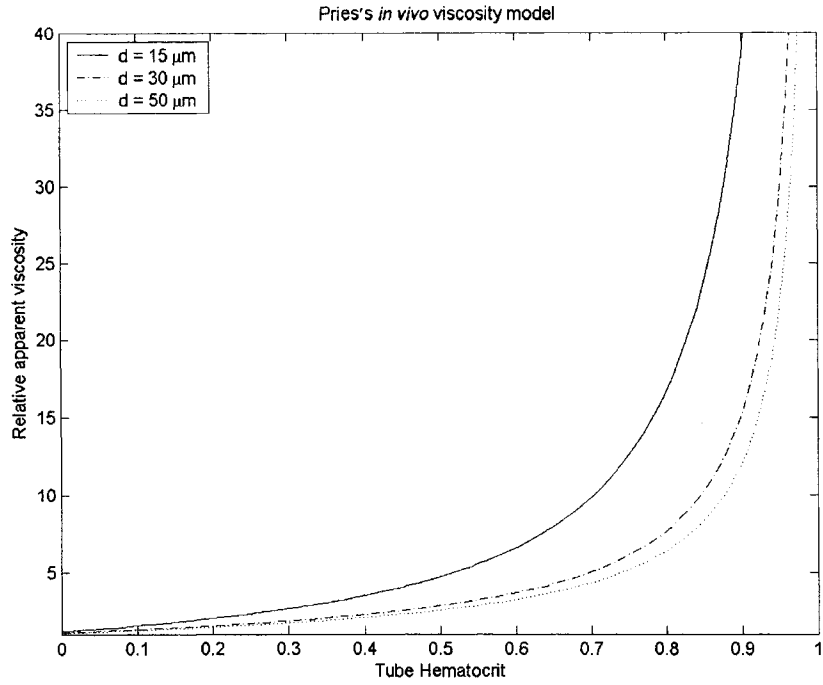
Figure 1.1   Pries's *In Vivo* Viscosity Model.
Curves of relative apparent viscosity versus hematocrit are plotted with three
different tube diameters.
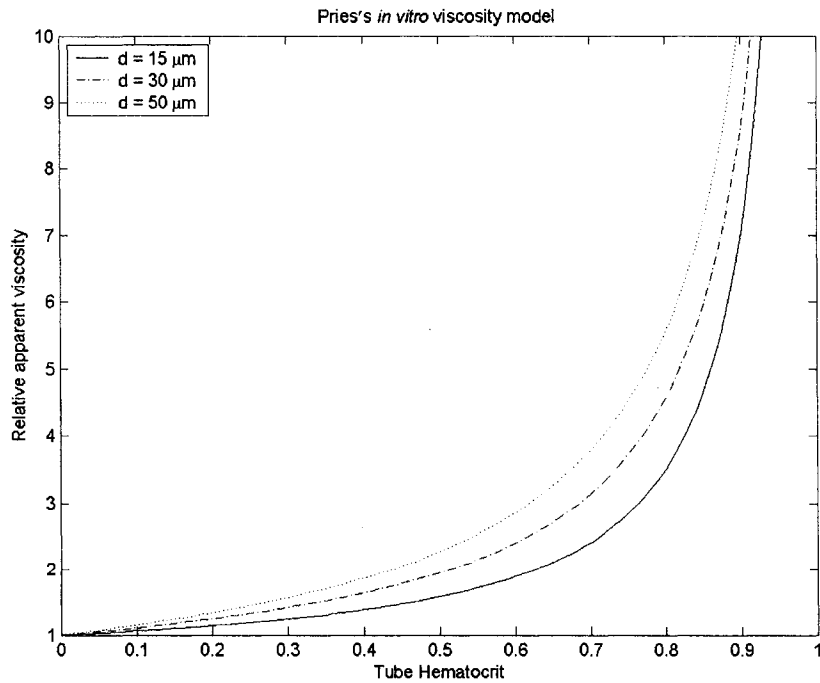
Figure 1.2   Pries's *In Vitro* Viscosity Model.
Curves of relative apparent viscosity versus hematocrit are plotted with three
different tube diameters.

6

1.2.4 Plasma Skimming Phenomena

Plasma skimming is a rheological peculiarity of microcirculation. This phenomenon was first stated in Krogh's book (Krogh, 1929)[16]. At a diverging node, if a downstream branch receives a higher fraction of flow, it receives an even higher fraction of RBCs. The phenomenon is related closely to the cell depleted region near the vessel wall again. Some researchers have made a thorough investigation into the underlying mechanism (Cokelet, 1986; Carr, 1984; Pries et al., 1989)[17,18,19]. Briefly, the blood flow splits at the bifurcation and forms a separation surface. If the flow split is not half to half, the cell depleted layer causes the blood to flow into daughter branches in different proportions (see Figure 1.3).
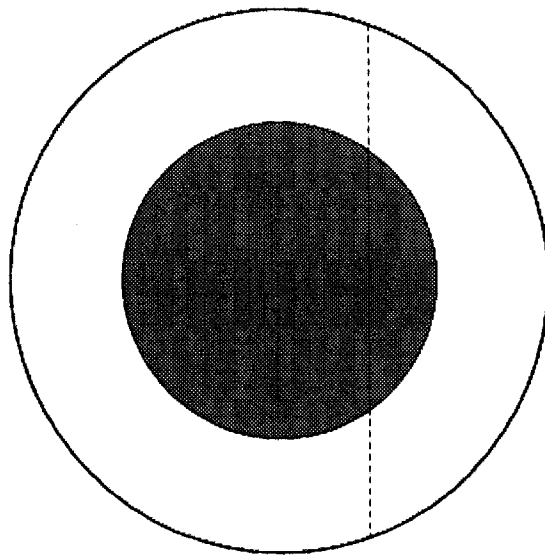
Figure 1.3 Cross-Section of the Parent Vessel Far Upstream from the Bifurcation. The shadow region represents a core of high hematocrit blood. The gap area is the cell depleted region.

Some reasonable models are available now. In this paper, two plasma skimming models are used, a linear model (Fenton et al., 1985)[20] and a logit model (Dellimore et al., 1983)[21]. Both models are given below, with F, Q denoting the fractional RBC flow and the fractional volumetric flow entering a daughter branch respectively,

7

and p denoting the plasma skimming parameter. Graphical illustrations of the two models are shown in Figure 1.4.

- The linear plasma skimming model:

$$F = pQ + (1-p)/2$$

$$p = \frac{1}{1.4 - \sqrt{\varepsilon}}; \quad \varepsilon = d_{RBC}/d. \tag{1.2.7}$$

Here d_{RBC} is the diameter of a mature red blood cell (7 ~ 8 microns), and d is the diameter of the parent branch. The plasma skimming parameter p must be greater than or equal to 1 according to Fenton *et al.*.

- The logit plasma skimming model:

$$F = \frac{Q^p}{Q^p + (1-Q)^p}. \tag{1.2.8}$$

Generally, a reasonable value of p is between 1 and 3.
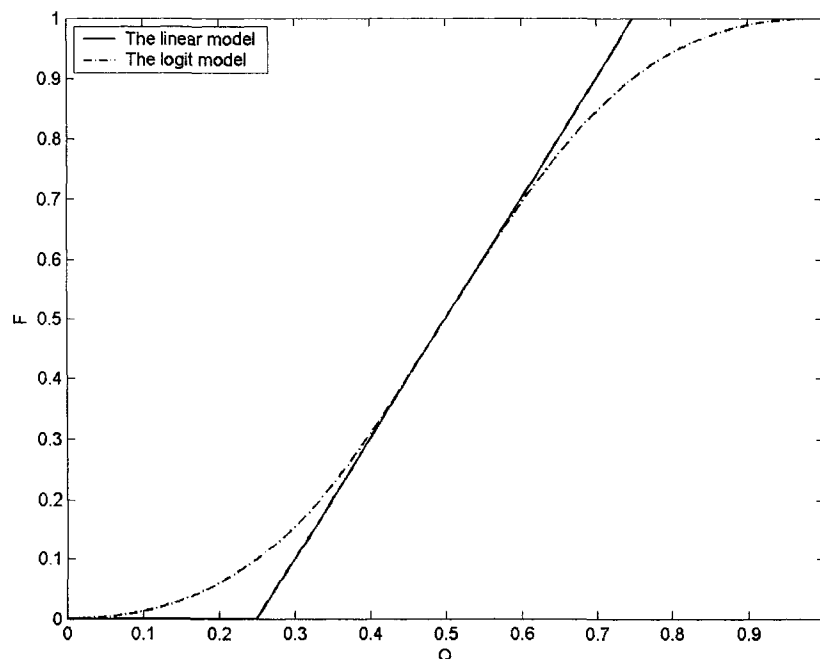
Figure 1.4   Curves of Plasma Skimming Models when p = 2.0.

8

1.3 Oscillation Phenomena in Microcirculation Systems

1.3.1 Spontaneous Oscillations in Large Microvascular Networks

It has been noted for a long time that the temporal oscillations in blood flow exist in microcirculation. Based on observations, researchers have sought the causes of the fluctuations in blood flow parameters, such as hematocrit, velocity, and pressure etc.. Special techniques are required to measure those parameters. The dual slit device was invented in 1960s (Wayland and Johnson, 1967)[22], and this technique was shortly used shortly thereafter to measure RBC velocities *in vivo*. Another widely used technique of velocity measurement is laser Doppler velocimetry (Rodgers *et al.*, 1984)[23]. The servo-nulling micropipette pressure measuring system can be used to monitor pressure variability *in vivo* (Wiederhielm *et al.*, 1964)[24]. It is reported recently that transcranial Doppler ultrasound has been extensively used to study cerebral hemodynamics (Giller and Mueller, 2003)[25]. All these methods show evidence of the temporal variability of blood flow parameters in the microcirculation.

Johnson and Wayland applied the dual slit method and reported that 7 out of 27 capillaries displayed periodic flow patterns in the cat mesentery, and the dynamics found in microvessels include steady flow, periodic flow, fluctuating aperiodic flow, and intermittent flow (Johnson and Wayland, 1967)[26]. They also reported that changes in the inlet flow rate changed the dynamics considerably.

Instead of focusing on a single blood vessel to observe oscillations, the laser Doppler velocimeter can generate results by averaging signals from several vessels. Rodger *et al.* applied the velocimeter to measure blood flow in the forearm skin of sickle cell and control patients. Periodic flow patterns were found in sickle cell patients without crisis, which was explained as a compensatory mechanism for the

9

increased viscosity of sickle cell blood (Rodgers et al., 1984)[15].

Weiderhielm's pressure measuring system has been applied in various living animals to track the microvessel pressure (Weiderhielm et al.,1964; Intaglietta et al., 1969; Zweifach, 1974; Slaaf et al., 1987)[24,27,28,29]. All the experimental records display temporal fluctuations. The frequencies of the observed oscillations range from about 300 cycles per minute (Zweifach, 1974)[20] to 0.14 cycles per minute (Slaaf et al., 1987)[21].

An advantage of Doppler ultrasound method is its excellent temporal resolution, thus it has been widely used to validate mathematical model of interactions between blood velocity in the cerebral microvessels and blood pressure. The time analyses exhibited the non-linear and oscillatory behavior of cerebral hemodynamics, and the computer models produced spontaneous oscillations similar to observed phenomena in humans (Giller and Mueller, 2003).

One possible cause of these temporal fluctuations is respiration rhythms and heart beat rates. Weiderhielm has identified the range of observed oscillation is from ~300 cycles/min to ~0.14 cycles/min. Some of the oscillations are found to be related to pulse of the heart beat (120 to 300 cycles/min), while breathing rhythms may be closely connected to some frequencies around 45 cycles/min. Other lower frequencies from 6 cycles/min to 0.14 cycles/min may be caused by temporal variations in vessel diameters.

Variations in vessel diameters, i.e., vasomotion, can be observed directly in in vivo experiments (Colantuoni et al., 1984; Slaaf et al., 1987; Parthimos et al., 1996)[30,31,32], and can also be characterized in vitro using isobaric and isometric methods (Hessellund et al., 2003)[33]. Colantuoni et al. found vasomotion frequencies of 2.7 cycles/min in arteries and of 9.5 cycles/min in terminal arterioles. Slaaf and

10

his collegues noted that the frequencies range from 5 to 32 cycles/min in first order side branch arterioles (Slaaf *et al.*, 1987)[31]. Meyer *et al.* found a fundamental frequency of 20 cycles/min in terminal arterioles by examining rabbit tenuissimus muscle (Meyer *et al.*, 1987)[34].

Since the range of reported vasomotion frequencies coincides with the range of observed oscillation frequencies of blood pressure, it seems plausible to attribute the temporal fluctuations in the microcirculation to the vasomotion. However, by performing a nonlinear analysis of fluctuations in RBC velocity and arteriolar diameters in anaesthetized rat, Parthimos *et al.* reported that both correlation dimensions and largest Lyapunov exponents were higher for RBC velocity than diameter variations, thus hinting that different mechanisms regulates the microvascular flow (Parthimos *et al.*, 2004)[35]. Some researchers have been focused on the relationship between the fluctuations and biological control signals, such as the release of NO (Letinene *et al.*, 1998)[36], pressure, oxygen concentration, tension, temperature, etc. However, the numerical research strongly indicates the oscillatory phenomena are not only due to the biological control, but also due to the rheological properties, geometry and topology of the microvascular networks.

1.3.2 Numerical Simulations for Microvascular Networks

Kiani *et al.* presented a simulation model based on the rheological properties and applied the model to microvascular networks that mimicked a part of *in vivo* mesentery networks (Kiani *et al.*, 1994)[1]. The model contained information about plasma skimming, the Fåhraeus effect, the Fåhraeus-Lindqvist effect, and network topology and geometry. Amazingly, even though no biological control was considered in the model and the boundary conditions were kept constant, the results

11

showed that about 30% of the vessels exhibited spontaneous oscillations in blood flow parameters, such as pressure, hematocrit, and flow rate.

One possible cause of the oscillation is the numerical instability, but Kiani *et al.* found that the results were not changed when smaller time step was used, thus the oscillatory behavior may be explained as an intrinsic property of a nonlinear system (Kiani *et al.*, 1994)[1]. Nonlinear systems can exhibit various dynamic behaviors, such as fix points, limit cycle, and chaos etc. (Moon, 1992; Strogatz, 2000)[37,38]. In fact, Fung pointed out that flow fluctuations in the microcirculation might be a result of either physical properties or physiological variables (Fung, 1973)[39]. In his paper, Fung also claimed the significant influence of network topology on the dynamic behaviors, which has been examined by a series of work done by Pries and his coworkers (Pries *et al.*, 1986; Pries *et al.*, 1995; Pries *et al.*, 1996)[40,41,42].

Since Kiani *et al.* investigated large networks containing between 383 and 913 vessel segments, they were unable to identify the cause of the oscillations. Carr and LeCoin extended the computational research by focusing on small networks (less than 15 vessel segments) and their results provided further understanding of underlying mechanisms of these spontaneous oscillations. (Carr and LeCoin, 2000)[2] The simulation model consisted of nonlinear coupled partial differentiation equations (PDE's) with boundary and initial conditions. Carr and LeCoin reported that possible dynamic behaviors in small microvascular networks include steady states, sustained oscillations and damped oscillations.

Carr and LeCoin's work discussed some necessary features for oscillations to take place: the Fåhraeus-Lindqvist effect and plasma skimming are necessary, but the Fåhraeus effect is not necessary. Instead of using an *in vitro* viscosity model as Kiani *et al.* did, Carr and LeCoin applied the Pries's *in vivo* viscosity model and still

12

observed oscillations in their simulations. Even when a linearized viscosity law was used, the oscillation still occurred, so it seems that the form of the viscosity law is not crucial. Plasma skimming was found to influence both the amplitude and the frequency of oscillations. If no plasma skimming was included, oscillations did not occur. The Fåhraeus effect was found to impact the frequency of the oscillation, but even when the Fåhraeus effect was excluded, the qualitative features of the dynamic behaviors were not altered.

Carr and LeCoin also found both geometry and topology of the networks were of significance to determine the dynamic behaviors (Carr and LeCoin, 2000)[2]. However, the interactions between the geometrical and topological properties and the dynamics were too complicated to be understood well. According to Carr and LeCoin's paper, the simplest microvascular network to exhibit oscillations was a four node network with three inlets. Due to the considerably time-consuming property of the simulation program and high dimension of the system, it was impractical to run it to discover boundaries of oscillations in spaces of physical parameters.

Therefore, it is reasonable to focus on simpler networks where oscillation can occur. Based on these simple networks, some mathematical techniques like stability analysis may be applied to discover the physical parameters that affect the oscillatory behavior, and to further identify the necessary conditions that initiate the oscillations. Such small networks might be constructed by using techniques like soft lithography (Duffy et al., 1998; Xia and Whitesides, 1998; Clarner, 2000)[43,44,45], and then some in vitro experiments may be conducted to verify the corresponding numerical results.

13

CHAPTER II

STABILITY ANALYSIS OF BLOOD FLOW IN SIMPLE MICROVASCULAR NETWORKS

2.1 Topological Properties of the Simple Networks

Obviously, the simplest networks include two node networks with one inlet, three node networks with two inlets or outlets, four node networks with an intersecting branch, four node networks with three inlets. The illustrations of these networks are presented in Figure 2.1.

Topology 1

Topology 2

Topology 3
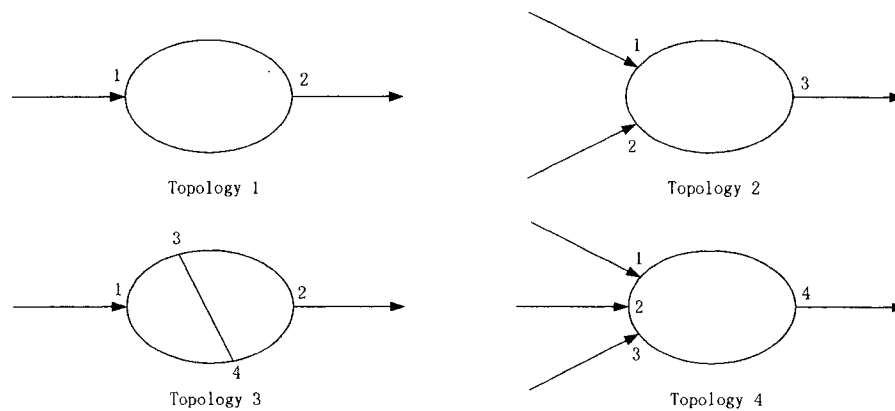
Topology 4

Figure 2.1 Four Topologies for Simple Microvascular Networks.
(Topology 1: two node networks; Topology 2: three node networks with two inlets; Topology 3: four node networks with an intersecting branch; Topology 4: four node networks with three inlets.)

The two node topology shown in Figure 2.1 consists of one inlet, one outlet, and two branches. While blood flows through the network, it diverges at the inlet junction and joins together at the outlet junction.

14

For the three node topology, it has two inlet junctions, and divergence can happen at either of them at one time. The node pressures at the two inlet junctions determine which one is a diverging node. When the pressure at node 1 is higher, divergence occurs, and blood flows from node 1 to node 2. A special case is that the pressures are equal at both inlet junctions, and then there is no flow in the branch between them. To conclude, there are always one divergence and two convergences taking place in the three node network except when no blood flows in the middle branch.

The four node topology with an intersecting branch possesses a more complicated situation – divergence may take place at three junctions. The inlet junction is always a diverging node, but only one of the two interior junctions can be a diverging node at one time, and pressures need to be computed to determine which the diverging one is. Therefore, two divergences exist for this type of network, and it is possible for a reverse flow to happen in the intersecting branch.

The fourth topology in Figure 2.1 is another type of four node network, which processes three inlet junctions. Different from the former one, there is only one diverging node existing among the three inlet junctions in the four node network.

From the above brief descriptions, we notice that different topological structure may mean distinct dynamics characteristics accordingly. However, all four networks have at least one diverging node where plasma skimming can take place, so it is still possible for spontaneous oscillations to occur in these simple networks under certain conditions.

15

2.2 Complexity Measure and Delays

To mathematically model a system, it is necessary to know its degree of freedom, i.e., how many state-dependent variables need to be included in the governing equations. Also, the number of time delays in the system are of great interest since they may appear somewhere in the model. However, if the studied system possesses more complicated topologies, it may not be easy to determine the degrees of freedom and the number of time delays a priori. This section presents an initial discussion on general ways to analyze complexity and delays of a given system.

Some definitions are made here. A network may possess m exterior nodes - which are defined as junctions connecting inlet or outlet branches, and n interior nodes - which are defined as junctions joined by branches excluding inlets or outlets. Each node connects three branches.

2.2.1 Complexity Measure

In microvascular networks, the distribution of blood flow rates determines the hematocrit of blood entering branches at each node. The average hematocrit influences resistance in each branch, which changes the distribution of flow rates in turn. Therefore, the flow rates are state-dependent variables, and the degree of freedom of a system can be discovered by combining mass balance and topology analysis.

Suppose the degree of freedom is denoted as N_F, which equals to the minimum number of state-dependent variables required to decide the state of the system. The

16

variables may be solved through N_F relations, for instance, momentum balances.

When status of blood flow in each branch is determined, status of a whole microvascular network is known. Thus, the number of total variables is equal to the total number of branches. Note that each node connects three branches. If the total number of the nodes are tripled, each branch except an inlet or an outlet is double counted, thus the number of total variables

$$N_V = [3(m + n) + m]/2 = 2m + 3n/2,$$ (2.2.1)

Mass balances are conducted at each node, so the number of the total equations

$$N_E = m + n.$$ (2.2.2)

Let N_C denote the specified flows at external nodes, it is easily found that

$$N_C = m - 1.$$ (2.2.3)

Therefore, the degrees of freedom can be determined from

$$N_F = N_V - N_E - N_C = n/2 + 1,$$ (2.2.4)

which means N_F state-dependent variables are unknown on the basis of mass balance, and N_F additional functional relationships are required to determine the status of the system.

The result is somewhat surprisingly neat, which means the degree of freedom is only related to the number of the interior nodes. To verify the above conclusion, some examples are examined.

- Example 1: The two node network

For the topology 1, $n = 0$, so $N_F = 0/2 + 1 = 1$, which means one state-dependent variable is needed to determine the system status. Obviously, if a flow rate in one

17

branch or a flow rate ratio is determined, the system status is known.

- Example 2: The three node network with two inlets

For the topology 2, $n = 0$, so $N_F = 0/2 + 1 = 1$, and therefore one state-dependent variable is required. It is consistent with the fact that a flow rate in one branch or a flow rate ratio suffices to determine the status of the whole system.

- Example 3: The four node network with a middle branch

For the topology 3, $n = 2$, so $N_F = 2/2 + 1 = 2$, which means two state-dependent variable is needed to determine the system status. For instance, if two flow rate ratios are determined, the system status is known.

- Example 4: The four node network with three inlets

For the topology 4, $n = 0$, so $N_F = 0/2 + 1 = 1$, which means one state-dependent variable is needed to determine the system status. By comparing this example with the four node network in Example 3, it is evident that although total nodes is equal, but the complexity of the two four node networks is entirely different.

2.2.2 Number of Delays of the Systems

Obviously, each branch represents a delay, which means the blood flow at the exit contains the same information as the blood flow at entrance some time ago. Since on each pathway, certain combinations of the delays on adjacent branches generate new delays, the number of delays is closely related to pathways the blood flows take in the networks. Therefore, the possible pathways need to be found to determine the total delays of the system.

18

There are several basic rules to obey when determining the pathways.

1) Each node must not be convergence and divergence;

2) A closed loop for blood flow must not happen in the pathways;

3) A pathway must start from an inlet and end at an outlet.

Suppose in a network, there are N_p pathways and k_i nodes on the ith pathway. Obviously, there are $k_i - 1$ segments on the ith pathway. The number of the combined delays on the ith pathway is computed by

$$N_{com} = \sum_{j=1}^{k_i-1} j - (k_i - 1) = (k_i - 1)(k_i / 2 - 1) \qquad (2.2.5)$$

The total number of branches can be computed using Eq.(2.2.1). The number of total delays is equal to the sum of the total number of branches and the total number of the combined delays

$$N_{total} = 2m + 3n / 2 + \sum_{i=1}^{N_p} (k_i - 1)(k_i / 2 - 1) . \qquad (2.2.6)$$

Some examinations can be performed on the topologies in Figure 2.1. For topology 1, there are two branches, two pathways, and two nodes on each pathway, so the number of delays is equal to two, i.e. each delay on each branch. For the topology 2, there are three branches, two pathways, one pathway possess two nodes, and the other possesses three nodes, so the system has three delays. Likewise, it is computed that ten delays exist for the topology 3. The case of topology 4 is a little more complex, and there are seven or six delays depending at which node the divergence takes place.

19

2.3 Procedures of Stability Analysis around Steady States

Determining the stability of a network with simple topology is an intriguing issue, which is useful in discovering the underlying mechanism of the oscillation phenomena. The simple topologies studied in this paper include a two node arcade network and a three node network with two inlets. Although these networks have different topologies, general analysis procedures can be summarized as following (Wu *et al.*, 2005 (1); Wu *et al.*, 2005 (2); Carr *et al.*, 2005; Geddes *et al.*, 2003)[46,47,48,49]:

1) First, the governing equations are established as coupled partial differential equations (PDE's) with boundary and initial conditions, and then PDE's are transformed into state dependent delay differential equation(s) DDE('s) with threshold conditions.

2) Second, possible steady state solutions of the equation(s) are found numerically.

3) Then, the DDE('s) is(are) linearized about steady states and normalized, and the characteristic equation(s) can be obtained based on the DDE('s) after manipulations.

4) Finally, numerical methods are applied to find rightmost roots of the characteristic equation(s), i.e. the rightmost eigenvalues, at that steady state. Thus the local stability around the steady states can be predicted theoretically according to the sign of the real part of the rightmost eigen values – positive real part means the steady state is unstable, or vice versa (Class and Mackey, 1988)[50].

In the following sections, each step of the procedure is explained with examples provided for the two node network (see Figure 2.2) and the three node network (see

Figure 2.3). The related mathematical derivations of the characteristic equations are

lengthy and tedious, and they are included in the appendixes.
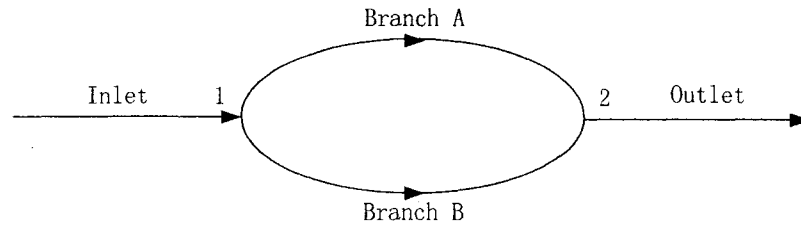
Figure 2.2   An Illustration of a Two Node Network
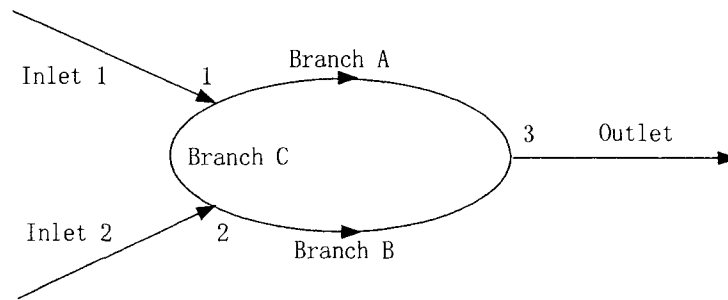
Figure 2.3   An Illustration of a Three Node Network with Two Inlets

21

2.4 Governing Equations

In each vessel in the networks, a convection equation can be obtained via a red cell balance done by Carr and LeCoin (Carr and LeCoin, 2000)[2],

$$\frac{\partial H_i}{\partial t} + v_i \frac{\partial H_i}{\partial x} = 0 , \qquad (2.4.1)$$

where H_i is the hematocrit in branch i, and v_i is the velocity of the blood flow in branch i. By neglecting the Fåhreous effect, the distinction between tube hematocrit and discharge hematocrit is lost in Eq.(2.4.1), and accordingly the bulk velocity of the blood flow is equal to red blood cell velocity. In the governing equations, the hematocrit is a continuous function of position and time, which does not approximate the discrete nature of RBC flow over short time very well. However, since the discrete nature of the flow is to be eliminated over longer time scales, the model provides a good description (Carr and LeCoin, 2000)[2].

Since all the blood in a branch at any time corresponds to the blood entering it a certain time ago, the certain time is defined as a delay time τ_i for the branch i so that

$$H_i(l_i, t) = H_i(0, t - \tau_i) , \qquad (2.4.2)$$

where τ_i is a function of time and can be determined from the following integral, and d_i and l_i are diameters and lengths of branch i respectively

$$l_i = \int_{t - \tau_i(t)}^{t} v_i(s)ds . \qquad (2.4.3)$$

Integrating $H_i(x_i, t_i)$ over the length of the branch by using equation Eq.(2.4.1), and use $\bar{\bar{H}}_i$ to denote the average hematocrit in branch i at a time, $\Rightarrow$

$$\frac{d\bar{\bar{H}}_i}{dt} = \frac{v_i}{l_i}[H_i(0, t) - H_i(l_i, t)] \qquad (2.4.4)$$

22

$$\frac{d\bar{H}_i}{dt} = \frac{v_i}{l_i}[H_i(0,t) - H_i(0,t-\tau_i)].\qquad(2.4.5)$$

From a plasma skimming model and a mass balance

$$H_i(0,t) = H_i(Q_i(t), par),\qquad(2.4.6)$$

where Q_i denotes a dimensionless flow rate ratio and *par* denotes physical parameters, such as plasma skimming model parameters, inlet or outlet flow rates, inlet or outlet hematocrits, branch diameters, and branch lengths.

From a mass and momentum balance

$$Q_i(t) = Q_i(R_1(\bar{H}_1(t)), ..., R_m(\bar{H}_m(t)), par),\qquad(2.4.7)$$

where R_i can be represented using Eq.(1.2.4) combined with a certain viscosity model.

From the chain rule (Kreyszig, 1993)[51],

$$\frac{dQ_i}{dt} = \sum_{k=1}^{m} \frac{\partial Q}{\partial R_k} \frac{dR_k}{d\bar{H}_k} \frac{d\bar{H}_k}{dt}.\qquad(2.4.8)$$

Since $dR_k / d\bar{H}_k$ can be computed from Eq.(1.2.4) combined with a viscosity function and $d\bar{H}_i / dt$ is available from Eq.(2.4.5), Eq.(2.4.8) can be transformed to the DDE's, which are also called retarded functional differential equations (RFDE's) in some mathematics references (Hale and Lunel, 1993)[52]. This kind of DDEs is called threshold type delay differential equations due to additional threshold conditions $l_i = \int_{-\tau_i(t)}^{t} v_i(s)ds$ (Luzyanina et al., 2001)[53].

Illustrations of transforming the governing PDE's to DDE's in the simple networks are shown as follows.

23

- The two node network

From Eq.(2.4.5)

$$\frac{d\bar{H}_A}{dt} = \frac{4Q_1 Q(t)}{\pi d_A^2 l_A}[H_A(0,t) - H_A(0,t-\tau_A)]$$

$$\frac{d\bar{H}_B}{dt} = \frac{4Q_1(1-Q(t))}{\pi d_B^2 l_B}[H_B(0,t) - H_B(0,t-\tau_B)], \qquad (2.4.9)$$

where τ_A, τ_B are defined by

$$l_A = \int_{t-\tau_A(t)}^{t} v_A(s)ds = \frac{4Q_1}{\pi d_A^2}\int_{t-\tau_A(t)}^{t} Q(s)ds$$

$$l_B = \int_{t-\tau_B(t)}^{t} v_B(s)ds = \frac{4Q_1}{\pi d_B^2}\int_{t-\tau_B(t)}^{t}(1-Q(s))ds \qquad (2.4.10)$$

where $Q(t) = Q_A(t)/Q_1$, Q_1 is the inlet flow rate.

From a momentum balance,

$$\Delta P = Q_A R_A = Q_B R_B \qquad (2.4.11)$$

$$\Rightarrow Q(t) = \frac{R_B(t)}{R_A(t) + R_B(t)}. \qquad (2.4.12)$$

where R_A and R_B are hydraulic resistance of blood flow in branch A and branch B respectively.

Plug Eq.(2.4.12) into Eq.(2.4.8)

$$\frac{dQ}{dt} = -\frac{1}{(1+R_A/R_B)^2}\left[\frac{1}{R_B}\frac{dR_A}{dt} - \frac{R_A}{R_B^2}\frac{dR_B}{dt}\right] = \frac{Q}{R_B}\left[(1-Q)\frac{dR_B}{dt} - Q\frac{dR_A}{dt}\right] \qquad (2.4.13)$$

From Eq.(1.2.6)

$$\frac{dR_A}{dt} = \frac{128 l_A}{\pi d_A^4}\beta_A \frac{d\bar{H}_A}{dt}$$

$$\frac{dR_B}{dt} = \frac{128 l_B}{\pi d_B^4}\beta_B \frac{d\bar{H}_B}{dt}, \qquad (2.4.14)$$

24

where $\beta_A = \dfrac{d\mu_A}{d\bar{H}_A}$, $\beta_B = \dfrac{d\mu_B}{d\bar{H}_B}$.

From a plasma skimming model,

$$H_A(0,t) = H_1 \frac{F(Q(t))}{Q(t)}$$

$$H_B(0,t) = H_1 \frac{1-F(Q(t))}{1-Q(t)}, \tag{2.4.15}$$

where H_1 is the inlet hematocrit and F denotes the fractional RBC flow entering

branch A.

Combine Eq.(2.4.13), Eq.(2.4.14), Eq.(2.4.15), and Eq.(2.4.9)

$$\frac{dQ(t)}{dt} = \frac{4Q_1 H_1 d_B{}^4}{\pi l_B \mu_B(t)} Q(t)[(1-Q(t))^2 \frac{\beta_B(t)}{d_B{}^6}(\frac{1-F(Q(t))}{1-Q(t)} - \frac{1-F(Q(t-\tau_B))}{1-Q(t-\tau_B)})$$
$$-Q(t)^2 \frac{\beta_A(t)}{d_A{}^6}(\frac{F(Q(t))}{Q(t)} - \frac{F(Q(t-\tau_A))}{Q(t-\tau_A)})] \tag{2.4.16}$$

with threshold conditions (2.4.10).

In Part 2.2, it is shown that one state dependent variable and two delays are need

to describe the two node system, and Eq.(2.4.16) satisfies this requirement.

● The three node network

From the Part 2.1, it is known that either node 1 or node 2 can be a diverging

node (see Figure 2.3), but due to their topological symmetry, we can assume one of

them is a diverging node and establish the governing PDE's and DDE's. After the

governing equations are obtained, symmetrical physical parameters can be switched

and another set of governing equations are available readily, which are

corresponding to the other assumption.

25

Assume node 1 is diverging, and from Eq.(2.4.5) $\Rightarrow$

$$\frac{d\bar{H}_A}{dt} = \frac{4Q_1 Q(t)}{\pi d_A^2 l_A}[H_A(0,t) - H_A(0,t-\tau_A)]$$

$$\frac{d\bar{H}_B}{dt} = \frac{4Q_1(1-Q(t)+y_q)}{\pi d_B^2 l_B}[H_B(0,t) - H_B(0,t-\tau_B)]$$

$$\frac{d\bar{H}_C}{dt} = \frac{4Q_1(1-Q(t))}{\pi d_C^2 l_C}[H_C(0,t) - H_C(0,t-\tau_C)],\qquad(2.4.17)$$

where τ_A, τ_B, τ_C are defined by threshold conditions,

$$l_A = \int_{t-\tau_A(t)}^{t} v_A(s)ds = \frac{4Q_1}{\pi d_A^2}\int_{t-\tau_A(t)}^{t} Q(s)ds$$

$$l_B = \int_{t-\tau_B(t)}^{t} v_B(s)ds = \frac{4Q_1}{\pi d_B^2}\int_{t-\tau_B(t)}^{t} (1-Q(s)+y_q)ds$$

$$l_C = \int_{t-\tau_C(t)}^{t} v_C(s)ds = \frac{4Q_1}{\pi d_C^2}\int_{t-\tau_C(t)}^{t} (1-Q(s))ds,\qquad(2.4.18)$$

where $Q = Q_A/Q_1$, $y_q = Q_2/Q_1$, Q_1 and Q_2 are the flow rates in Inlet 1 and Inlet 2 respectively.

From mass and momentum balances, we can find an expression in the form of Eq.(2.4.7), but the process is a little lengthy, so only results are given here.

$$Q(t) = \frac{(1+y_q)R_B(t) + R_C(t)}{R_A(t) + R_B(t) + R_C(t)}\qquad(2.4.19)$$

Since node 1 is assumed to be a diverging node, from plasma skimming and mass balance,

$$H_A(0,t) = H_1\frac{F(Q(t))}{Q(t)}$$

$$H_C(0,t) = H_1\frac{1-F(Q(t))}{1-Q(t)},$$

26

$$H_B(0,t) = \frac{H_C(l_C,t)Q_1(1-Q(t)) + H_2 Q_2}{Q_1(1-Q(t)) + Q_2}$$

(2.4.20)

Combine   Eq.(1.2.4),   (2.4.19),   (2.4.20),   (2.4.17),   and $y_h = \dfrac{H_2 Q_2}{H_1 Q_1}$,

$$y_{com}(t) = (1+y_q)\frac{l_B d_C^4}{l_C d_B^4}\frac{\mu_B(t)}{\mu_C(t)} \quad \Rightarrow$$

$$\frac{dQ(t)}{dt} = \frac{d_C^4}{l_C \mu_C(t)} \frac{4Q_1 H_1}{\pi(1+y_{com}(t))} Q(t) \Big\{ -Q^2(t)\frac{\beta_A(t)}{d_A^6}\Big[\frac{F(Q(t))}{Q(t)} - \frac{F(Q(t-\tau_A(t)))}{Q(t-\tau_A(t))}\Big]$$

$$+(1+y_q - Q(t))^2 \frac{\beta_B(t)}{d_B^6}\Big[\frac{y_h + (1-Q(t))\dfrac{1-F(Q(t-\tau_C(t)))}{1-Q(t-\tau_C(t))}}{1+y_q - Q(t)}$$

(2.4.21)

$$-\frac{y_h + (1-Q(t-\tau_B(t)))\dfrac{1-F(Q(t-\tau_B(t)-\tau_C(t)))}{1-Q(t-\tau_B(t)-\tau_C(t))}}{1+y_q - Q(t-\tau_B(t))}\Big]$$

$$+(1-Q(t))^2 \frac{\beta_C(t)}{d_C^6}\Big[\frac{1-F(Q(t))}{1-Q(t)} - \frac{1-F(Q(t-\tau_C(t)))}{1-Q(t-\tau_C(t))}\Big]\Big\}$$

with threshold conditions Eq.(2.4.18).

It is pointed out in Part 2.2 that one state dependent variable and four delays are needed to describe the three node system. Since $\tau_B + \tau_C$ can be regarded as a combined delay, the Eq.(2.4.21) combined with Eq.(2.4.18) suffices to describe the three node system.

27

2.5 Steady-state Solutions

Since it is known that when a system is at equilibrium, all state-dependent variables are unchanged with time, the hematocrit in a branch is uniform. Thus Eq.(2.4.7) can be rewritten as

$$\tilde{Q}_i(t) = Q_i(R_1(\tilde{H}_1), \ldots, R_m(\tilde{H}_m), par),$$ (2.5.1)

where $\tilde{H}_i$ denotes the hematocrit in branch i at steady states.

Suppose the values of Q_i at a steady state are guessed, the flow rate and the average hematocrit in each branch can be calculated according to the mass balance and the plasma skimming model. Then the hydraulic resistance of each branch can be computed. By conducting momentum balance, the flow rate in each branch is calculated again, which renews the value of Q. The guessed Q must be equal to the calculated Q at steady states. To conclude, to find out equilibrium solutions in a certain network, roots of

$$\mathbf{Q} = G(\mathbf{Q})$$ (2.5.2)

need to be found, where $\mathbf{Q}$ is a k-dimensional vector consisting of Q_i, G is a continuous function on $\mathbf{R}^k$.

Because $G(\mathbf{Q})$ integrates information of viscosity models and plasma skimming models, it is a group of coupled nonlinear expressions of $\mathbf{Q}$. Due to the nonlinear properties of Eq.(2.5.2), it is difficult to solve analytically and numerical approaches need to be applied to seek solutions.

Illustrations of determining steady states in the two node network and the three node network are shown as follows. Since only one state dependent variable is

28

required for these two simple networks, Eq.(2.5.2) is written as

$$Q = g(Q), \qquad\qquad (2.5.3)$$

where Q is a scalar and g is a continuous function on $\mathbf{R}^1$.

A straightforward approach is a graphing method. In the graphing method, $g(Q)$ is plotted versus Q which ranges from 0 to 1, the curves ought be continuous. If the curves intersect with an identical line, the crossing points correspond to the equilibrium solutions, which satisfy Eq.(2.5.3).

An advantage of the graphing method is that all existing roots can be caught with enough small searching steps, but its shortcoming is also obvious – low efficiency. When the graphing method is used to find equilibrium solutions in many sets of parameters, the algorithm is too sluggish to be acceptable. Therefore, in this paper the practical algorithm is to combine the graphing method with a bisection method. The former is used to find small regions of Q where the steady states exist, and then the latter is applied in these regions to find the roots readily. A good balance between efficiency and accuracy is of importance – if the searching steps of graphing method are too large, some roots may be missed; if the searching steps are too small, there is no improvement of efficiency. Examples about finding steady states are given as follows.

29

- The two node network

At steady states, Eq.(2.4.12) is rewritten as

$$\tilde{Q} = \frac{R_B(\tilde{Q})}{R_A(\tilde{Q}) + R_B(\tilde{Q})}$$
(2.5.4)

and the right hand side of Eq.(2.5.4) is the form of $f(Q)$ in Eq.(2.5.3). $R_A(\tilde{Q})$ and

$R_B(\tilde{Q})$ can be computed by

$$R_A(\tilde{Q}) = \frac{128 l_A \mu_A (H_A(\tilde{Q}))}{\pi d_A^4}$$

$$R_B(\tilde{Q}) = \frac{128 l_B \mu_B (H_B(\tilde{Q}))}{\pi d_B^4}.$$
(2.5.5)

Since Node 1 is a diverging node,

$$H_A(\tilde{Q}) = H_1 \frac{F(\tilde{Q})}{\tilde{Q}}$$

$$H_B(\tilde{Q}) = H_1 \frac{1 - F(\tilde{Q})}{1 - \tilde{Q}}.$$
(2.5.6)

According to the definition $Q = Q_A / Q_1$, the value of Q is always between 0 and

1, and the values of the RHS of Eq.(2.5.4) are always between 0 and 1 because of the

positive signs of resistance. It can be concluded that at least one steady state exist

because of the RHS continuity of Eq.(2.5.4). Figure 2.4 and Figure 2.5 present a one

steady state situation and a three steady states situation respectively.

30
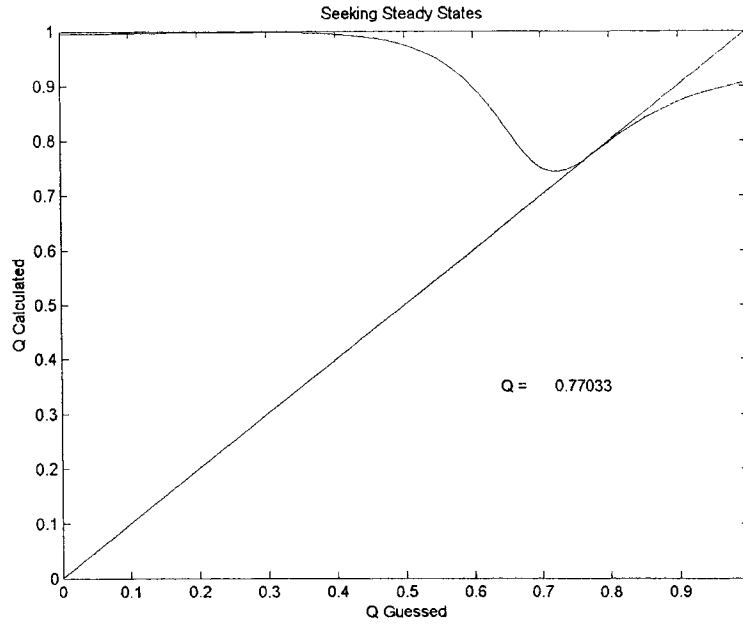
Figure 2.4   An Equilibrium Solutions $Q \approx$ 0.77 Obtained.

The parameter values are logit plasma skimming parameter p = 2.0, Pries's in vitro viscosity model, H_1 = 0.80, d_A = 35μm, d_B = 20μm, l_A = 500μm, l_B = 2500μm.
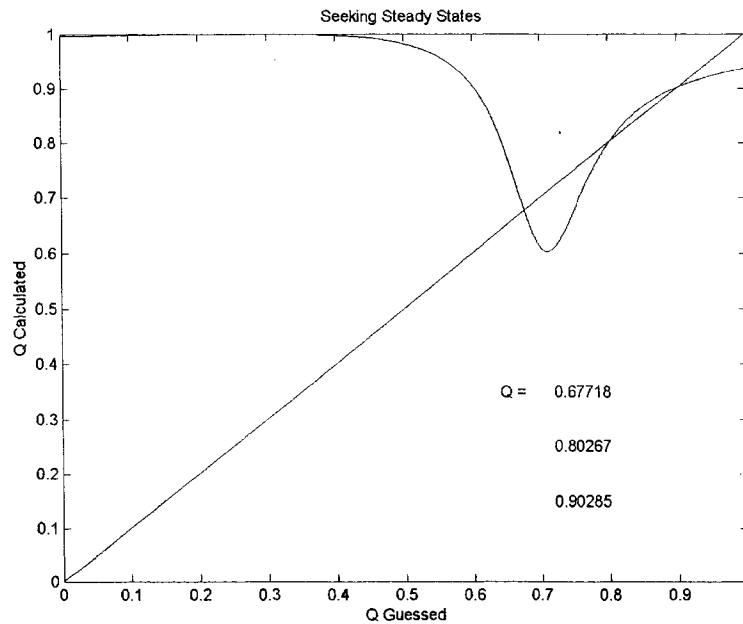
Figure 2.5   Three Equilibrium Solutions $Q \approx$ 0.68, 0.80, 0.90 Obtained.

The parameter values are logit plasma skimming parameter p = 2.0, Pries's *in vitro* viscosity model, H_1 = 0.82, d_A = 32μm, d_B = 14μm, l_A = 900μm, l_B = 2500μm.

31

- The three node network

At steady states, Eq.(2.4.19) can be rewritten as

$$\tilde{Q} = \frac{(1+y_q)R_B(\tilde{Q}) + R_C(\tilde{Q})}{R_A(\tilde{Q}) + R_B(\tilde{Q}) + R_C(\tilde{Q})} \qquad (2.5.7)$$

and the right hand side of Eq.(2.5.4) is the form of $f(Q)$ in Eq.(2.5.3). $R_i(\tilde{Q})$

$(i=A,B,C)$ can be computed by

$$R_i(\tilde{Q}) = \frac{128 l_i \mu_i (H_i(\tilde{Q}))}{\pi d_i^4} \qquad (2.5.8)$$

Since either node 1 or node 2 can be a diverging node, assume divergence occurs at

Node 1,

$$H_A(\tilde{Q}) = H_1 \frac{F(\tilde{Q})}{\tilde{Q}}$$

$$H_C(\tilde{Q}) = H_1 \frac{1 - F(\tilde{Q})}{1 - \tilde{Q}},$$

$$H_B(\tilde{Q}) = \frac{H_C(\tilde{Q})Q_1(1-\tilde{Q}) + H_2 Q_2}{Q_1(1-\tilde{Q}) + Q_2} \qquad (2.5.9)$$

According to the definition $Q = Q_A / Q_1$, this time the value of Q is not always

between 0 and 1, so a modified Q is defined as $Q^* = Q_A /(Q_1 + Q_2)$ whose values are

always between 0 and 1. When $Q^* < Q_1 /(Q_1 + Q_2)$, Node 1 is a diverging node, and

the Eq.(2.5.8,9) can be used to calculate the RHS of Eq.(2.5.7); when

$Q^* = Q_1 /(Q_1 + Q_2)$, no blood flows through the branch C; when $Q^* > Q_1 /(Q_1 + Q_2)$,

Node 2 is a diverging node, so in Eq.(2.5.8, 9) accordingly the physical parameters

of branch A and branch B need to be switched, and those properties of Inlet 1 and

Inlet 2 are also exchanged. Figure 2.6 and Figure 2.7 present an asymmetric system

case and a symmetric system case respectively.

32
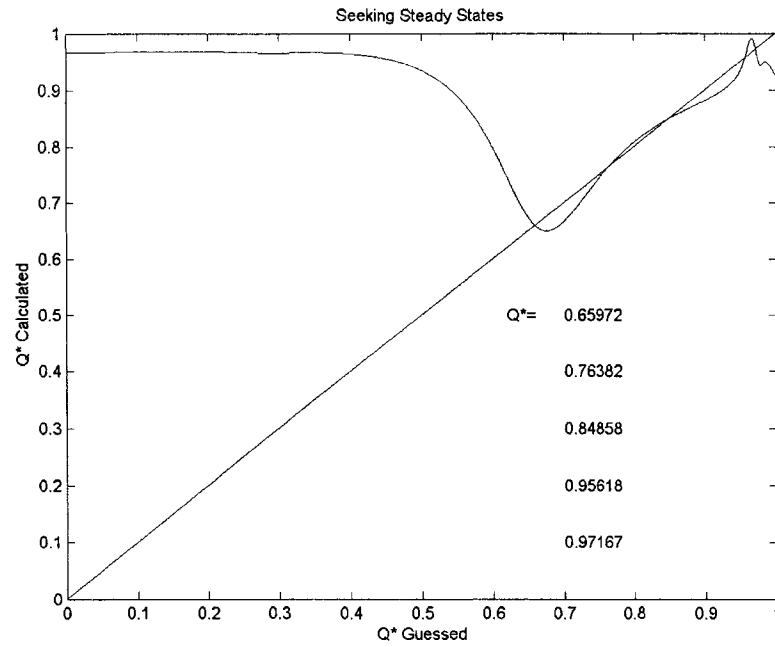
Figure 2.6   Five Equilibrium Solutions Obtained for an Asymmetric Three Node Network. Logit plasma skimming, parameter p = 2.1 at both node 1 and 2, Pries's *in vitro* viscosity model, H_1 = 0.80, H_2 = 0.80, Q_1 = 10nl/min, Q_2 = 0.05nl/min, d_A = 35μm, d_B = 20μm, d_C = 20μm, l_A = 500μm, l_B = 1000μm, l_C = 1500μm.
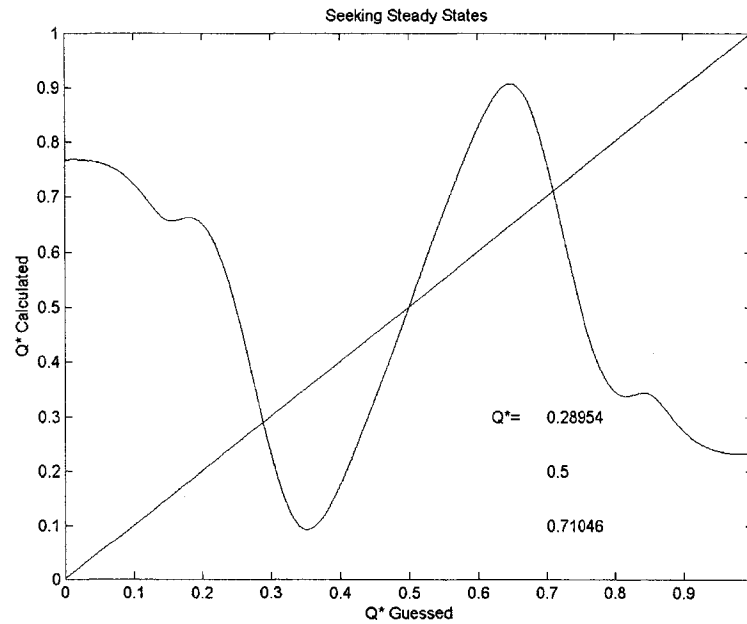
Figure 2.7   Three Equilibrium Solutions Obtained for a Symmetric Three Node Network. Q_1 = 10nl/min, Q_2 = 10nl/min. Other parameters are kept constant as those in Figure 2.6.

33

2.6 Characteristic Equations

Consider the delay differential equations with constant delays,

$$\frac{dx}{dt} = f(x(t), x(t-\tau_1), ..., x(t-\tau_m)),\qquad (2.6.1)$$

where $\tau_1, ..., \tau_m$ are time delays.

To reduce the parameters of DDEs, the Eq.(2.6.1) is normalized by substituting $s = t / \tilde{\tau}_m$, $\theta_i = \tau_i / \tilde{\tau}_m$ ($i = 0,1,...,m$) into it, where $\tilde{\tau}_m$ is the mth time delay at the steady state, yielding

$$\frac{dx}{ds} = f(x(s), x(s-\theta_1), ..., x(s-\theta_m)).\qquad (2.6.2)$$

Expand the equation (2.6.2) to Taylor series around a steady state x^* and neglect second derivatives or higher order items (Kreyszig, 1993)[54] $\Rightarrow$

$$\frac{dx}{ds} = f(x^*, ..., x^*) + \frac{\partial f}{\partial x}\bigg|_{(x^*,...,x^*)}(x-x^*) + \sum_{i=1}^{m} \frac{\partial f}{\partial x(s-\theta_i)}\bigg|_{(x^*,...,x^*)}(x(s-\theta_i)-x^*). \quad (2.6.3)$$

Let $A_i = \dfrac{\partial f}{\partial x(s-\theta_i)}\bigg|_{(x^*,...,x^*)}$ and let $y(s-\theta_i) = x(s-\theta_i) - x^*$ ($i=1,...,m$) $\Rightarrow$

$$\frac{dy}{ds} = A_0 y(s) + \sum_{i=1}^{m} A_i y(s-\theta_i),\qquad (2.6.4)$$

which is called varational equation (Hale, 1977)[55].

To obtain the characteristic equation, substitute the form $y(s) = Ce^{\lambda s}$ into the equation (2.6.4), where C is constant. The equation (2.6.4) has a nontrivial solution $Ce^{\lambda s}$ if and only if

$$\lambda = A_0 + \sum_{i=0}^{m} A_i e^{-\lambda \theta_i}.\qquad (2.6.5)$$

Eq. (2.6.5) is called the characteristic equation of the system. Illustrations of derivation of the characteristic equations for the networks are shown as follows.

34

- The two node network

Substitute $s = t / \tilde{\tau}_B$ into the equation (2.4.16) $\Rightarrow$

$$\frac{dQ(t)}{ds} = \frac{H_1}{\mu_B(s)} \frac{Q(s)}{1-Q(s)} [(1-Q(s))^2 \beta_B(s)(\frac{1-F(Q(s))}{1-Q(s)} - \frac{1-F(Q(s-\theta_B))}{1-Q(s-\theta_B)})$$
$$- Q(s)^2 \frac{\beta_A(s)}{d_A^6} (\frac{F(Q(s))}{Q(s)} - \frac{F(Q(s-\theta_A))}{Q(s-\theta_A)})] \tag{2.6.6}$$

Linearize the equation (2.6.6) around a steady state $\tilde{Q}$, and let $y(s) = Q(s) - \tilde{Q}$ and

$$b = \frac{H_1}{\mu_B(\tilde{Q})} \frac{\tilde{Q}^2}{1-\tilde{Q}} \beta_A(\tilde{Q})(\frac{d_B}{d_A})^6 (\frac{dF(Q)}{dQ}\Big|_{\tilde{Q}} - \frac{F(Q)}{Q}\Big|_{\tilde{Q}}) \tag{2.6.7}$$

$$c = \frac{H_1}{\tilde{\mu}_B(\tilde{Q})} \tilde{Q} \beta_B(\tilde{Q})(\frac{dF(Q)}{dQ}\Big|_{\tilde{Q}} - \frac{1-F(Q)}{1-Q}\Big|_{\tilde{Q}}) \tag{2.6.8}$$

$$\Rightarrow \frac{dy}{ds} = -(b+c)y(s) + by(s-\gamma) + cy(s-1), \tag{2.6.9}$$

where $\gamma = \tilde{\tau}_A / \tilde{\tau}_B = d_A^2 l_A (1-\tilde{Q}) / (d_B^2 l_B \tilde{Q})$.

Substitute $ce^{\lambda t}$ into the equation (2.6.9) $\Rightarrow$

$$\lambda = -(b+c) + be^{-\gamma\lambda} + ce^{-\lambda}, \tag{2.6.10}$$

which is the characteristic equation of the two node network.

- The three node network

Substitute $s = t / \tilde{\tau}_C$ into the equation (2.4.21) $\Rightarrow$

$$\frac{dQ(s)}{ds} = \frac{d_C^6 H_1}{\mu_C(s)(1+y_{com})} \frac{Q(s)}{1-\tilde{Q}} \{-Q^2(s) \frac{\beta_A(s)}{d_A^6} [\frac{F(Q(s))}{Q(s)} - \frac{F(Q(s-\theta_A))}{Q(s-\theta_A)}]$$
$$+ (1+y_q - Q(s))^2 \frac{\beta_B(s)}{d_B^6} [\frac{y_h + (1-Q(s))\frac{1-F(Q(s-\theta_C))}{1-Q(s-\theta_C)}}{1+y_q - Q(s)}$$
$$- \frac{y_h + (1-Q(s-\theta_B(s)))\frac{1-F(Q(s-\theta_B-\theta_C))}{1-Q(s-\theta_B-\theta_C)}}{1+y_q - Q(s-\theta_B)}]$$
$$+ (1-Q(s))^2 \frac{\beta_C(s)}{d_C^6} [\frac{1-F(Q(s))}{1-Q(s)} - \frac{1-F(Q(s-\theta_C))}{1-Q(s-\theta_C)}]\} \tag{2.6.11}$$

35

Linearize the equation (2.6.11) around the steady state $\tilde{Q}$, and let $y(s) = Q(s) - \tilde{Q}$

and

$$a = \frac{H_1}{\mu_C(\tilde{Q})(1 + y_{com}(\tilde{Q}))} \frac{\tilde{Q}}{1 - \tilde{Q}} \beta_B(\tilde{Q})(\frac{d_C}{d_B})^6(1 + y_q - \tilde{Q})(\frac{dF}{dQ}\Big|_{\tilde{Q}} - \frac{1 - F}{1 - Q}\Big|_{\tilde{Q}}) \quad (2.6.12)$$

$$b = \frac{H_1}{\mu_C(\tilde{Q})(1 + y_{com}(\tilde{Q}))} \frac{\tilde{Q}^2}{1 - \tilde{Q}} \beta_A(\tilde{Q})(\frac{d_C}{d_A})^6(\frac{dF}{dQ}\Big|_{\tilde{Q}} - \frac{F}{Q}\Big|_{\tilde{Q}}) \quad (2.6.13)$$

$$c = \frac{H_1}{\mu_C(\tilde{Q})(1 + y_{com}(\tilde{Q}))} \tilde{Q}\beta_C(\tilde{Q})(\frac{dF}{dQ}\Big|_{\tilde{Q}} - \frac{1 - F}{1 - Q}\Big|_{\tilde{Q}}) \quad (2.6.14)$$

$$d = \frac{H_1}{\mu_C(\tilde{Q})(1 + y_{com}(\tilde{Q}))} \frac{\tilde{Q}}{1 - \tilde{Q}} \beta_B(\tilde{Q})(\frac{d_C}{d_B})^6 y_q(\frac{dF}{dQ}\Big|_{\tilde{Q}} - \frac{H_2}{H_1}) \quad (2.6.15)$$

$\Rightarrow$

$$\frac{dy}{ds} = -(b + c + d)y(s) + by(s - \gamma) + dy(s - \delta) + ay(s - \delta - 1) + (c - a)y(s - 1), \quad (2.6.17)$$

where $\quad \gamma = \tilde{\tau}_A / \tilde{\tau}_C = \frac{d_A^2 l_A}{d_C^2 l_C} \frac{1 - \tilde{Q}}{\tilde{Q}} \quad , \quad \delta = \tilde{\tau}_B / \tilde{\tau}_C = \frac{d_B^2 l_B}{d_C^2 l_C} \frac{1 - \tilde{Q}}{1 - \tilde{Q} + y_q} \quad , \quad y_h = \frac{H_2 Q_2}{H_1 Q_1} \quad ,$

$$y_{com}(t) = (1 + y_q)\frac{l_B d_C^4}{l_C d_B^4} \frac{\mu_B(t)}{\mu_C(t)}$$

Substitute $C_l e^{\lambda s}$ into the equation (2.6.17), C_l is a constant $\Rightarrow$

$$\lambda = -(b + c + d) + be^{-\gamma\lambda} + de^{-\delta\lambda} + (c - a)e^{-\lambda} + ae^{-(\delta+1)\lambda}, \quad (2.6.18)$$

which is the characteristic equation of the three node network with two inlets and

one outlet.

36

2.7 "DDE-BIFTOOL" and Eigenvalues

"DDE-BIFTOOL" package consists of a set of MatLAB® routines and provides a tool for numerical stability and bifurcation analysis of steady state solutions and other aims (Engelborghs et al., 2001)[56]. All analyses are based on the computation of characteristic roots of systems of DDEs by using linear multi-step (LMS) methods. Instead of solving the nonlinear characteristic equation directly, LMS methods turn to estimate the characteristic roots by solving a large but standard eigenvalue problem, then a Newton-Raphson iteration is used to improve the accuracy of the roots (Engelborghs et al., 2002)[57]. The package also includes other bifurcation analysis functions, but in this paper, we mainly use DDE-BIFTOOL to calculate the characteristic roots of the DDEs derived from the mathematical models describing the simple networks.

DDE-BIFTOOL can deal with both DDEs with constant delays and DDEs with state-dependent delays (sd-DDEs). Obviously, the DDEs (2.6.10) and (2.6.18) describing the simple networks are both sd-DDEs. However, it is found that treating the delays as constant does not effect the results at all (Luzyanina et al., 2001)[53], which is illustrated in the two node network case (see Appendix C).

Inside a user manual of the DDE-BIFTOOL, it is required to define systems using MatLAB® functions. Details of the specification are available from the user manual – Report TW 330 (Engelborghs et al., 2001)[56]. The required RHS functions and the first order derivatives of RHS functions with respect to state variables in the simple networks are presented in Appendix A.

37

We should notice that in DDE-BIFTOOL, the eigenvalues are found for the characteristic equations in form of Eq.(2.6.5) instead of normalized ones like Eq.(2.6.10) or Eq.(2.6.18). But these two kinds of characteristic equations are equivalent in nature, and their eigenvalues are equal after being multipled by a scaling factor (see Appendix C). An example of finding the rightmost eigenvalues of a given system is presented below. Here, "rightmost" means at the most right part of a profile of characteristic roots.

A two node network is investigated. The Pries's *in vitro* viscosity model and the logit plasma skimming model are used here. The physical parameters are: $p = 2.0$, H_1 = 0.80, $Q_1 = 10nl/min$, $d_A = 35\mu m$, $d_B = 20\mu m$, $l_A = 500\mu m$, $l_B = 2500\mu m$. It is found at equilibrium, $\tilde{Q} = 0.77033$, $\tilde{\tau}_A = 3.746\sec$, $\tilde{\tau}_B = 20.51\sec$. For the characteristic equation

$$\lambda = A_0 + A_1 e^{-\lambda \tau_1} + A_2 e^{-\lambda \tau_2} \qquad (2.7.1)$$

where $A_0 = 0.3070$, $A_1 = -0.3232$, $A_2 = 0.01614$.

The profile of eigenvalues generated by DDE-BIFTOOL are presented in Figure 2.7, and the rightmost roots are $\lambda = 0.012103 \pm 0.089663i$. Symbol (x) denotes approximated roots computed from LMS methods and symbol (*) denotes corrected roots via the Newton-Raphson approach.

In fact, Eq.(2.6.10) and Eq.(2.6.18) can be arranged and written as iteration forms

$$\text{Re}(\lambda) = \mathbf{F}(\text{Re}(\lambda), \text{Im}(\lambda))$$

$$\text{Im}(\lambda) = \mathbf{G}(\text{Re}(\lambda), \text{Im}(\lambda)) \qquad (2.7.2)$$

38

and successive substitution methods (Rice and Do, 1994)[58] can be applied to Eq.(2.7.2) to produce the characteristic roots. Since DDE-BIFTOOL provides a general way to produce the characteristic roots and it is also convenient to generate graphical results as well, the numerical results discussed in the following section are mostly generated from this MatLAB® package. The application of successive substitution method in solving Eq.(2.6.10) and Eq.(2.6.18) are included in Appendix C and the comparisons between results from two methods are also included there.
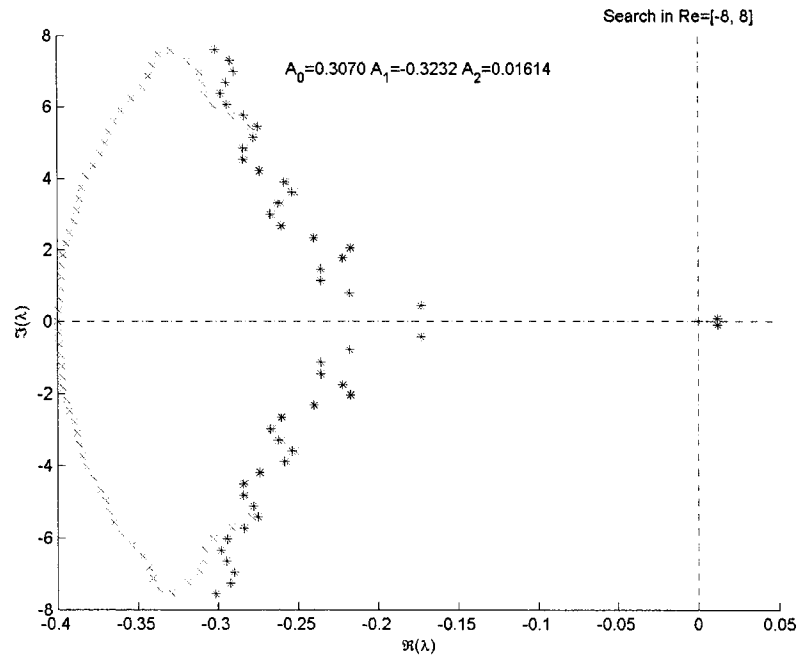
Figure 2.8   A Graphical Illustration of Eigenvalues Profiles Generated by DDE-BIFTOOL. These eigenvalues correspond to a two node network with $p=2.0$, $H_1 = 0.80$, $Q_1 = 10\text{nl/min}$, $d_A = 35\mu\text{m}$, $d_B = 20\mu\text{m}$, $l_A = 500\mu\text{m}$, $l_B = 2500\mu\text{m}$ with the *in vitro* viscosity model and the logit plasma skimming model.

39

CHAPTER III

NUMERICAL RESULTS ABOUT TWO NODE MICROVASCULAR NETWORKS

The two node topology shown in the Figure 2.2 is investigated numerically using DDE-BIFTOOL. By varying physical parameters or blood rheology models, flow in different networks is studied. Characteristic roots of systems are calculated via the MatLAB® subroutines (included in Appendix B). The predicted stability of the system around steady states is examined by a simulation program (Carr and LeCoin, 2000)[2] written in FORTRAN.

3.1 Effects of Viscosity Models

Pries and his colleagues have published empirical correlations of both the *in vitro* viscosity model (Pries *et al.*, 1992)[13] and the *in vivo* viscosity model (Pries *et al.*, 1994)[14]. Effects of both viscosity models on the instability of the system are checked here. Characteristic roots of the system are computed based on the two different viscosity models. The physical parameters are given as following: the logit plasma skimming parameter $p = 2.0$, $H_I = 0.8$, $Q_I = 10$nl/min, $d_A = 35\mu$m, $d_B = 20\mu$m, $l_A = 500\mu$m, $l_B = 2500\mu$m.

When the *in vitro* viscosity model is applied, one steady state exists and $\tilde{Q}=0.77033$; when the *in vivo* viscosity model is applied, one steady state exists and $\tilde{Q}=0.80826$. Accordingly, the coefficients in Eq.(2.6.10) are different.

40

The characteristic roots are computed by DDE-BIFTOOL and presented in Figure 3.1 and Figure 3.2 respectively.
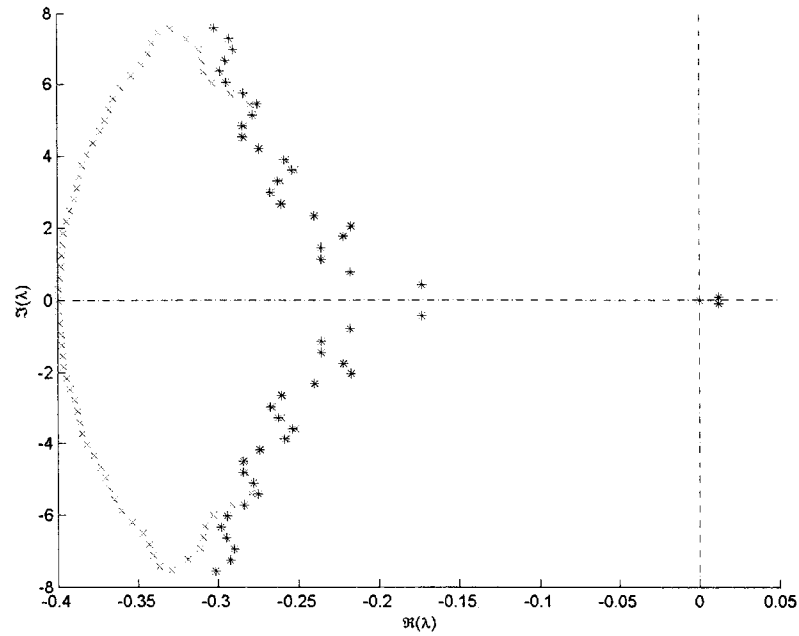
Figure 3.1 Characteristic Roots Generated with the *In Vitro* Viscosity Model.
Other parameters are: the logit plasma skimming parameter $p = 2.0$, $H_I = 0.8$, $Q_I = 10\text{nl/min}$, $d_A = 35\mu\text{m}$, $d_B = 20\mu\text{m}$, $l_A = 500\mu\text{m}$, $l_B = 2500\mu\text{m}$.
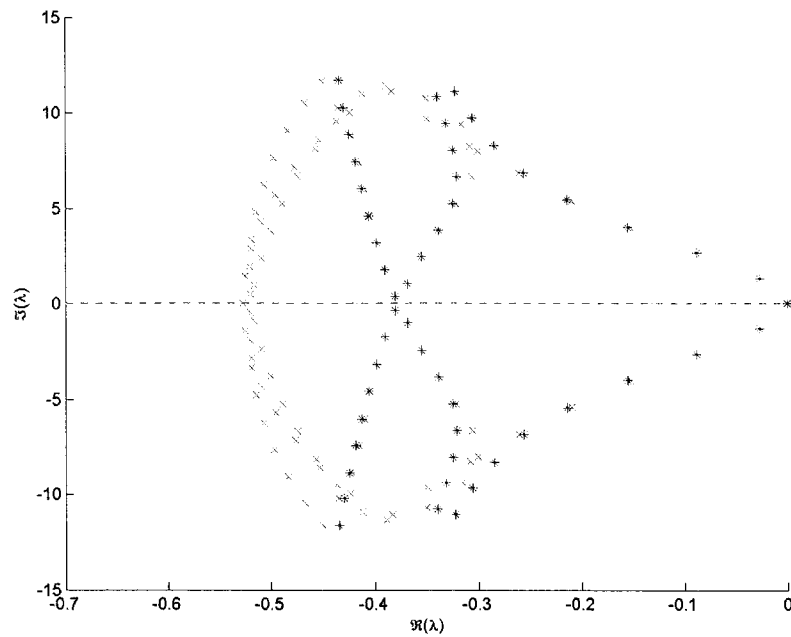
Figure 3.2 Characteristic Roots Generated with the *In Vivo* Viscosity Model.
Other parameters are the same as those in Figure 3.1.

41

The graphs show that the two viscosity models lead to different profiles of characteristic roots, i.e. eigenvalues. We need to note zero roots are always trivial ones (Carr et al., 2005)[48], so the rightmost eigenvalues are also different. Therefore, different viscosity models impact the stability of microvascular networks. Since the theoretical work done in this paper is expected to be verified by future experiments in in vitro replicas of microvascular networks, the in vitro viscosity model is applied in following parts of this paper.

3.2 Effects of Plasma Skimming Parameters

Two plasma skimming models are used in this paper – one is the linear model (Fenton et al., 1985)[20], and the other is the logit model (Dellimore et al., 1983)[21]. From Figure 1.4, the two models do possess different functional characteristics, especially at two ends of the range of volumetric flow ratios. This section identifies the effects of the two plasma skimming models on the systems' stability, and plasma skimming parameters are also varied for both plasma skimming models.

The in vitro viscosity model is used during an investigation process. Other physical parameters are H_I = 0.8, Q_I = 10nl/min, d_A = 35μm, d_B = 20μm, l_A = 500μm, l_B = 2500μm. The steady states $\tilde{Q}$ are plotted with varying plasma skimming parameter p. It is noticed from Figure 3.3 and Figure 3.4 that single steady states exist with given physical parameters.

42

Figure 3.3   Steady States Q versus Linear Plasma Skimming Parameter.
Other physical parameters are $H_I = 0.8$, $Q_I = 10\text{nl/min}$, $d_A = 35\mu\text{m}$, $d_B = 20\mu\text{m}$, $l_A = 500\mu\text{m}$, $l_B = 2500\mu\text{m}$.


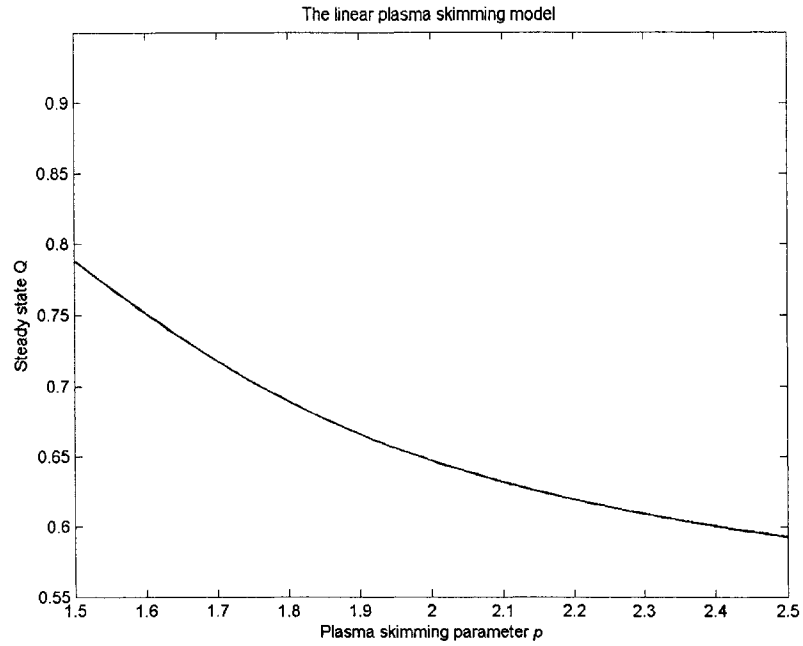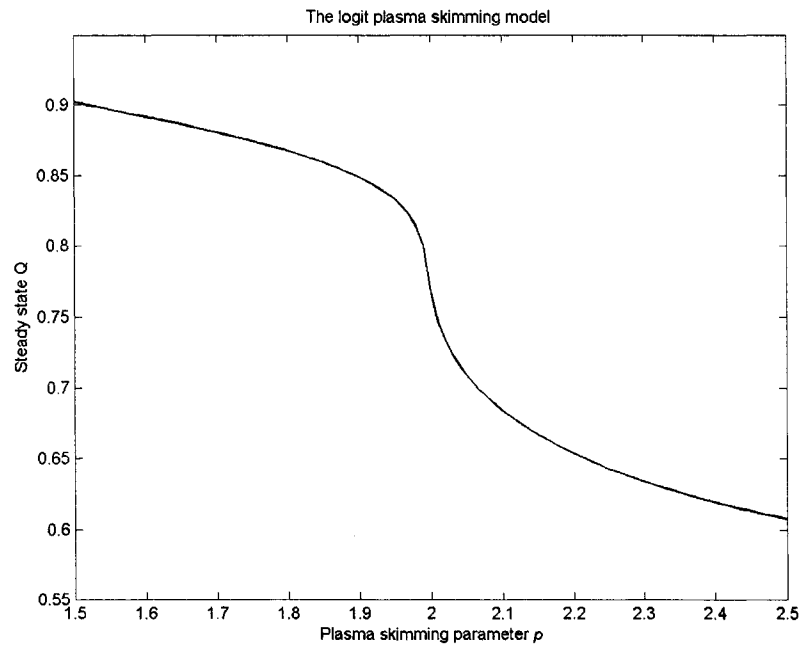**Figure 3.4   Steady States Q versus Logit Plasma Skimming Parameter.**
Other physical parameters are the same as those in Figure 3.3.

43

At the computed steady states, the real parts of the rightmost eigenvalues are computed from DDE-BIFTOOL and are plotted against varying plasma skimming parameter p. (See Figure 3.5 and Figure 3.6)

From Figure 3.5, it seems that the real parts of rightmost eigenvalues are negative where plasma skimming parameter p ranges from 1.5 to 2.5. However, Figure 3.6 shows that the real parts of rightmost eigenvalues are positive in a small range where $p \approx 2.0$. The curves in the two graphs also show quite different shapes. A potential explanation is that the two plasma skimming models have distinct definitions where the volumetric flow ratio Q is close to 0 or 1. We can notice in Figure 3.3 and Figure 3.4 that when $p < 2.1$ the values of computed Q at equilibrium are quite different from each other and are close to 1 as well. Since coefficients in characteristic equations are all computed based on plasma skimming correlations and corresponding derivatives at steady states, the above differences will result in the various characteristic roots. It is hard to say which one of the two models is more accurate because they are both empirical correlations. The logit plasma skimming correlation is mainly used in the following due to its smooth shape and continuous first derivatives with respect to Q, which are thought to be more convenient for analytical studies.

44

The linear plasma skimming model
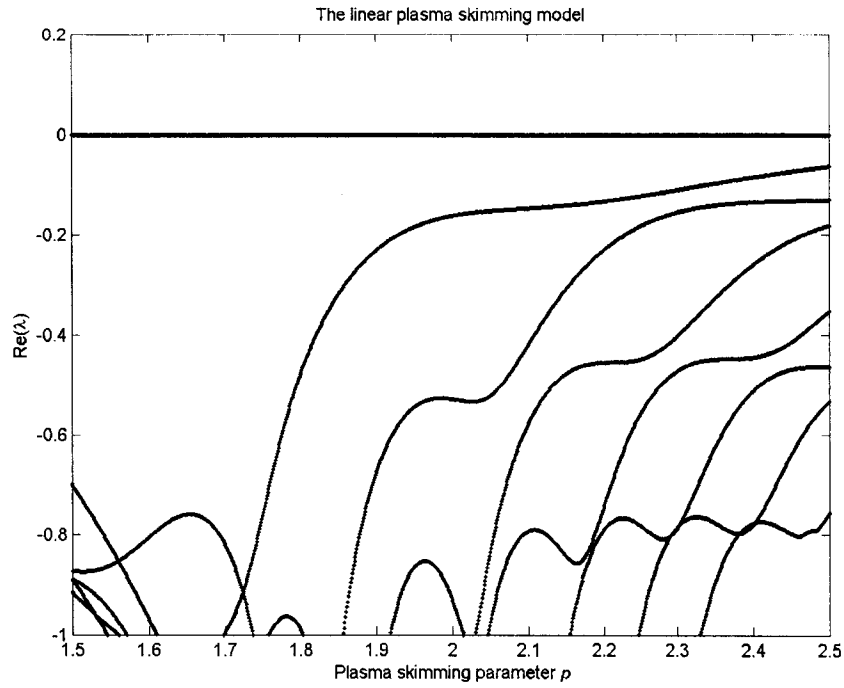

Figure 3.5   Re(λ) versus Linear Plasma Skimming Parameter.
Other physical parameters are $H_l = 0.8$, $Q_l = 10$nl/min, $d_A = 35\mu$m, $d_B = 20\mu$m, $l_A = 500\mu$m, $l_B = 2500\mu$m.

The logit plasma skimming model
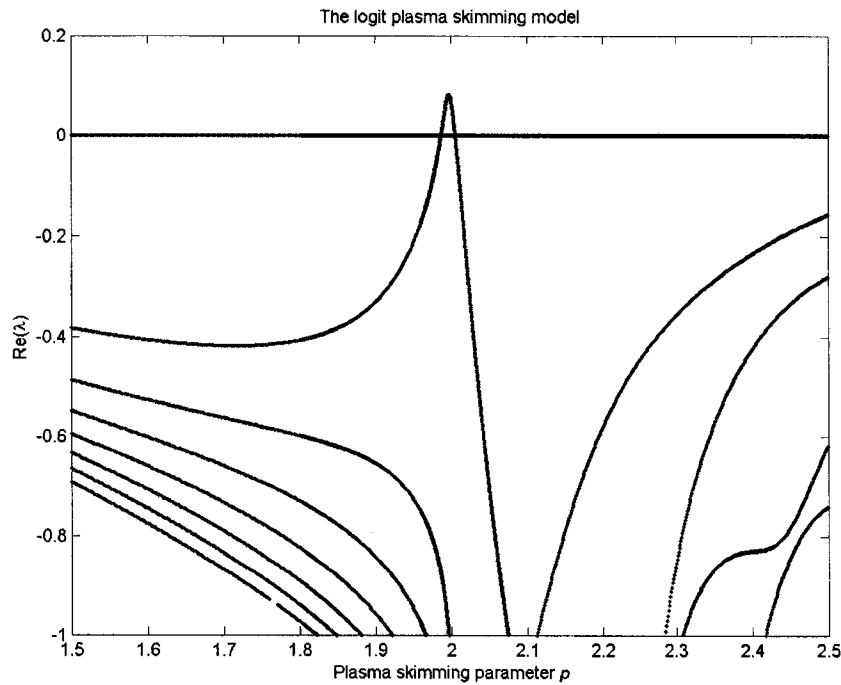
Figure 3.6   Re(λ) versus Logit Plasma Skimming Parameter.
Other physical parameters are the same as those in Figure 3.5.

45

3.3 Effects of Inlet Hematocrit

In a normal human body, the red blood cell concentration, i.e., hematocrit, is about 0.40 ~ 0.45. However, the hematocrit is adjustable for experiments. The procedures in detail are available in Carr's Ph.D. dissertation (Carr, 1984)[18]. Briefly, RBCs in blood are separated from plasma after centrifugation and then washed several times using a buffer solution. According to the hematocrit desired, a certain amount of buffer solutions is added to RBCs to form a suspension after mixing. Finally, the hematocrit in the new "blood" is measured by a capillary method.

Obviously, the inlet hematocrit is an important physical parameter that is adjustable in experiments. The following numerical research focuses on the impact of inlet hematocrits on the system stability at steady states. The *in vitro* viscosity model and the logit plasma skimming model are used here.

The inlet hematocrits are changed during the numerical studies, and other constant parameters are given as follows: Logit plasma skimming parameter $p = 2.0$, $Q_I = 10 \text{nl/min}$, $d_A = 35 \mu\text{m}$, $d_B = 20 \mu\text{m}$, $l_A = 500 \mu\text{m}$, $l_B = 2500 \mu\text{m}$. First, steady states of the system are calculated with various inlet hematocrits (see Figure 3.7). Then the rightmost eigenvalues are computed at the steady states using DDE-BIFTOOL package (see Figure 3.8a and Figure 3.8b).

Figure 3.7 shows that when inlet hematocrits increase to more than 0.70, the flow ratio at equilibrium decreases quickly against increasing inlet hematocrit H_I. Accordingly, the curves of the real parts of rightmost eigenvalues exhibit sharp changes against the inlet hematocrit where H_I is about 0.8. A whole profile is presented in Figure 3.8a and more detail is shown in Figure 3.8b. These abrupt changes can be explained as the very nonlinear inherent properties of the system. From Figure 3.8b, it is noticed that the real parts of rightmost eigenvalues are greater

than zero in a very narrow range of inlet hematocrits H_I (about 0.798 ~ 0.802).

Figure 3.8a and Figure 3.8b convey two pieces of information: the stability analysis around steady states predicts possible oscillations in the two node network; the inlet hematocrits corresponding to oscillations are quite high and the range of hematocrits is very narrow, thus experimental verifications are difficult to perform for these theoretical predictions.
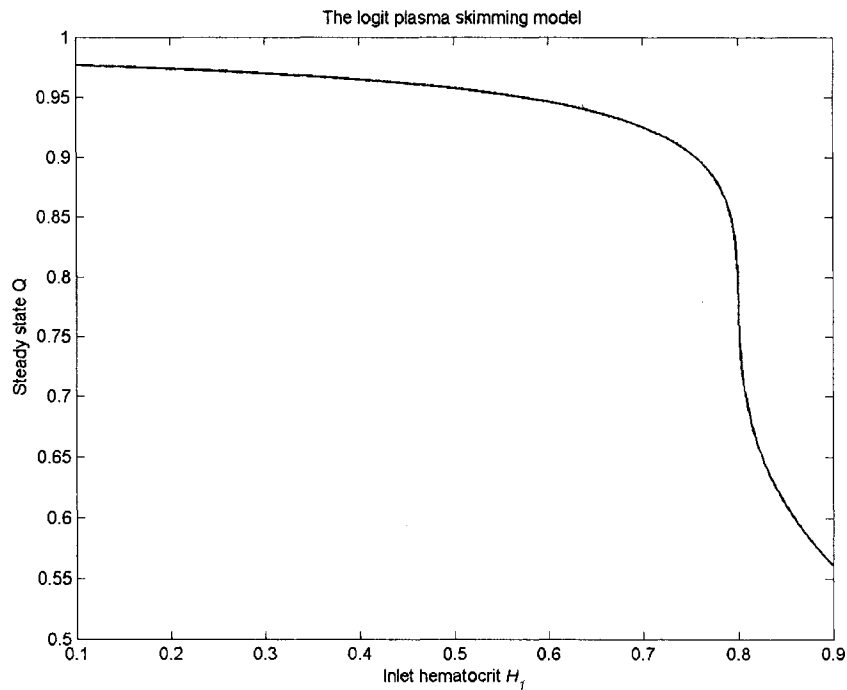
Figure 3.7   Steady State Q versus Inlet Hematocrit.
Other physical parameters are the logit plasma skimming parameter p = 2.0, Q_I = 10nl/min, d_A = 35μm, d_B = 20μm, l_A = 500μm, l_B = 2500μm.

47
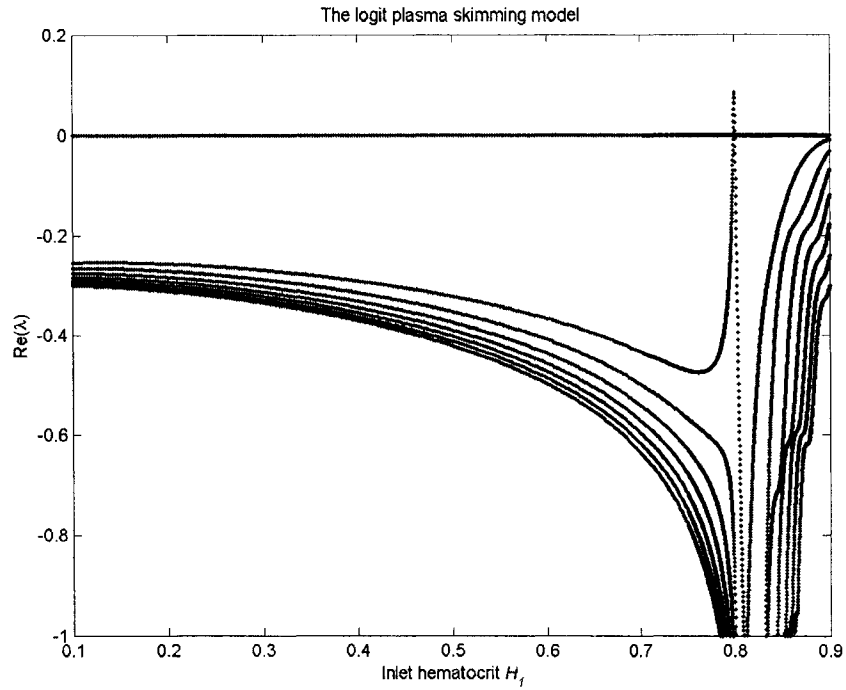
Figure 3.8a Re(λ) versus Inlet Hematocrit with H_I Ranging from 0.1 to 0.9.
Other physical parameters are the logit plasma skimming parameter $p = 2.0$, $Q_I = $
10nl/min, $d_A = 35\mu$m, $d_B = 20\mu$m, $l_A = 500\mu$m, $l_B = 2500\mu$m.
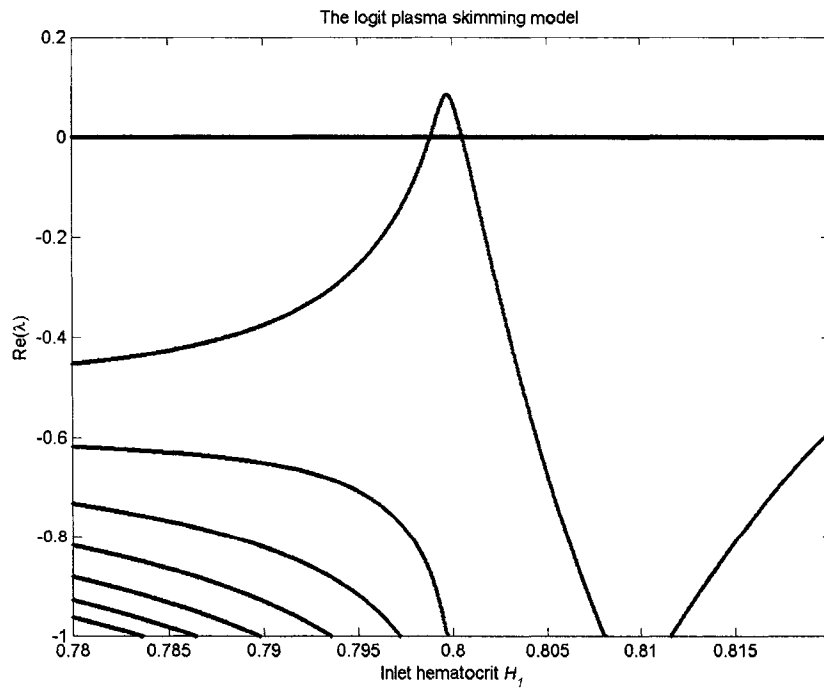
Figure 3.8b Re(λ) versus Inlet Hematocrits with H_I Ranging from 0.78 to 0.82.
Other physical parameters are the same as those in Figure 3.8a.

48

3.4 Effects of Diameters of Branches

To build a practical *in vitro* simple microvascular networks that can exhibit spontaneous oscillations, effects of diameters and lengths of branches ought to be investigated. In this section, the effect of diameters of branches is studied, and the influence of lengths of branches is examined in the next.

During the investigation, the diameter of branch A (see Figure 2.2) is varied, while the diameter of branch B and other physical parameters are fixed. The values of these fixed parameters are listed as following: $p = 2.0$, $H_I = 0.8$, $Q_I = 10$nl/min, $d_B = 20\mu$m, $l_A = 500\mu$m, $l_B = 2500\mu$m. The *in vitro* viscosity model and the logit plasma skimming model are applied here. The volumetric flow ratios Q at steady states are computed first (see Figure 3.9), and then the real parts of rightmost eigenvalues are computed at each steady state against varying diameters of branch A (see Figure 3.10a and Figure 3.10b).
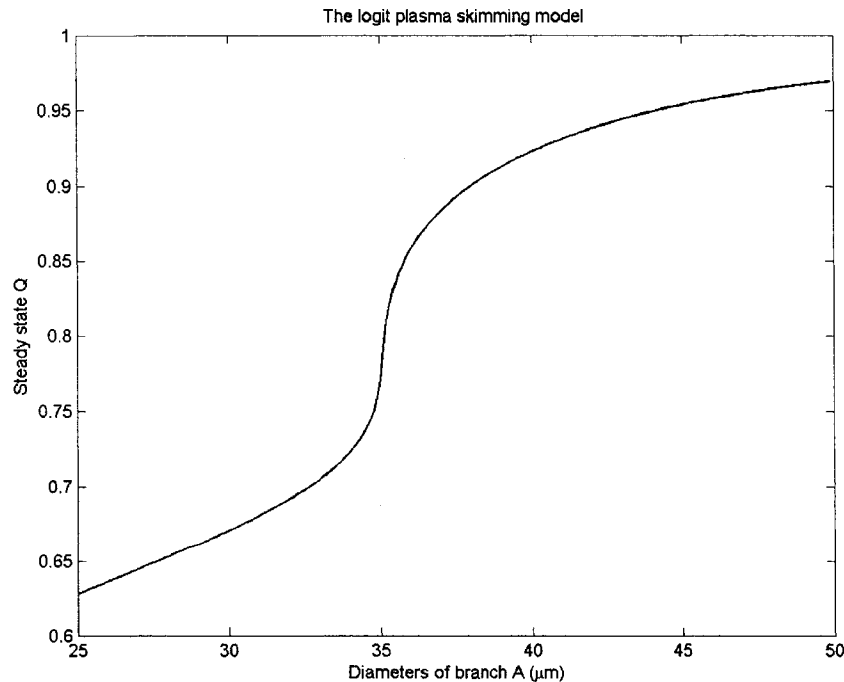
Figure 3.9   Steady States Q versus Diameter of Branch A.
Other physical parameters are Logit plasma skimming parameter $p = 2.0$, $H_I = 0.8$, $Q_I = 10$nl/min, $d_B = 20\mu$m, $l_A = 500\mu$m, $l_B = 2500\mu$m.

49

The logit plasma skimming model

Figure 3.10a   Re(λ) versus Diameter of Branch A with d_A Ranging from 25μm to 50μm. Other physical parameters are Logit plasma skimming parameter p = 2.0, H_I = 0.8, Q_I = 10nl/min, d_B = 20μm, l_A = 500μm, l_B = 2500μm.
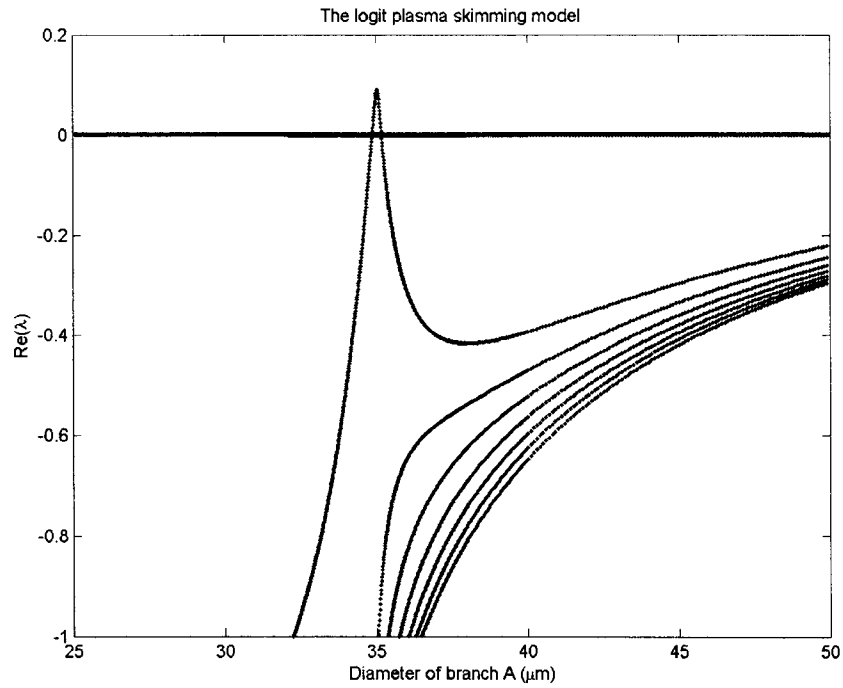
The logit plasma skimming model
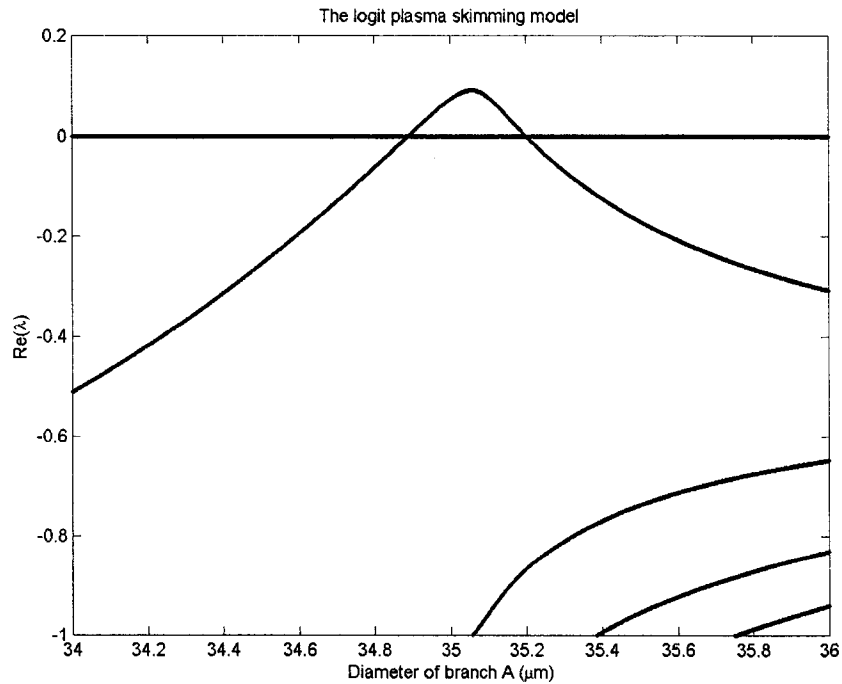
Figure 3.10b   Re(λ) Versus Diameter of Branch A with d_A Ranging from 34μm to 36μm. Other physical parameters are the same as those in Figure 3.10a.

50

Figure 3.10a and 3.10b show that when other physical parameters are fixed at certain values, the real parts of rightmost eigenvalues are positive in a narrow range of diameters of branch A (about $34.8\mu m \sim 35.2\mu m$). This means that during manufacture of micro channels, errors of diameters of branches are required to be controlled under half a micron. The requirement is strict but still achievable using soft lithography methods, for it was reported that the technique can replicate features as small as 30nm (Xia et al., 1997)[59]. From Eq.(2.6.7) and Eq.(2.6.8) that define the coefficients in the characteristic equation Eq.(2.6.10), we observe the information of diameters are integrated in the viscosity correlations, and one of coefficients contains the sixth power of diameter ratio. Thus, it is reasonable to find the rightmost eigenvalues are sensitive to the diameters. However, the wide ranges of the diameters corresponding oscillations are still preferable to the narrow ones, because the experimental systems are easier to be built.

3.5 Effects of Lengths of Branches

The influence of lengths of branches on the stability of the systems is investigated in this part. The length of branch A (see Figure 2.2) is varied, and meanwhile the diameter of branch B and other physical parameters are kept constant. The values of these fixed parameters are: $p = 2.0$, $H_I = 0.8$, $Q_I = 10$nl/min, $d_A = 35\mu m$, $d_B = 20\mu m$, $l_B = 2500\mu m$. The in vitro viscosity model and the logit plasma skimming model are both applied. The volumetric flow ratios Q at steady states are computed and plotted against varying l_A in Figure 3.11, and the real parts of rightmost eigenvalues versus varying l_A are presented in Figure 3.12.

51

Figure 3.12a and Figure 3.12b show that the system possesses rightmost eigenvalues with positive real parts and the corresponding length of branch A ranges from 470μm to 530μm. Compared with the requirements for diameters of branch A, the length during the manufacture can be easily controlled and bounded in the range using the soft lithography method.
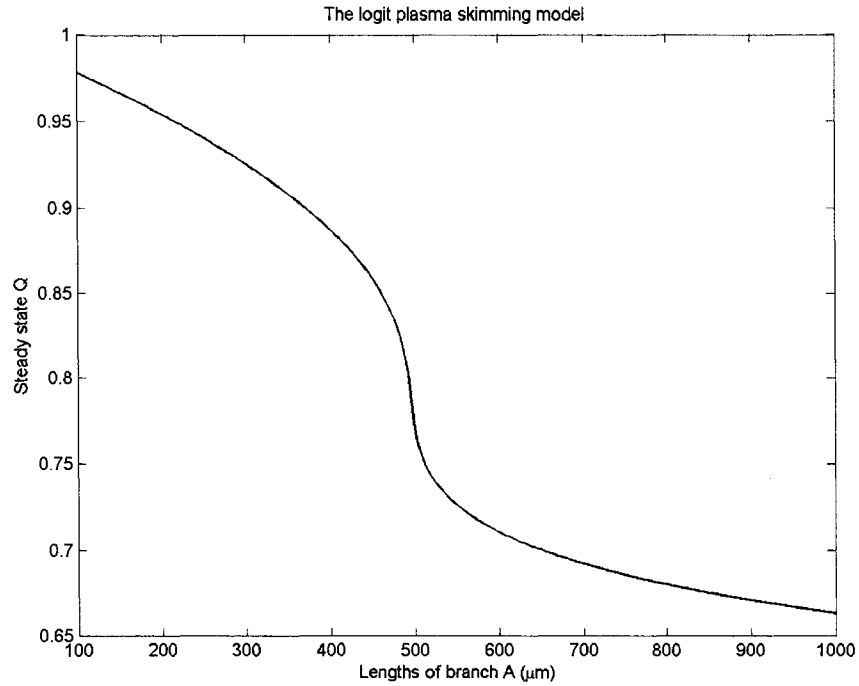
Figure 3.11 Steady States Q versus Length of Branch A.
Other physical parameters are Logit plasma skimming parameter $p = 2.0$, $H_1 = 0.8$, $Q_I = 10$nl/min, $d_A = 35\mu$m, $d_B = 20\mu$m, $l_B = 2500\mu$m.
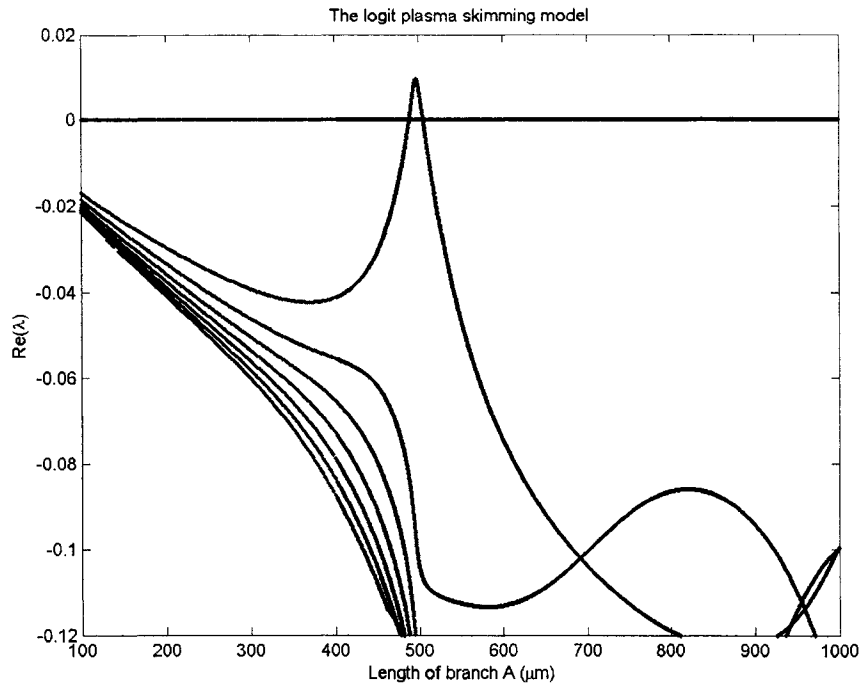
Figure 3.12a Re(λ) versus Length of Branch A with l_A Ranging from 100μm to 1000μm. Other physical parameters are Logit plasma skimming parameter p = 2.0, H_I = 0.8, Q_I = 10nl/min, d_A = 35μm, d_B = 20μm, l_B = 2500μm.
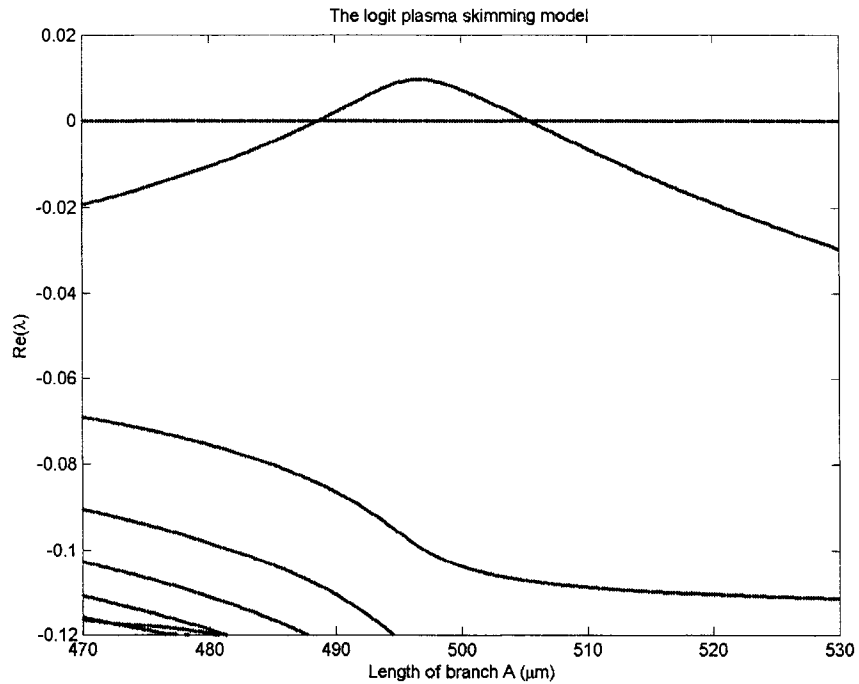
Figure 3.12b Re(λ) versus Length of Branch A with l_A Ranging from 470μm to 530μm. Other physical parameters are the same as those in Figure 3.12a.

53

3.6 Instability Regions of the Two Node Network

The proceeding work in this chapter has focused on the effects of a physical parameter on the stability of the two node microvascular network around steady states. It is meaningful to generate plots that illustrate regions of instability on two dimensional parameter spaces. The plasma skimming parameter p and inlet hematocrit H_I are chosen to construct the parameter space.

The *in vitro* viscosity model and the logit plasma skimming model are applied here. The fixed parameters are listed as following: Q_I = 10nl/min, d_A = 35μm, d_B = 20μm, l_A = 500μm, l_B = 2500μm. The results are presented in Figure 3.13, and it is noticed that the instability region on the p-H_I plane is very narrow and hints at the potential difficulties for future experimental verifications.
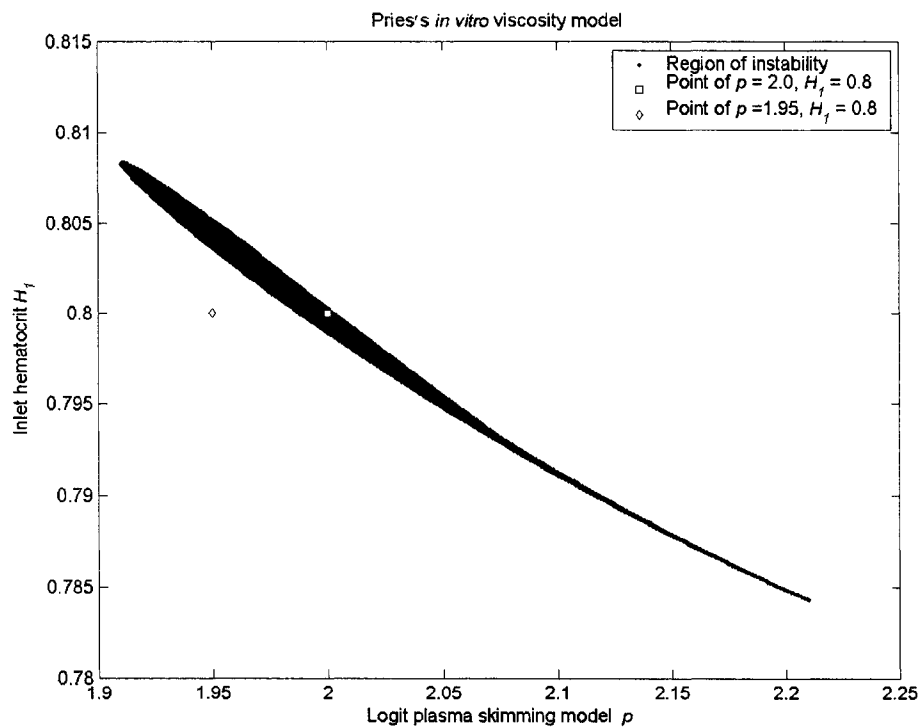
Figure 3.13 An Instability Region in the p-H_I Plane.
The other fixed parameters are: the logit plasma skimming model, the *in vitro* viscosity model, Q_I = 10nl/min, d_A = 35μm, d_B = 20μm, l_A = 500μm, l_B = 2500μm.

54

To verify the predicted stability on Figure 3.13, Carr and LeCoin's procedure can be followed to generate numerical simulation results (Carr and LeCoin, 2000)[1]. A point within the instability region in Figure 3.14a is checked, the pressure at node 1 is plotted against increasing time and initially all branches are filled with blood at a steady state hematocrits.

To illustrate the dynamics structure more clearly, Figure 3.14b presents a phase portrait with averaged hematocrits in branch A and branch B as parameters, which show the dynamics of the two node system. Obviously, a spontaneous fluctuation of pressure at node 1 occurs even without biological controls, and the oscillation appears to have a single frequency. On the phase portrait, the dynamic structure looks like a stable limit cycle where any trajectory starting from inside or outside finally approaches it. Limit cycles are necessarily due to nonlinear dynamics and never occurs in a linear system (Strogatz, 2000)[38]. The limit cycle seems like a two dimensional one, but the time series coming from simulations need to be analyzed by calculating correlation dimensions (Grassberger and Procaccia, 1983)[60], which may be a part of future work on the nonlinear dynamics of microvascular blood flow.

It is of interest to estimate an initial growth rate of pressure change at node 1. As shown in Figure 3.14c, the initial doubling time estimated from the simulation results is $T_{1/2} \approx 117.4 - 98.0 = 19.4(\text{sec})$. Also, the doubling time can be computed from the obtained rightmost eigenvalues $\lambda = 0.012103 \pm 0.089663i$ for the given physical parameters (refer to section 2.7). The computed doubling time is

$T_{1/2}{}^{*} = \dfrac{\ln 2}{\text{Re}(\lambda)} \approx 57.3(\text{sec})$. There may be several potential reasons for unmatched

values of the doubling time: 1) Steady-state solutions are not accurate enough. Generally, errors of flow ratio at steady states are controlled within +/-0.0001, but at

55

high hematocrits, a small change of the steady states may lead to a considerable change of resistance in each branch, and then of pressure at nodes; 2) In this dissertation, resistance of inlet and outlet branches are not considered, while Carr and LeCoin's simulation program did include information of the inlets and outlets. Even though influences of the inlets and outlets could be weakened by shortening their length, some small deviations still existed; 3) As for the computed rightmost eigenvalue, its imaginary part is not close to zero, which means the growth rate computed from the real part may be different from observed simulation results. In any future *in vitro* experiments, it will be meaningful to compare time scales of predicted doubling time with those of external disturbances to examine validity of the simplified mathematical models.
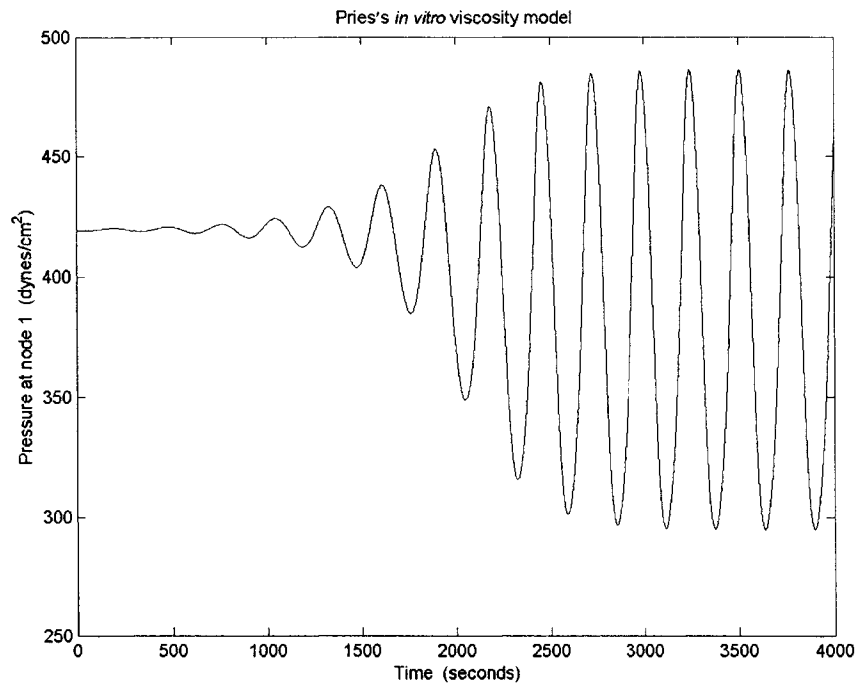
Figure 3.14a   Time Series showing the Fluctuation of Pressure at Node 1.
The other fixed parameters are: the logit plasma skimming model, the *in vitro* viscosity model, $p = 2.0$, $H_I = 0.8$, $Q_I = 10\text{nl/min}$, $d_A = 35\mu\text{m}$, $d_B = 20\mu\text{m}$, $l_A = 500\mu\text{m}$, $l_B = 2500\mu\text{m}$.

56
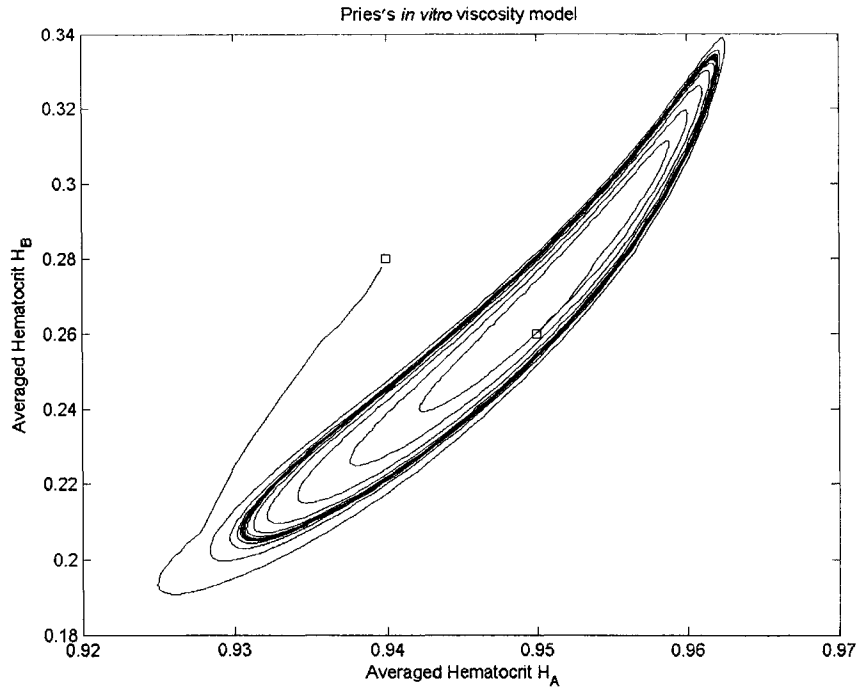
Figure 3.14b **A Phase Portrait with Averaged H_A and Averaged H_B as Parameters.** The other fixed parameters are the same as those in Figure 3.14a.
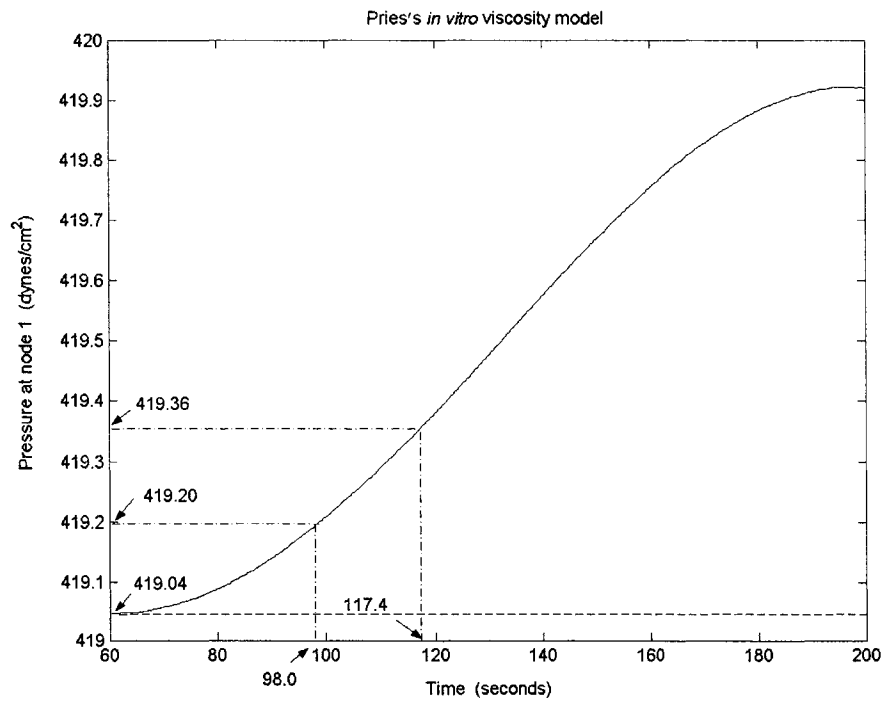
Figure 3.14c **Estimation of the Doubling Time from the Simulation Result.** The other fixed parameters are the same as those in Figure 3.14a.

57

A point outside the instability region is examined by the simulation program directly. The time series of pressure at node 1 is shown in Figure 3.15. Logit plasma skimming parameter is changed to $p = 1.95$, and other parameters keep constant as in Figure 3.14a. The initial hematocrit in each branch is around the steady state approximately. After a tiny fluctuation at the beginning, the pressure at node 1 gets back to the steady state. The result verifies the prediction and indicates again that the two node system is very sensitive to change of physical parameters.

When the plasma skimming model is switched to the linear model, while keeping the same viscosity model and physical parameters, there is no instability region found on the p - H_I plane. It seems that if the nonlinearity of the plasma skimming model is lost, the two node system tends to be always stable at steady states.
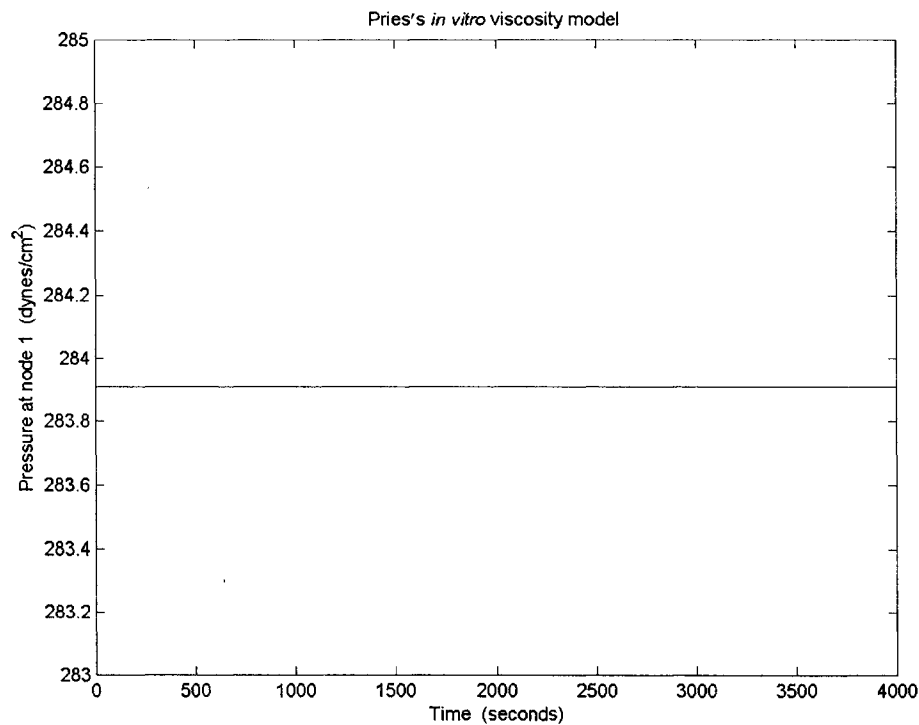
Figure 3.15   Time Series Showing Stable Pressure at Node 1.
The other fixed parameters are the same as those in Figure 3.14a.

58

3.7 Necessary Conditions for Spontaneous Oscillations

By analyzing the linearized DDE Eq.(2.6.6) for the two node topology necessary conditions for oscillations can be found (Carr et al., 2005)[48]. Note that some definitions in Carr et al.'s paper are slightly different from the ones presented in Eq.(2.6.7) and Eq.(2.6.8), and the necessary conditions are listed below:

$$-bc > 0 \tag{3.7.1}$$

$$-bc(1-\gamma)^2 > 1. \tag{3.7.2}$$

In fact, as a dimensionless time, γ is always greater than zero, so the condition Eq.(3.7.2) contains the information in Eq. (3.7.1).

The less strict necessary condition Eq.(3.7.1) indicates b and c possess opposite signs. If the definitions of b and c are examined in Eq.(2.6.7) and Eq.(2.6.8) respectively, it is found that all items are always positive except in Eq.(2.6.7) for b

$$\frac{dF}{dQ}\Big|_{\bar{Q}} - \frac{F}{Q}\Big|_{\bar{Q}} = \frac{d(F/Q)}{dQ}\Big|_{\bar{Q}} = \frac{d(H_A/H_1)}{dQ}\Big|_{\bar{Q}} \tag{3.7.3}$$

and in Eq.(2.6.8) for c

$$\frac{dF}{dQ}\Big|_{\bar{Q}} - \frac{1-F}{1-Q}\Big|_{\bar{Q}} = -\frac{d((1-F)/(1-Q))}{dQ}\Big|_{\bar{Q}} = -\frac{d(H_B/H_1)}{dQ}\Big|_{\bar{Q}}. \tag{3.7.4}$$

If the inlet hematocrit ratio is plotted against the flow ratio Q, the graph may show regions satisfying the necessary condition Eq.(3.7.1). An example is presented in Figure 3.16a, where Logit plasma skimming model is applied and the plasma skimming parameter p is equal to 2.0. With the given p, two critical values of flow ratio Q are computed: $Q_{cr1} \approx 0.2929$, $Q_{cr2} \approx 0.7071$. The left shaded region is located between 0 and Q_{cr1}, where $b > 0$, $c < 0$, and $-bc > 0$; the right shaded region is located between Q_{cr2} and 1, where $b < 0$, $c > 0$, and $-bc > 0$; the middle un-shaded region is located between Q_{cr1} and Q_{cr2}, where $b > 0$, $c > 0$ and $-bc < 0$. Thus, the

59

first necessary condition for oscillation is not obeyed in the un-shaded region and no oscillation can occur there.

To verify the necessary conditions, each point satisfying the conditions is plotted in the p-H_I plane (see Figure 3.17). All fixed parameters and related models are the same as those in Figure 3.13. From the Figure 3.17, it is noticed that the region of instability is bounded in the parameter space where both necessary conditions for oscillations are satisfied.

When the plasmas skimming model is changed to the linear model, the inlet hematocrit ratio is plotted versus the flow ratio Q in Figure 3.16b. Also two critical values are calculated: $Q_{cr1} = 0.25$, $Q_{cr2} = 0.75$. When $0 < Q < Q_{cr1}$, $b = 0$, $c < 0$, and $bc = 0$; when $Q_{cr1} < Q < Q_{cr2}$, $b > 0$, $c > 0$, and $bc > 0$; when $Q_{cr2} < Q < 1$, $b < 0$, $c = 0$, and $bc = 0$. Obviously, the necessary condition Eq.(3.7.1) is satisfied nowhere for the two node system when the linear plasma skimming model is applied. Therefore, this system will always be stable.

The logit plasma skimming model
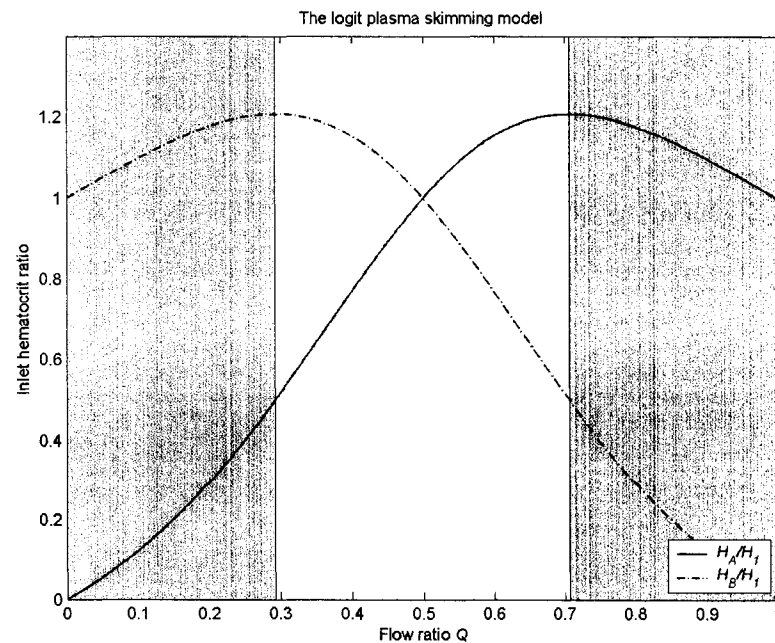
Figure 3.16a   Inlet Hematocrit Ratio versus Flow Ratio Q when Logit Plasma Skimming Parameter p = 2.0. Shadowed area corresponds to oscillation regions.

60
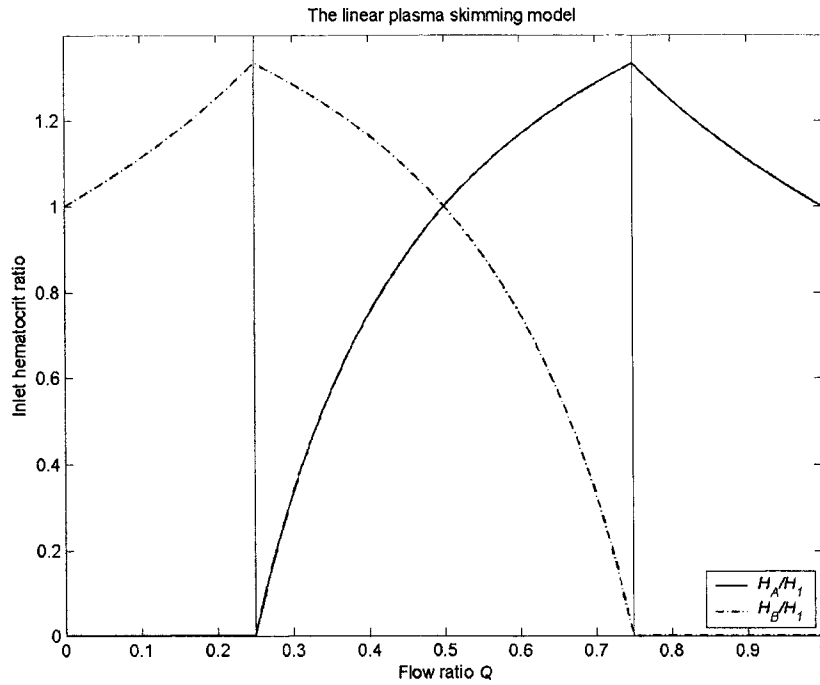
Figure 3.16b Inlet Hematocrit Ratio versus Flow Ratio Q when Linear Plasmas Skimming Parameter $p = 2.0$.
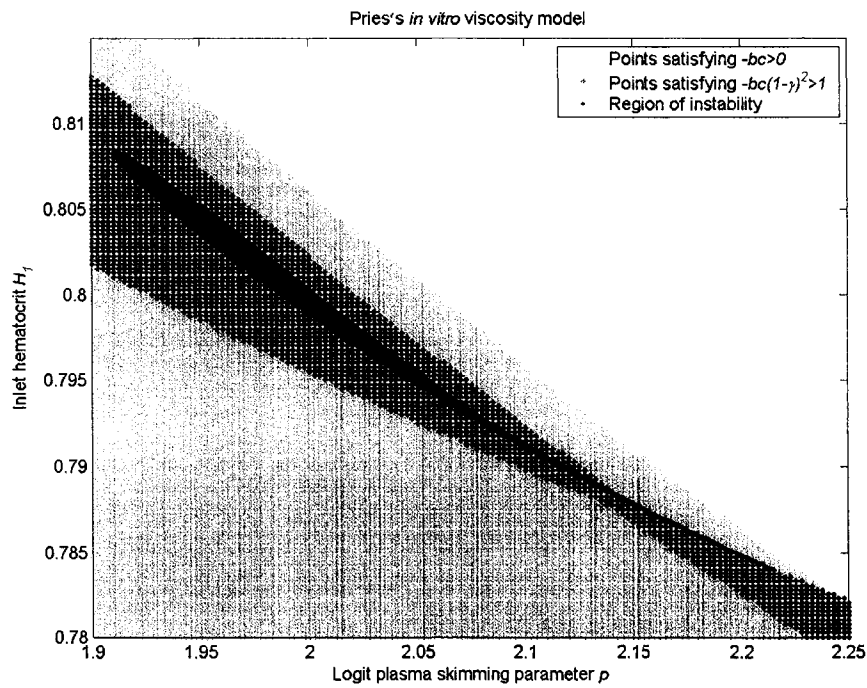
Figure 3.17 Points Satisfying Necessary Conditions for oscillations in the p-H_1 Plane. All fixed parameters and related models are the same as those in Figure 3.13.

61

CHAPTER IV

NUMERICAL RESULTS ABOUT THREE NODE MICROVASCULAR NETWORKS

The numerical studies in the last chapter show that parameter spaces of possible oscillations are quite narrow and hint that experimental verification for those theoretical predictions may be difficult. Therefore, it is reasonable to move to more complicated topological structures such as three node network with two inlets (see Figure 2.3), where a practical system for experiments is hoped to be found. Again, DDE-BIFTOOL is applied during the numerical investigation. Carr and LeCoin's simulation program is again used to examine stability of the system. Pries's *in vitro* viscosity model is applied in this chapter.

Through the first five sections (from Section 4.1 to Section 4.5), effects of geometry and inlet conditions are investigated in symmetric systems. Advantages of investigating a symmetric system are as follows.

First, the number of investigated parameters is reduced greatly. For an asymmetric system, there are ten parameters for analysis – d_A, d_B, d_C, l_A (or l_B), l_C, H_1, H_2, Q_1 (or Q_2), p_1, p_2, etc; while for a symmetric system, the number of the parameters are decreased to five, and they are d_A (or d_B), d_C, l_C/l_A (or l_C/l_B), H_1 (or H_2), and p_1 (or p_2).

62

Second, since the symmetric system is defined to have symmetric geometry as well as symmetric inlet conditions, it always possesses a trivial steady state – no blood flow in branch C, and other existing steady states appear in pairs. Theoretically the paired steady states have exactly the same stability, thus investigation of half of the steady states will suffice.

Third, experimental models for the symmetric system can be built more easily than for an asymmetric system.

To have a preliminary idea about asymmetric systems, effects of heterogeneity of inlet conditions on dynamics are studied for the three node system in Section 4.6.

4.1 Effects of Plasma Skimming Parameters

It is found that in the two node network, the steady states and corresponding stability are sensitive to the plasma skimming model and the plasma skimming parameter applied. For the three node network, the effects of plasma skimming models and parameters are under investigation. Likewise, both the linear model (Fenton et al., 1985)[20] and the logit model (Dellimore et al., 1983)[21] are examined for the three node system. The investigation is performed in geometrically symmetric systems with identical inlet conditions in two inlet branches. To avoid destroying the symmetry, the plasma skimming parameters at node 1 and node 2 are always changed simultaneously, i.e., $p_1 = p_2$.

Pries's in vitro viscosity model is used during the investigation. Other physical parameters are $H_1 = H_2 = 0.8$, $Q_1 = Q_2 = 10$nl/min, diameters $d_A = d_B = 35\mu$m, $d_C = 50\mu$m, lengths $l_A = l_B = 500\mu$m, $l_C = 1000\mu$m. The steady state $\tilde{Q}^* = Q_A /(Q_1 + Q_2)$ is plotted against varying plasma skimming parameters p_1, p_2 for the two models in Figure 4.1 and Figure 4.2 respectively. In these figures, a black point denotes stable

63

one and a grey point denotes unstable one. At $Q^* = 0.5$, the stability is always uncertain due to the functional limitation of DDE-BIFTOOL.

Both of the above two graphs present only slight differences in the shapes of the Q-p curves. This is reasonable since the computed steady state flow ratios fall in the central regions of the plasma skimming graphs where the two are similar However, the unstable steady states appear at lower values of the plasma skimming parameter for the linear model than for the logit model.

It is also noticed from Figure 4.1 and Figure 4.2 that there are two symmetric branches of steady states and a middle one corresponding to steady states $Q^* = 0.5$, which means no blood flow in the branch C at the steady states. At steady states $Q^* = 0.5$, the coefficients in Eq.(2.6.5) are calculated to be zero, with which DDE-BIFTOOL fails to continue the further computation and thus the corresponding stability is undetermined. It is sufficient to compute the rightmost eigenvalues along one of branches of non-zero steady states due to their symmetry. The rightmost eigenvalues versus the plasma skimming parameters for both models are presented in Figure 4.3 and Figure 4.4 respectively.

The linear plasma skimming model
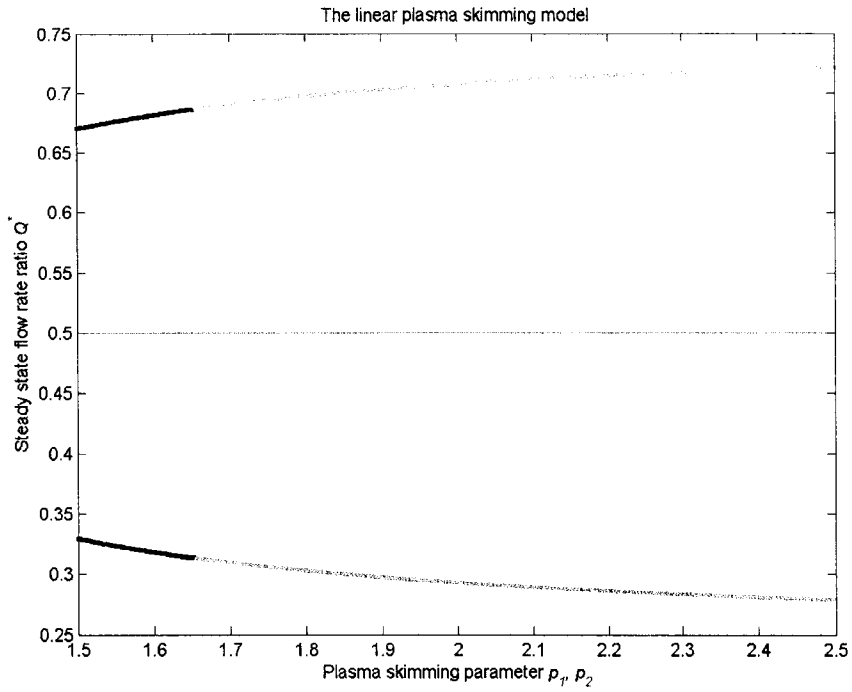
Figure 4.1   Steady State Q^* versus Linear Plasma Skimming Parameter.
Other physical parameters are $H_1 = H_2 = 0.8$, $Q_1 = Q_2 = 10\text{nl/min}$, $d_A = d_B = 35\mu\text{m}$, $d_C = 50\mu\text{m}$, lengths $l_A = l_B = 500\mu\text{m}$, $l_C = 1000\mu\text{m}$.

The logit plasma skimming model
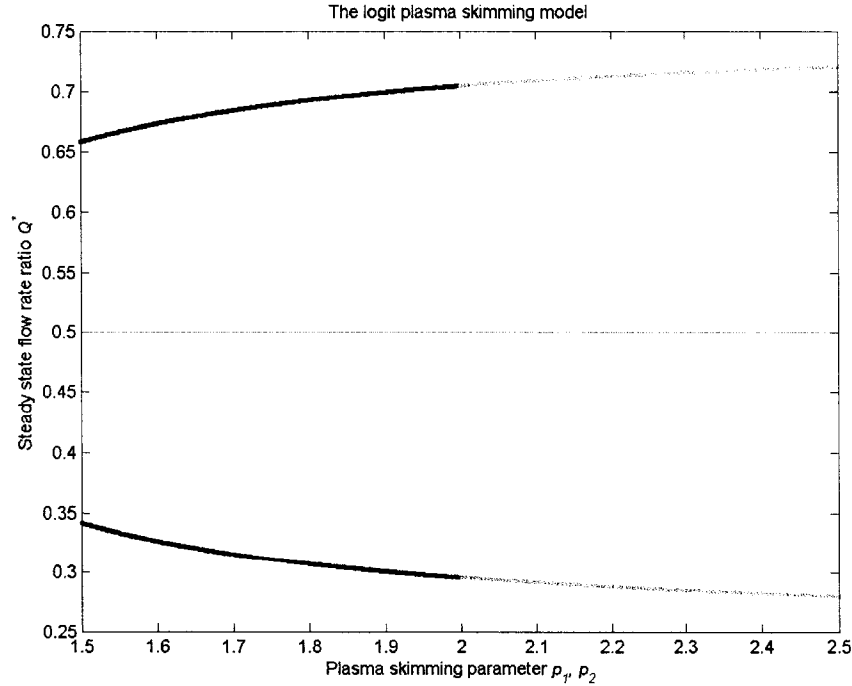
Figure 4.2   Steady State Q^* versus Logit Plasma Skimming Parameter.
Other physical parameters are $H_1 = H_2 = 0.8$, $Q_1 = Q_2 = 10\text{nl/min}$, $d_A = d_B = 35\mu\text{m}$, $d_C = 50\mu\text{m}$, lengths $l_A = l_B = 500\mu\text{m}$, $l_C = 1000\mu\text{m}$.

65

The linear plasma skimming model

Figure 4.3   Re(λ) versus Linear Plasma Skimming Parameter.
Other physical parameters are $H_1 = H_2 = 0.8$, $Q_1 = Q_2 = 10$nl/min, $d_A = d_B = 35\mu$m, $d_C = 50\mu$m, lengths $l_A = l_B = 500\mu$m, $l_C = 1000\mu$m.

The logit plasma skimming model

Figure 4.4   Re(λ) versus Logit Plasma Skimming Parameter.
Other physical parameters are $H_1 = H_2 = 0.8$, $Q_1 = Q_2 = 10$nl/min, $d_A = d_B = 35\mu$m, $d_C = 50\mu$m, lengths $l_A = l_B = 500\mu$m, $l_C = 1000\mu$m.

66
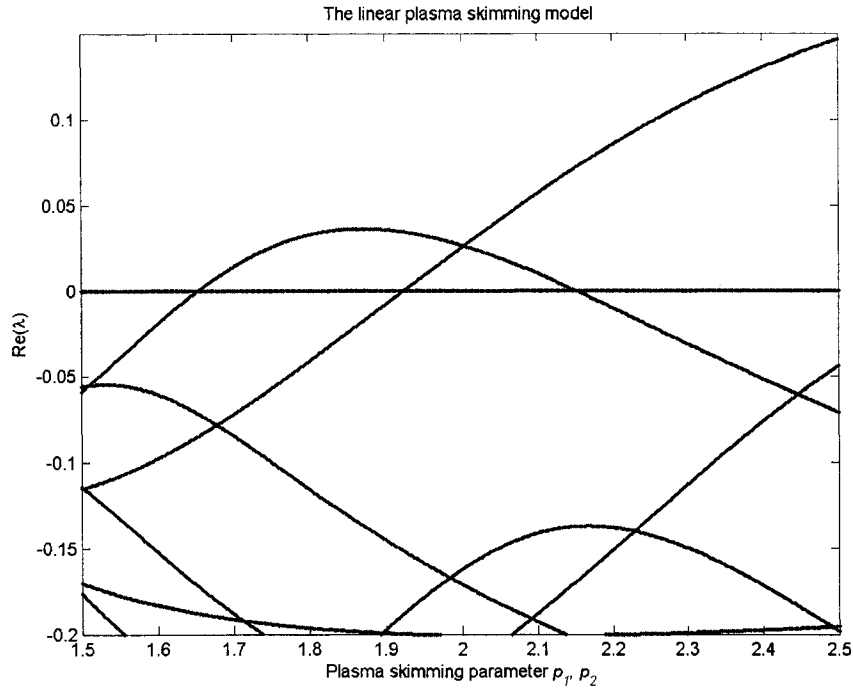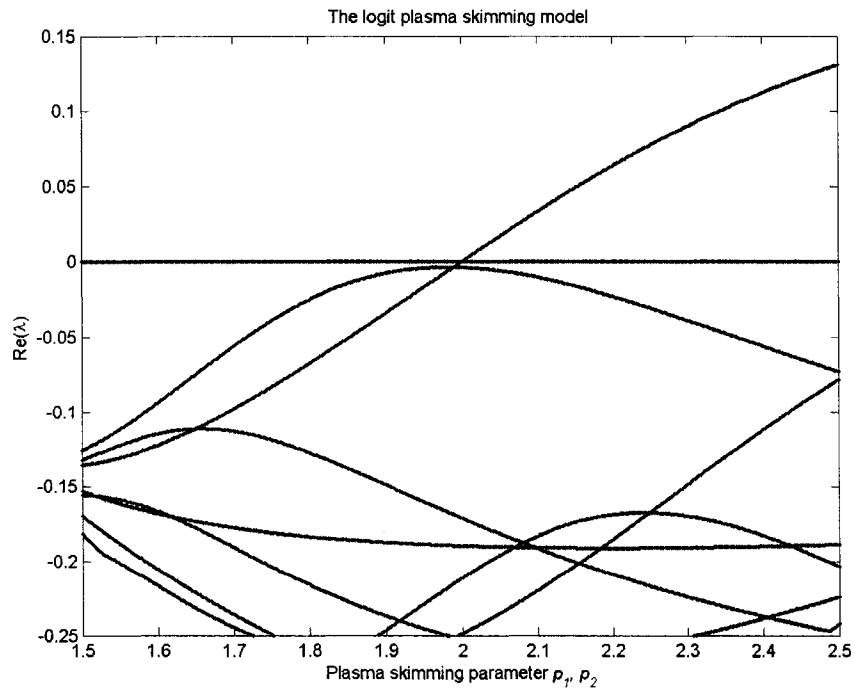
The results of Figure 4.3 and Figure 4.4 explain why the linear model has a wider range of plasma skimming parameters corresponding to unstable steady states. There are two branches of eigenvalues whose real parts are greater than zero in Figure 4.3, but only one branch of eigenvalues has positive real parts in Figure 4.4. Figure 4.3 also shows that the two positive eigenvalue branches exist simultaneously where p ranges from about 1.9 to about 2.2. When the imaginary parts corresponding to the two branches are plotted against p in Figure 4.5, it is found that the two branches possess different imaginary parts in the overlapping range. When the real parts are greater than zero, the value of an imaginary part is related to oscillation frequencies. Oscillations with two frequencies are anticipated. This has been checked with the simulation program.
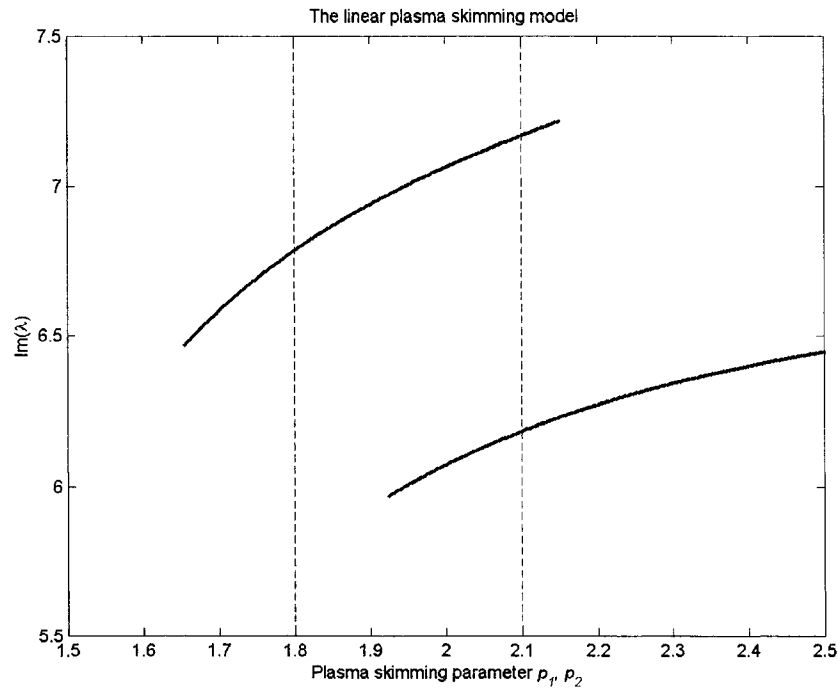
Figure 4.5 Im(λ) versus Linear Plasma Skimming Parameter for Positive Eigenvalue Branches. Other physical parameters are $H_1 = H_2 = 0.8$, $Q_1 = Q_2 = 10$nl/min, $d_A = d_B = 35\mu$m, $d_C = 50\mu$m, lengths $l_A = l_B = 500\mu$m, $l_C = 1000\mu$m.

67

Linear plasma skimming parameter $p_1 = p_2 = 1.8$

Pressure at node 1 (dynes/cm^2)

Time (seconds)
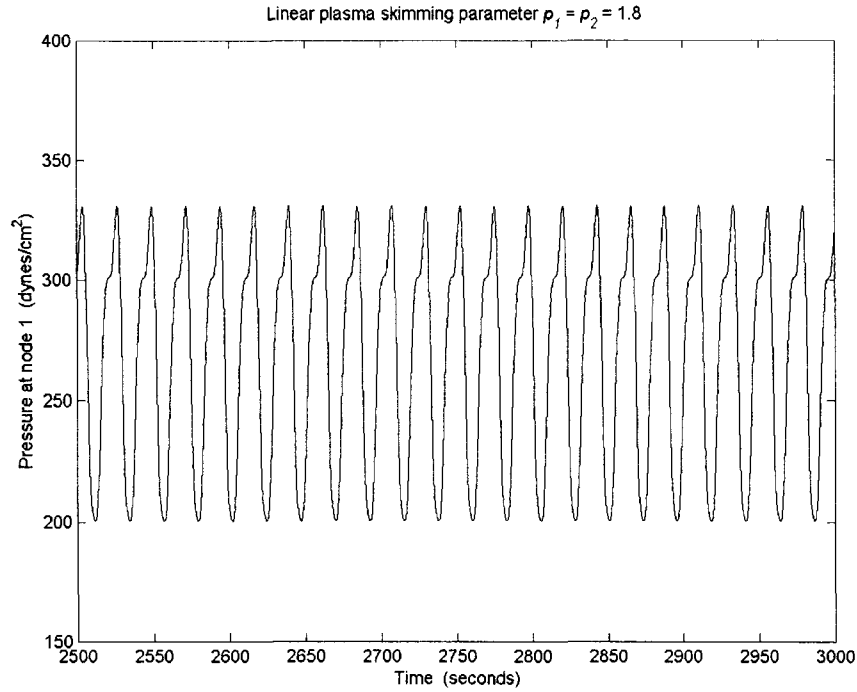
Figure 4.6a Time Series Showing Fluctuation of Pressure at Node 1 when p_1 = p_2 = 1.8. The linear plasma skimming model. Other physical parameters are $H_1 = H_2$ = 0.8, $Q_1 = Q_2$ = 10nl/min, $d_A = d_B$ = 35μm, d_C = 50μm, lengths $l_A = l_B$ = 500μm, l_C = 1000μm.

Linear plasma skimming parameter $p_1 = p_2 = 2.1$

Pressure at node 1 (dynes/cm^2)

Time (seconds)

Figure 4.6b Time Series Showing Fluctuation of Pressure at Node 1 when p_1 = p_2 = 2.1. Other physical parameters are the same as those in Figure 4.6a.

68

The point at $p_1 = p_2 = 1.8$ and 2.1 are checked respectively. At $p_1 = p_2 = 1.8$ only one frequency is expected, while two frequencies are expected at $p_1 = p_2 = 2.1$. The simulation program proceeds for enough time so that the dynamic behavior develops completely. The time series of pressure at node 1 are plotted in Figure 4.6(a,b). It is found that Figure 4.6a only presents the oscillation with a single frequency. In contrast, Figure 4.6b shows the oscillation at $p_1 = p_2 = 2.1$ with two frequencies as predicted.

4.2 Effects of Inlet Hematocrits

As stated previously, it is expected that oscillations will occur at a lower inlet hematocrit and wider ranges of inlet hematocrit for the three node network than for the two node network. Thus, the effects of inlet hematocrits on the hemodynamics are studied here. Pries et al.'s in vitro viscosity model and the logit plasma skimming model are applied. To utilize the symmetric properties of the three node system, the two inlet hematocrits and the plasma skimming parameters at two inlet nodes are chosen to be identical, and the diameters and lengths of branch A and branch B are the same as well.

First, the steady state flow ratio Q^* is plotted against the varying inlet hematocrits (see Figure 4.7), and different line styles represent unstable, stable, and undetermined stability at steady state. The fixed physical parameters are $p_1 = p_2 = 2.0$, $Q_1 = Q_2 = 10\text{nl/min}$, diameters $d_A = d_B = 35\mu\text{m}$, $d_C = 50\mu\text{m}$, lengths $l_A = l_B = 500\mu\text{m}$, $l_C = 1000\mu\text{m}$.
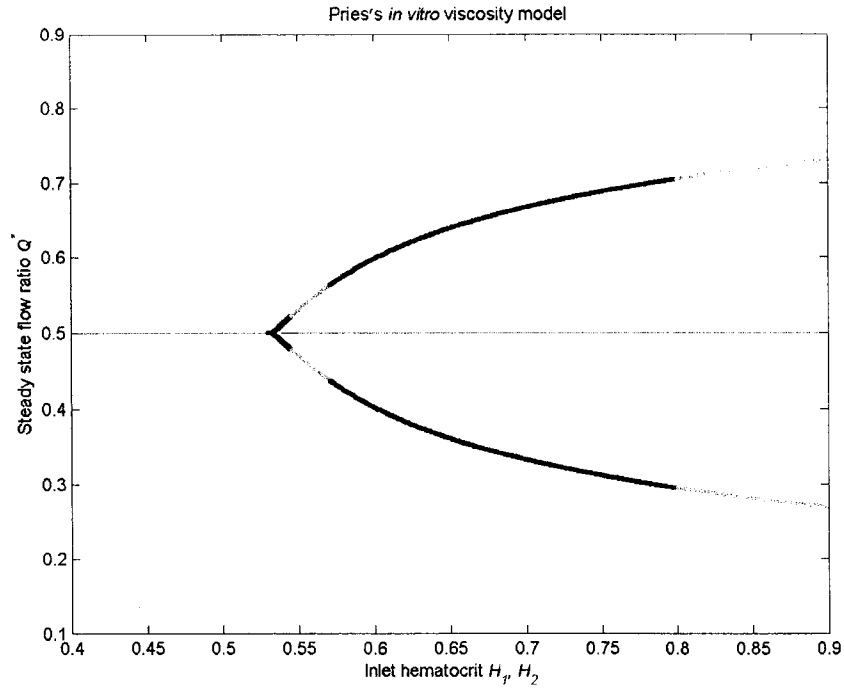
Figure 4.7 Steady State Q^* versus Inlet Hematocrit H_1, H_2.
Other physical parameters are the logit plasma skimming parameters $p_1 = p_2 = 2.0$, $Q_1 = Q_2 = 10\text{nl/min}$, $d_A = d_B = 35\mu\text{m}$, $d_C = 50\mu\text{m}$, $l_A = l_B = 500\mu\text{m}$, $l_C = 1000\mu\text{m}$.
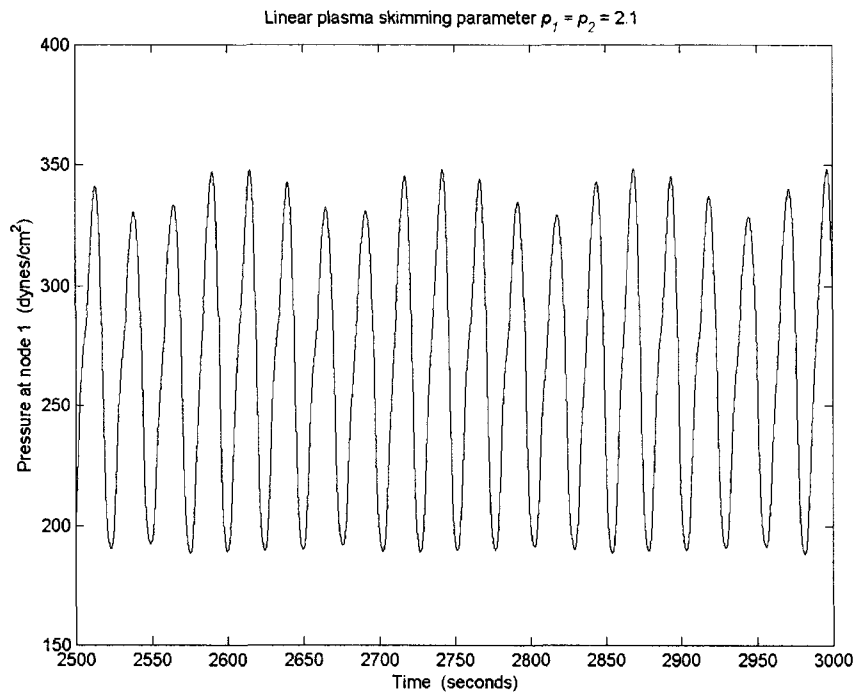
The rightmost eigenvalues are computed for one branch of non-zero steady states due to the symmetric properties of the system. The real parts of the eigenvalues are plotted against the hematocrits in both inlets in Figure 4.8, and the graph presents more details of change of eigenvalues at steady states. It is found that rightmost eigenvalues may come from various eigenvalue branches, and eigenvalues on one branch can grow to a positive value and then become negative as hematocrits increase.

70

Pries's *in vitro* viscosity model
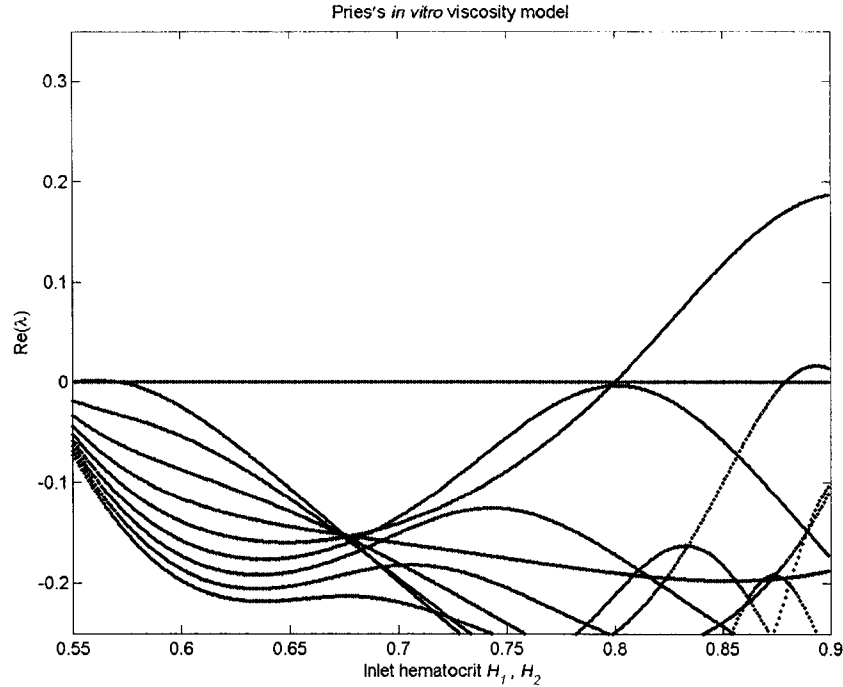
Figure 4.8   Re(λ) versus Inlet Hematocrit H_1, H_2.
The other parameters are the logit plasma skimming parameters $p_1 = p_2 = 2.0$, $Q_1 = Q_2 = 10\text{nl/min}$, $d_A = d_B = 35\mu m$, $d_C = 50\mu m$, $l_A = l_B = 500\mu m$, $l_C = 1000\mu m$.

At the first glance, it is found that the rightmost eigenvalues with positive real parts exist around relatively low inlet hematocrits (about 0.56 to 0.58). When the simulation program is carried out at a value in that range ($H_1 = H_2 = 0.57$), no spontaneous oscillation occurs as expected (see Figure 4.9a), while at the higher inlet hematocrit values ($H_1 = H_2 = 0.80$), the oscillation with two frequencies is observed (see Figure 4.9b). The stability analysis is based on the linearized DDE's around steady states (see Eq.2.6.3), and higher order items are neglected during the linear analysis. When the real parts the rightmost eigenvalues are slightly greater than zero, the ignored higher orders may damper linear instabilities; when the real parts are slightly less than zero, the higher orders may destabilize the system at the steady states.

71
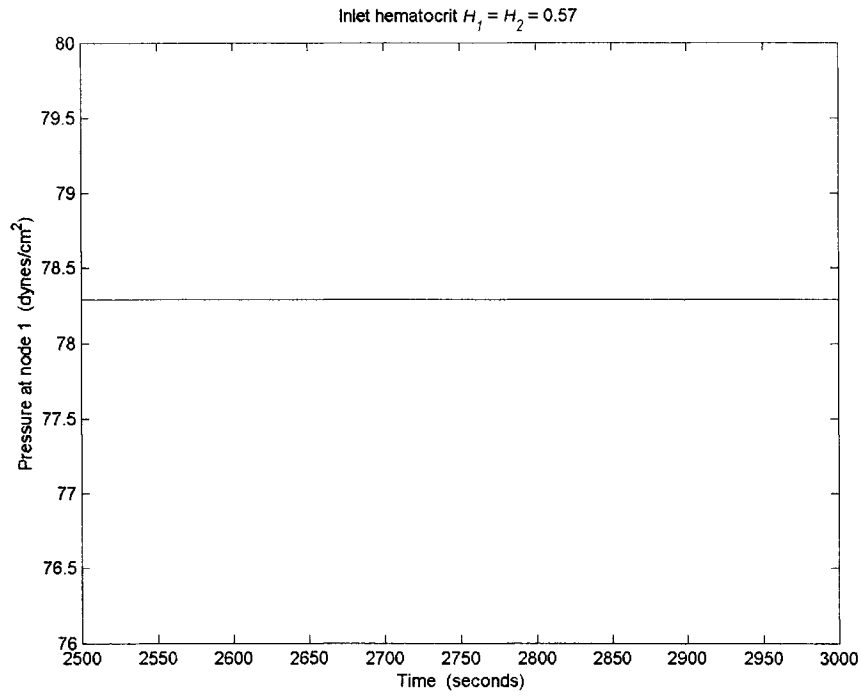
Figure 4.9a Time Series Showing Stable Pressure at Node 1 when $H_1 = H_2 = 0.57$. The other parameters are the same as those in Figure 4.8.
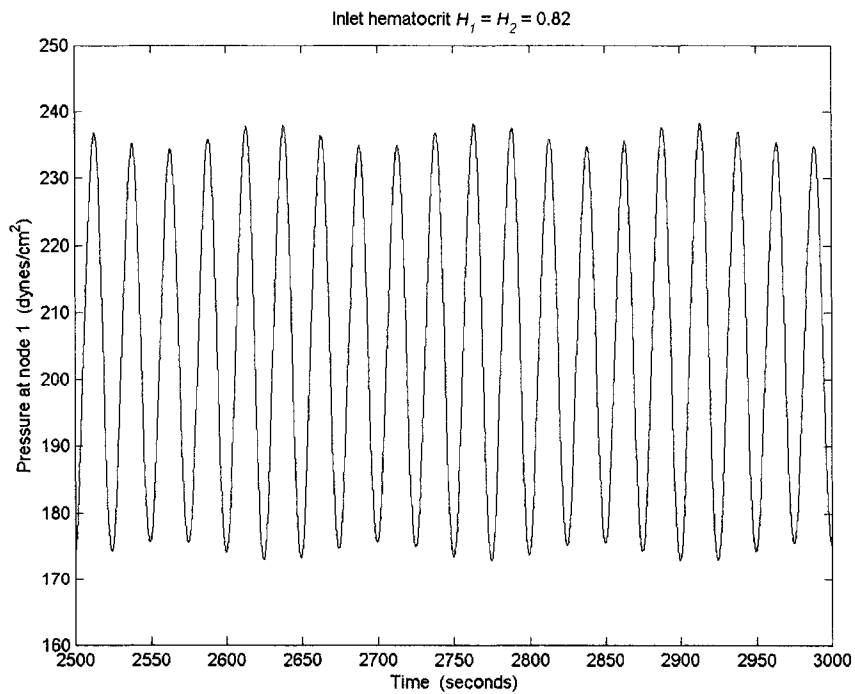
Figure 4.9b Time Series Showing Stable Pressure at Node 1 when $H_1 = H_2 = 0.82$. The other parameters are the same as those in Figure 4.8.

72

4.3 Effects of Diameter of Branch C

As pointed out in Section 3.4 and 3.5, it is important to know instability ranges of geometrical parameters for a system to determine whether it is practical to be built. In this section, effects of diameters of branch C are investigated.

The steady state flow ratio Q^* is plotted against the varying diameter of branch C in Figure 4.10 with given fixed parameters. Pries's *in vitro* viscosity model and the logit plasma skimming model are used and the constant physical parameters are: $p_1 = p_2 = 2.0$, $Q_1 = Q_2 = 10\text{nl/min}$, $d_A = d_B = 35\mu m$, $l_A = l_B = 500\mu m$, $l_C = 1000\mu m$.

As seen in the preceding parts, the symmetric system possesses two symmetric branches of steady states and one trivial branch corresponding to no blood flow in branch C. Either of the two symmetric branches of steady states is under the observation. It is found that the stability changes three times as d_C increases from $25\mu m$ to $65\mu m$: from stability to instability at $d_C \approx 40\mu m$; then from instability to stability at $d_C \approx 43\mu m$; and again from stability to instability at $d_C \approx 45\mu m$. The three instability ranges of d_C shown in Figure 4.10 are about $3\mu m$, $1.5\mu m$, and $18\mu m$ respectively. The diameters of branches can be easily controlled in these ranges via soft lithography method (Xia et al., 1998)[44].

In Figure 4.11, the real parts of the rightmost eigenvalues are plotted against the growing diameter of branch C. From the graph, it is found that multiple branches of eigenvalues become the rightmost one with positive real parts in turn, and segments corresponding to positive real parts are isolated initially, but then overlap at higher d_C values. Accordingly, the three node system possesses unstable steady states in a wider range of diameters compared with the two node topology case (see Figure 3.12a, 3.12b).

73
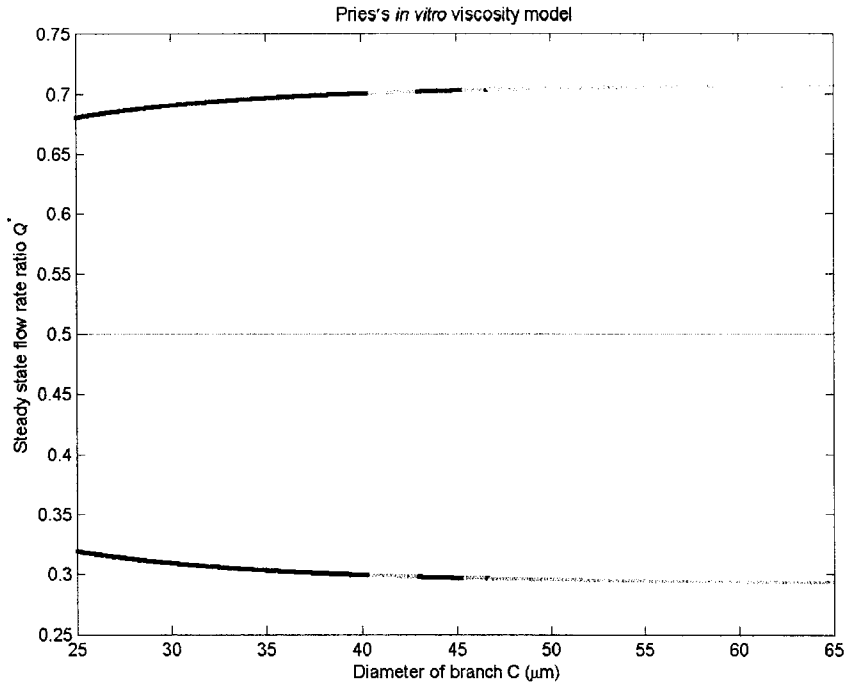
Figure 4.10 Steady State Q^* versus Diameter of Branch C.
The other parameters are the logit plasma skimming parameters $p_1 = p_2 = 2.0$, $Q_1 = Q_2 = 10\text{nl/min}$, $H_1 = H_2 = 0.8$, $d_A = d_B = 35\mu\text{m}$, $l_A = l_B = 500\mu\text{m}$, $l_C = 1000\mu\text{m}$.

**Figure 4.11 Re(λ) versus Diameter of Branch C.**
The other parameters are the logit plasma skimming parameters $p_1 = p_2 = 2.0$, $Q_1 = Q_2 = 10\text{nl/min}$, $H_1 = H_2 = 0.8$, $d_A = d_B = 35\mu\text{m}$, $l_A = l_B = 500\mu\text{m}$, $l_C = 1000\mu\text{m}$.

74
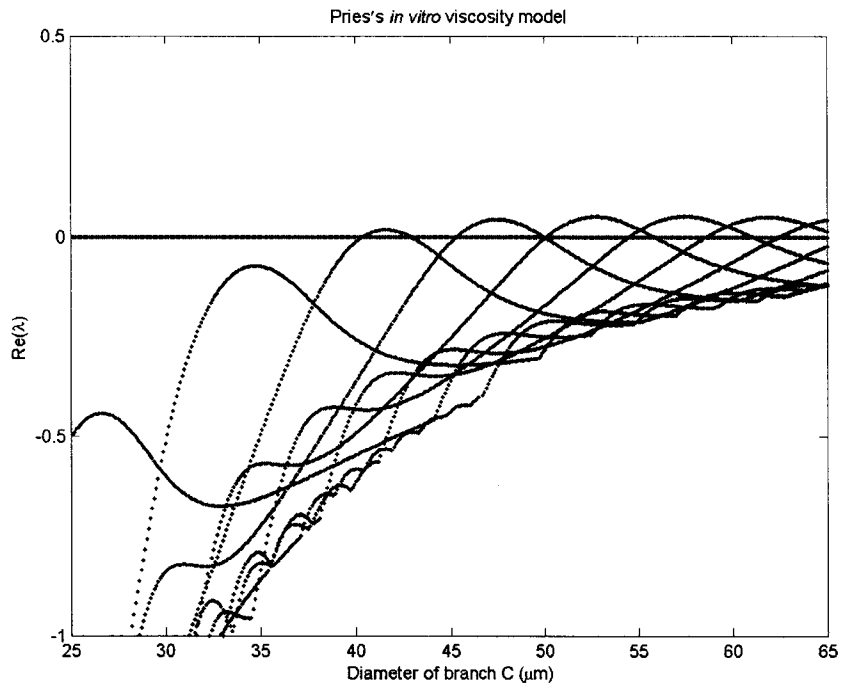
4.4 Effects of Lengths of Branch C

Another geometrical parameter examined here is the length of branch C. Pries's *in vitro* viscosity model and the logit plasma skimming model are used and the constant physical parameters are: $p_1 = p_2 = 2.0$, $Q_1 = Q_2 = 10\text{nl/min}$, $d_A = d_B = 35\mu\text{m}$, $d_C = 50\mu\text{m}$, $l_A = l_B = 500\mu\text{m}$.

The steady state flow ratio Q^* is plotted against the varying length of branch C in Figure 4.12 first. Similar to Figure 4.10, the stability at the steady states changes several times along the increasing l_C along either the upper branch or the lower branch. Interestingly, the discrete non-oscillation regions look like "windows". In Figure 4.13, the real parts of the rightmost eigenvalues are plotted versus l_C, and the non-oscillation windows exist between two branches of the rightmost eigenvalues.
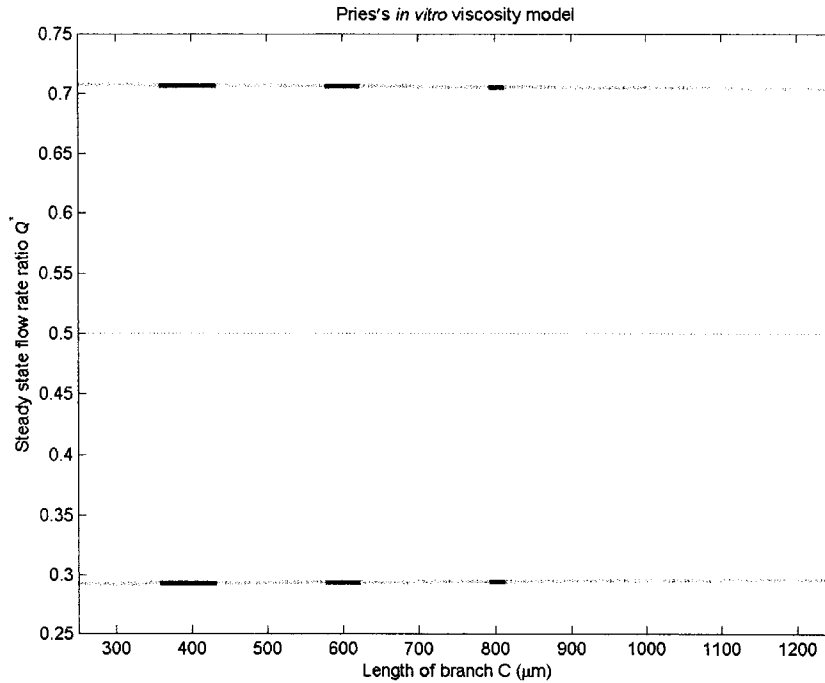
Figure 4.12 Steady State Q^* versus Length of Branch C.
The other parameters are the logit plasma skimming parameters $p_1 = p_2 = 2.0$, $Q_1 = Q_2 = 10\text{nl/min}$, $H_1 = H_2 = 0.8$, $d_A = d_B = 35\mu\text{m}$, $d_C = 50\mu\text{m}$, $l_A = l_B = 500\mu\text{m}$.

75
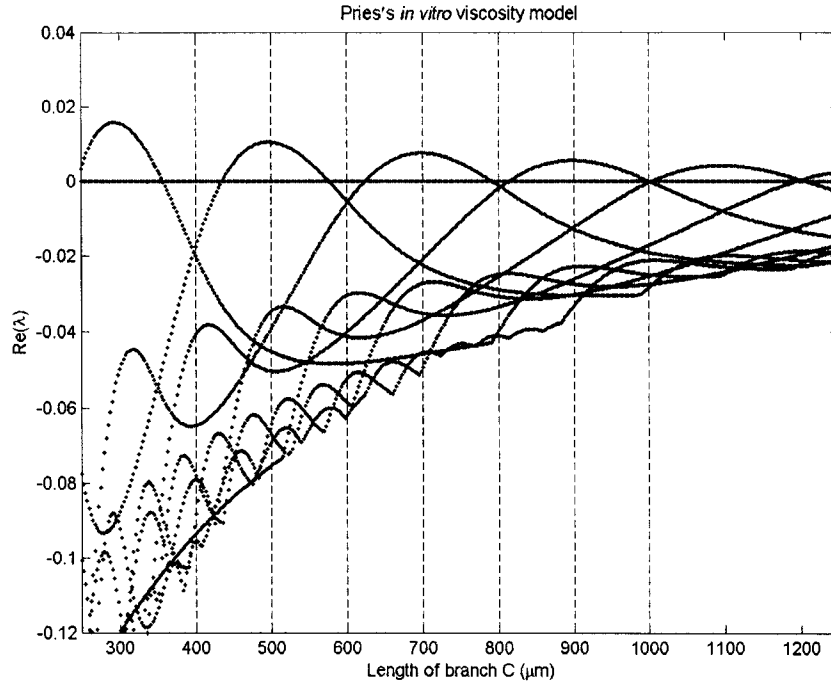
Figure 4.13 Re(λ) versus Length of Branch C.

The other parameters are the logit plasma skimming parameters $p_1 = p_2 = 2.0$, $Q_1 = Q_2 = 10$nl/min, $H_1 = H_2 = 0.8$, $d_A = d_B = 35\mu$m, $d_C = 50\mu$m, $l_A = l_B = 500\mu$m.

The simulation program is carried out to examine the stability inside and outside the non-oscillation windows, and the results are shown in Figure 4.14(a-g), which corresponds to $l_C = 400\mu$m, 500μm, 600μm, 700μm, 800μm, 900μm and 1000μm in sequence. The simulation results match the prediction very well as shown in the figures. The steady state at $l_C = 800\mu$m is supposed to be stable according to the stability analysis, but Figure 4.14e shows that oscillation with a very small amplitude still occur. As pointed out in Section 4.3, deviations may occur between the linear stability analysis and the direct numerical simulation. Figure 4.14g presents a similar situation to Figure 4.14e. The oscillation in Figure 4.14g appears to possess two frequencies, where an eigenvalue with positive part exists along with another eigenvalue with negative real part close to zero.

76

Length $l_c = 400$ (µm)

Pressure at node 1 (dynes/cm²)

240
230
220
210
200
190
180
170
160
150
140

2500 2550 2600 2650 2700 2750 2800 2850 2900 2950 3000
Time (seconds)
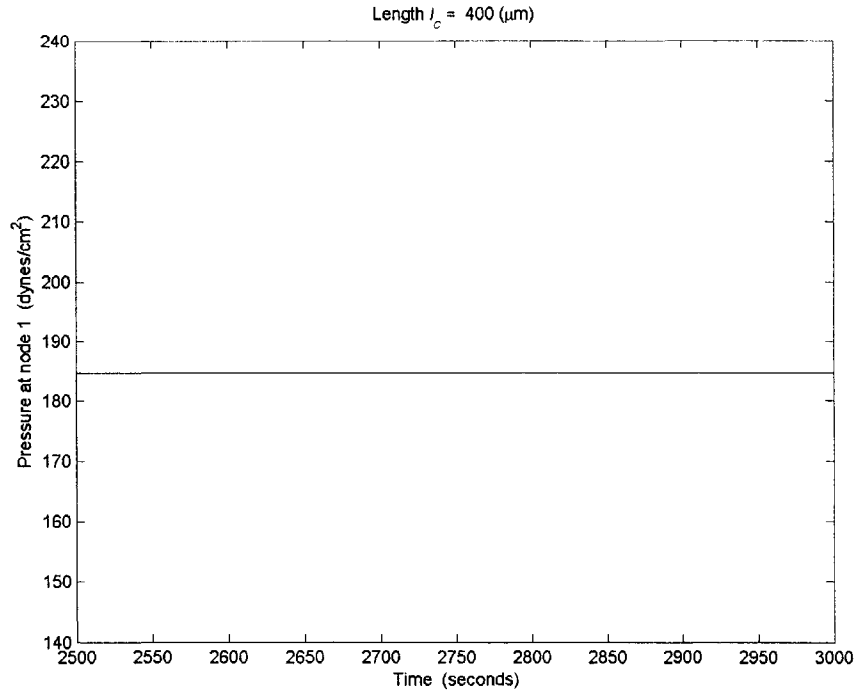
Figure 4.14a   Time series Showing Stable Pressure at Node 1 when $l_C = 400\mu$m.
The other parameters are the same as those in Figure 4.13.

Length $l_c = 500$ (µm)

Pressure at node 1 (dynes/cm²)

240
230
220
210
200
190
180
170
160
150
140

2500 2550 2600 2650 2700 2750 2800 2850 2900 2950 3000
Time (seconds)
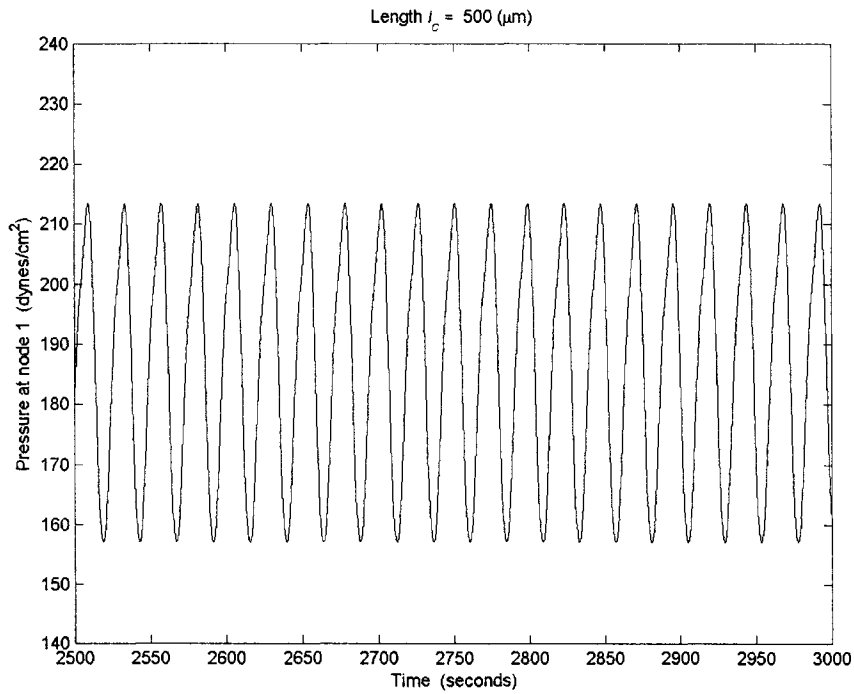
Figure 4.14b   Time series Showing Unstable Pressure at Node 1 when $l_C = 500\mu$m. The other parameters are the same as those in Figure 4.13.

77

Length l_c = 600 (μm)
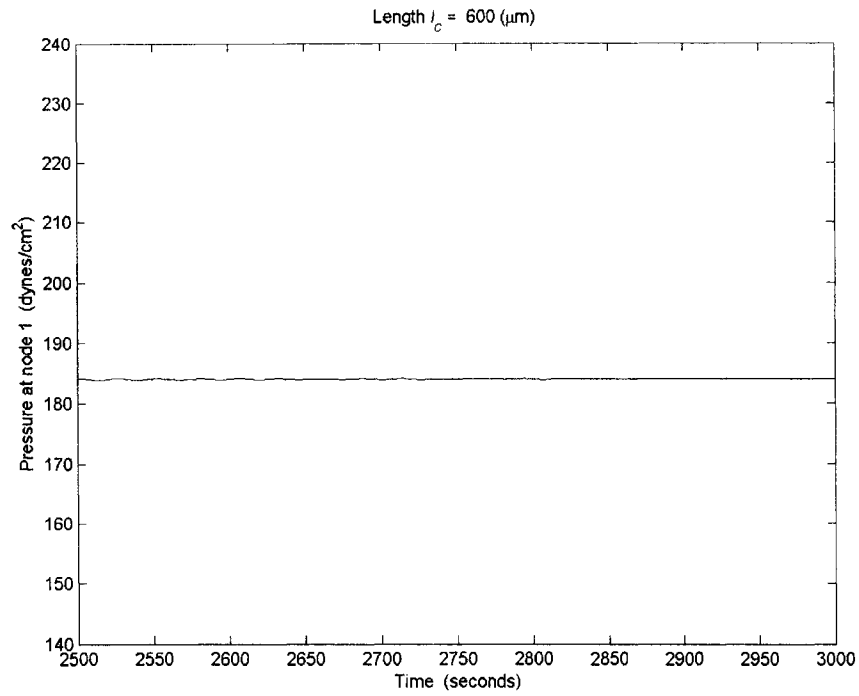
Figure 4.14c   Time series Showing Stable Pressure at Node 1 when l_C = 600μm.
The other parameters are the same as those in Figure 4.13.

Length l_c = 700 (μm)
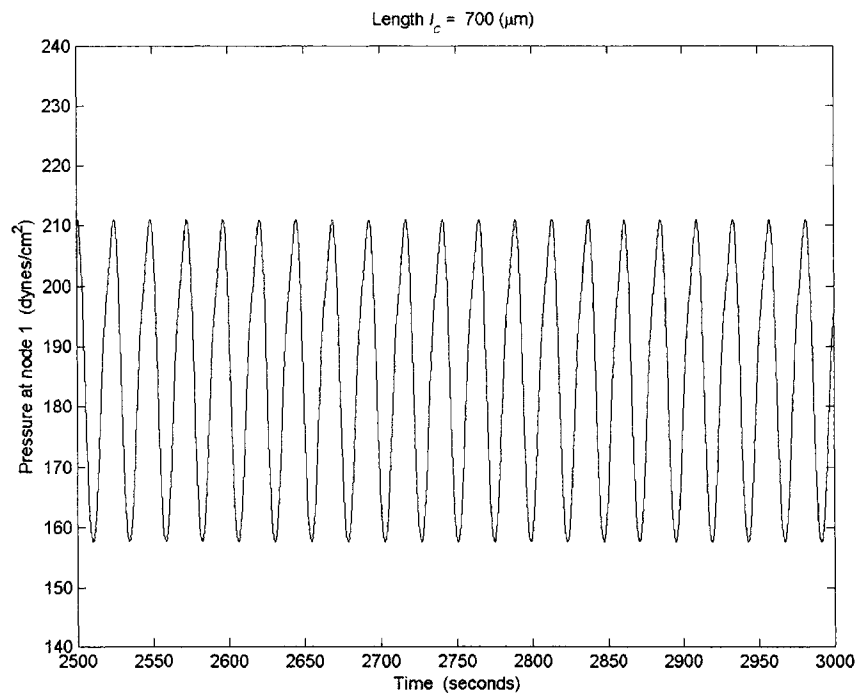
Figure 4.14d   Time series Showing Unstable Pressure at Node 1 when l_C = 700μm. The other parameters are the same as those in Figure 4.13.

78

Length l_c = 800 (μm)
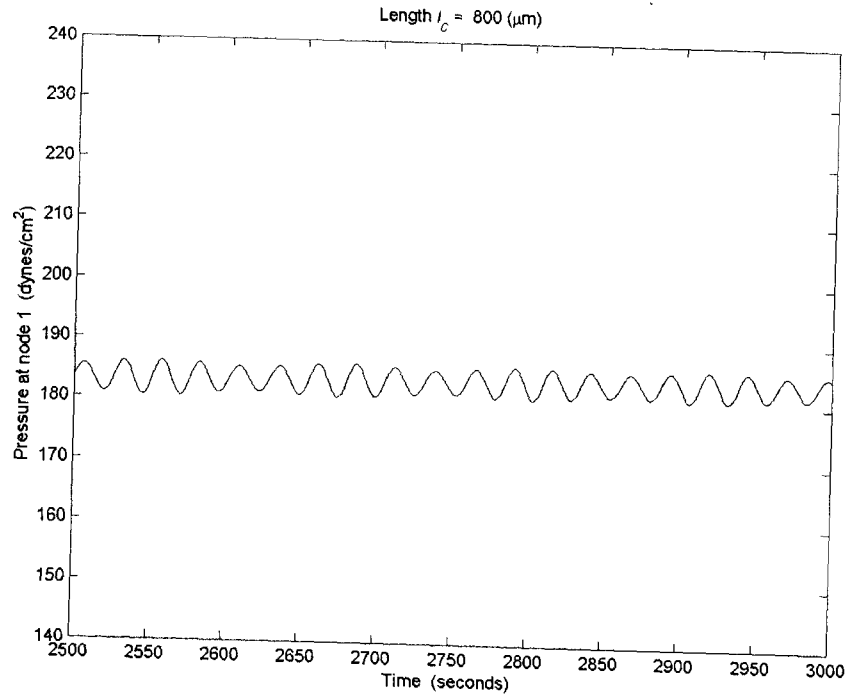
Figure 4.14e Time series Showing Slightly Unstable Pressure at Node 1 when
$l_C = 800\mu$m. The other parameters are the same as those in Figure 4.13.

Length l_c = 900 (μm)
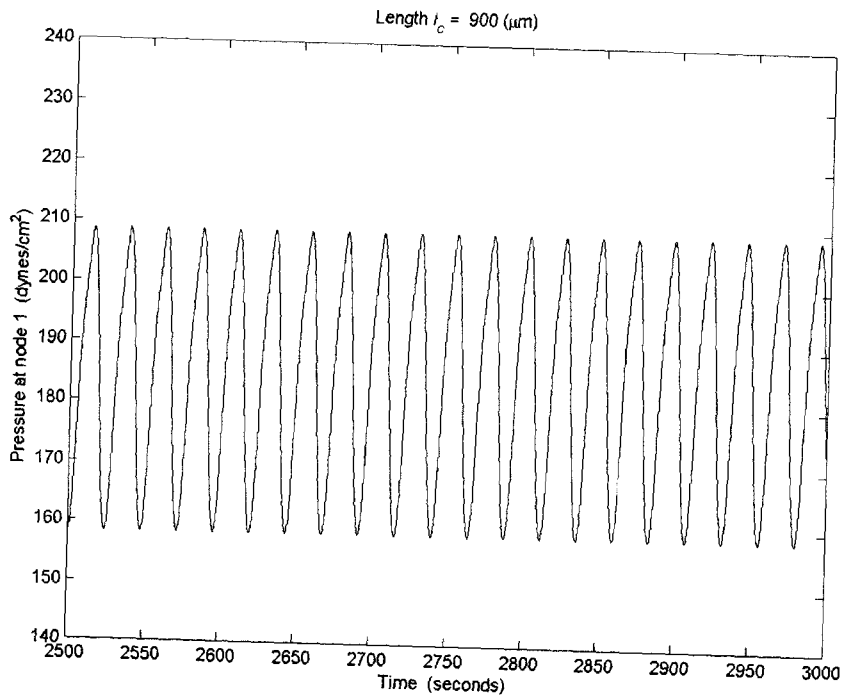
Figure 4.14f Time series Showing Unstable Pressure at Node 1 when $l_C =$
900μm. The other parameters are the same as those in Figure 4.13.

79

Length l_c = 1000 (μm)
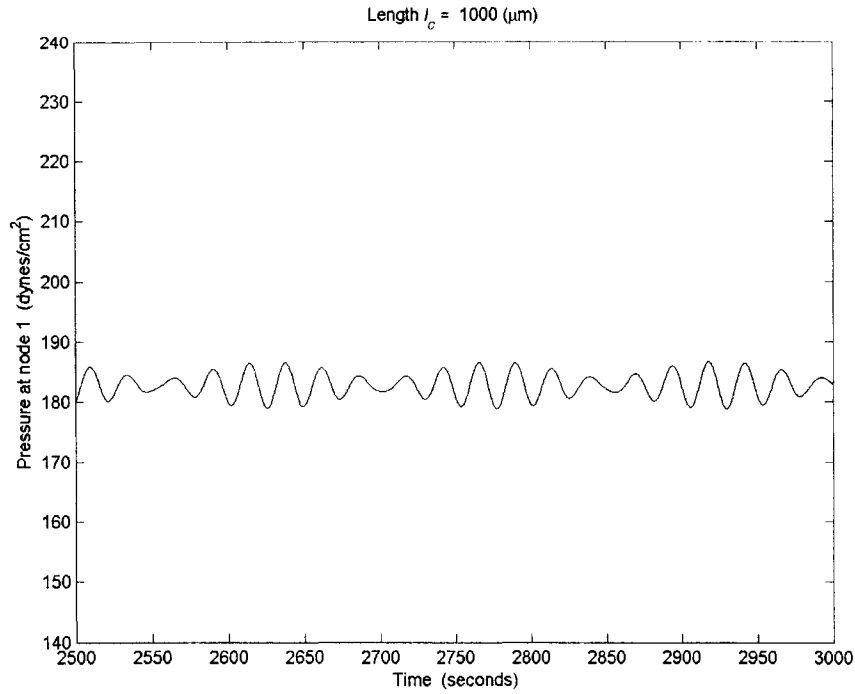
Figure 4.14g Time series Showing Slightly Unstable Pressure at Node 1 when l_C = 1000μm. The other parameters are the same as those in Figure 4.13.

4.5 Instability Regions of the Three Node Network

As shown in Section 3.6, an instability region on a $p - H$ plane is found to be quite narrow for the two node system. Both tight tolerances and high inlet hematocrit values suggest that it is impractical to build such an in vitro model for experimental verification

Following the approach in Section 3.6, the instability region is constructed on the $p - H$ plane for the three node system in Figure 4.15. Here, p denotes the logit plasma skimming parameters, $p = p_1 = p_2$; H represents the inlet hematocrits, $H = H_1 = H_2$. Other physical parameters are $Q_1 = Q_2 = 10$nl/min, $d_A = d_B = 35\mu$m, $d_C = 50\mu$m, $l_A = l_B = 500\mu$m, $l_C = 1000\mu$m. Pries's in vitro viscosity model and the logit plasma skimming parameters are applied.

80

Figure 4.15 displays the much broader instability range on the $p - H$ plane for the three node system than that for the two node system. Also, compared to the two node system, inlet hematocrits H_1, H_2 required for instability decrease. For example, the minimum inlet hematocrits are about 0.76 at $p_1 = p_2 = 2.0$ for the three node system as shown in Figure 4.15 while the minimum inlet hematocrit is about 0.8 at p =2.0 for the two node system as shown in Figure 3.13.
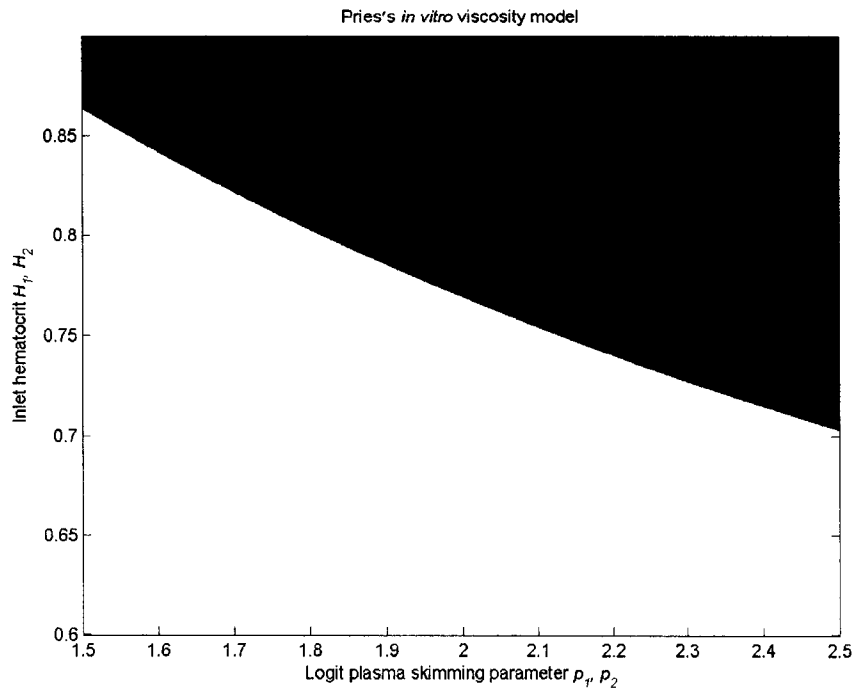
Figure 4.15 An Instability Region in the p - H Plane with the Logit Plasma Skimming Model. The other parameters are: Pries's *in vitro* viscosity model, Q_1 = Q_2 = 10nl/min, $d_A = d_B = 35\mu$m, $d_C = 50\mu$m, $l_A = l_B = l_C = 500\mu$m.

For the two node system, when the linear plasma skimming model is applied, the necessary conditions are not satisfied, and thus no instability region can be found (see Section 3.7). However, from Section 4.1, it is found the linear model can also lead to spontaneous oscillations in the three node system, which means the three node system is more robust than the two node system.

81

Again, when the linear plasma skimming model is applied, the program containing DDE-BIFTOOL subroutines are carried out to generate the instability region in the $p - H$ plane in Figure 4.16. Interestingly, the instability region shown in Figure 4.16 is slightly larger than the one show in Figure 4.15 with lower minimum inlet hematocrits. It is suggested that even though the plasma skimming model lost the nonlinearity, additional nonlinear behaviors are introduced by combining the plasma skimming model and the topological complexity of the three node system. This also means that the necessary conditions Eq.(3.7.1) for the two node system is unsuitable for the three node system.

Pries's *in vitro* viscosity model

Inlet hematocrit H_1, H_2

Linear plasma skimming parameter p_1, p_2
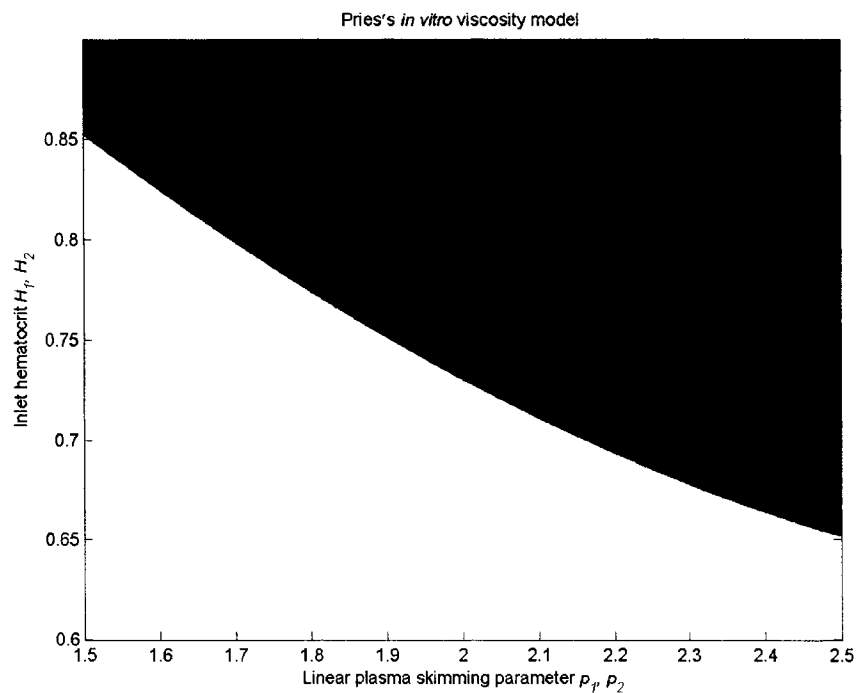
Figure 4.16 An Instability Region in the $p - H$ Plane with the Linear Plasma Skimming Model. The other parameters are the same as those in Figure 4.15.

Under certain conditions, several separated instability regions appear in the $p - H$ plane. For instance, when l_C is changed to $1000\mu m$ but other parameters remain constant, three instability regions are shown in Figure 4.17. Region I has been

82

verified as unstable by the simulation program, but the other two regions have not been verified. It is found Region II corresponds to positive real rightmost eigenvalues. For example, at $p_1 = p_2 = 1.5$, $H_1 = H_2 = 0.55$, a profile of the characteristic roots is shown in Figure 4.18a. Region III corresponds to complex rightmost eigenvalues with positive real parts, but the real parts are slightly greater than zero. For example, at $p_1 = p_2 = 2.0$, $H_1 = H_2 = 0.55$, the profile of the characteristic roots is shown in Figure 4.18b. In future numerical investigations, a promising direction is to adjust physical parameters to find the lower regions corresponding to complex rightmost eigenvalues with considerably positive real parts, which may be verified by the simulation program.
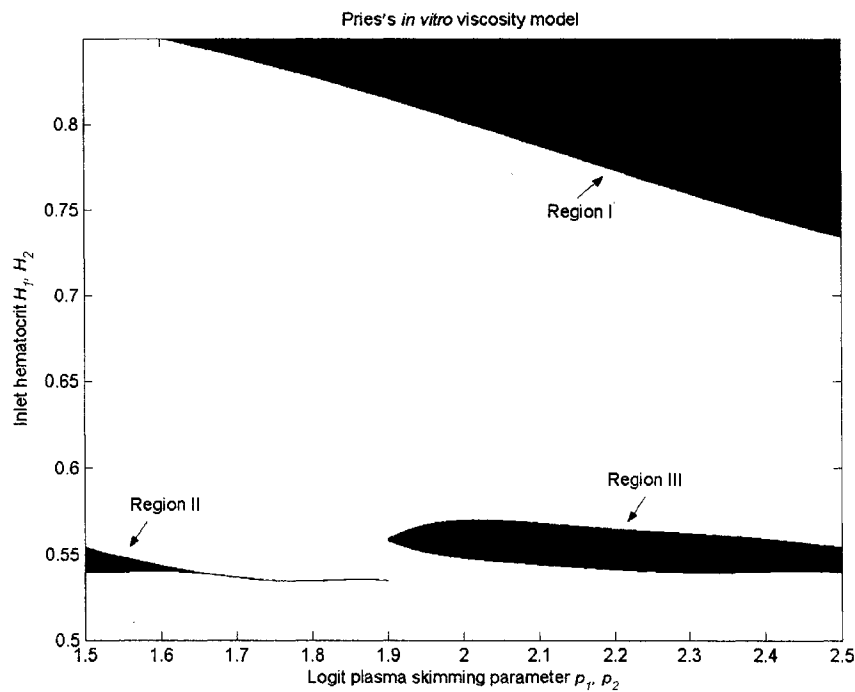
Figure 4.17 Multiple Instability Regions in the $p - H$ Plane.
The logit plasma skimming model, Pries's *in vitro* viscosity model, $Q_1 = Q_2 = 10$nl/min, $d_A = d_B = 35\mu$m, $d_C = 50\mu$m, $l_A = l_B = 500\mu$m, $l_C = 1000\mu$m.

83
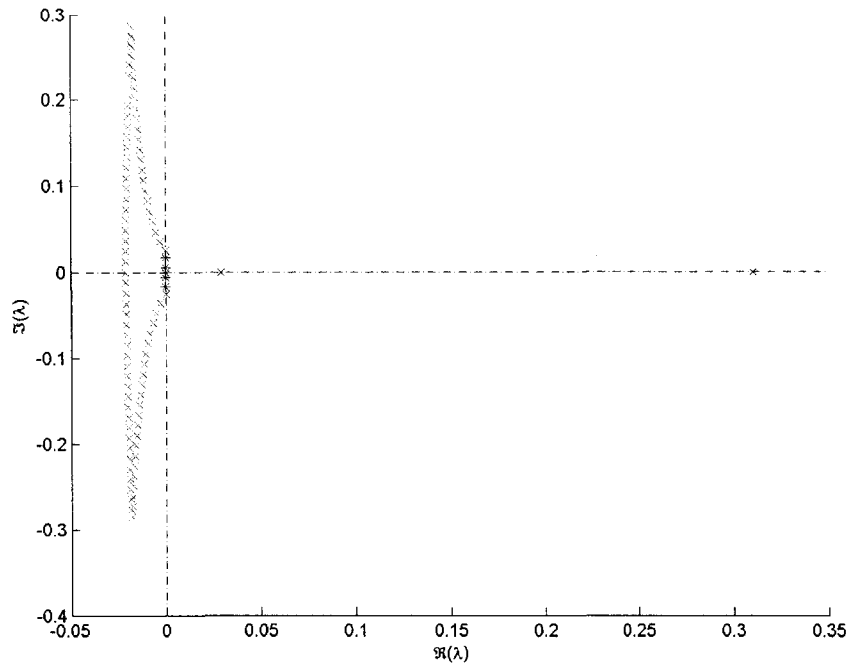
Figure 4.18a   A Profile of Characteristic Roots of a Point in Region II at $p_1 = p_2 = 1.5$, $H_1 = H_2 = 0.55$. The other parameters are the same as those in Figure 4.17.
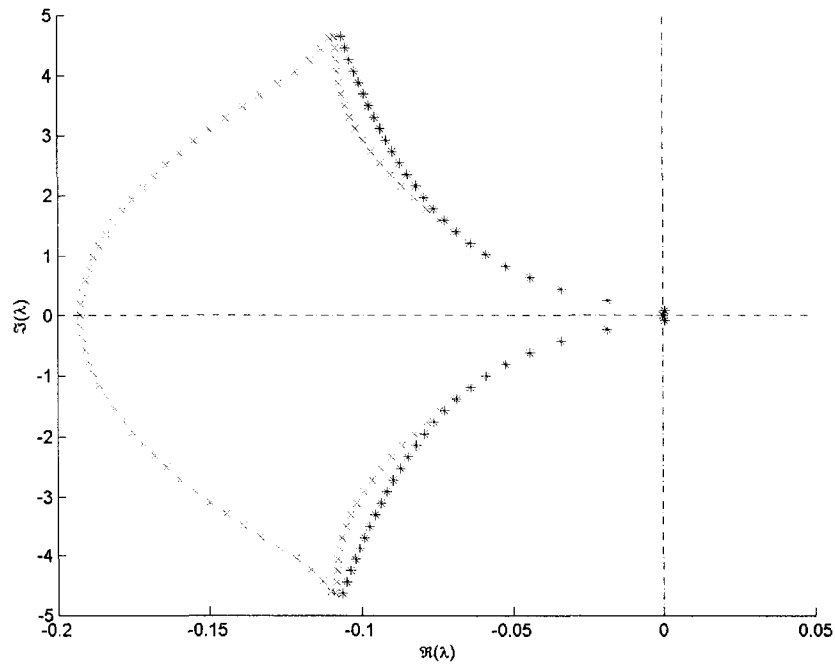
Figure 4.18b   A Profile of Characteristic Roots of a Point in Region III at $p_1 = p_2 = 2.0$, $H_1 = H_2 = 0.55$. The other parameters are the same as those on Figure 4.17.

84

4.6 Effects of Heterogeneity of Inlet Conditions

Proceeding investigations in the two node system exhibit impacts of geometric parameters like diameters or lengths. However, the three node system has two inlet branches that allow the inlet hematocrits and volumetric flow rates to be different. It is of interest to know effects of heterogeneity of inlet conditions on the hemodynamics.

To observe the effects of heterogeneity of inlet conditions better, the investigation is performed for the three node system with symmetrical geometric parameters, for example, the three node system with the logit plasma skimming parameters $p_1 = p_2 = 2.0$, diameters $d_A = d_B = 35\mu m$, $d_C = 50\mu m$, lengths $l_A = l_B = 500\mu m$, $l_C = 1000\mu m$.

The hematocrits in inlet 1 and inlet 2 are denoted as H_1 and H_2 respectively; accordingly, the flow rates are denoted as Q_1 and Q_2 respectively. From the governing DDE of Eq.(2.6.11), it is found that the two inlet flow rates always appear as a ratio of one to the other, i.e., $y_q = Q_2/Q_1$, thus instead of the flow rates, the changing ratio is studied here. Since some information of the inlet hematocrits is contained in the viscosity correlations, in the following numerical studies, the H_1 is kept a constant value, while the H_2 is varied.

In Figure 4.19 and Figure 4.20, the steady state flow ratio $Q^* = Q_A/Q_1$ is potted against the varying y_q and H_2 respectively with other physical parameters fixed. Due to the symmetry of the system, y_q ranges from 1 to 10 instead of from 0.1 from 10. Again, in these figures, a black point denotes a stable steady state, a grey point denotes unstable one, and a black point with a smaller size denotes uncertainty due to the functional limitation of DDE-BIFTOOL.

85
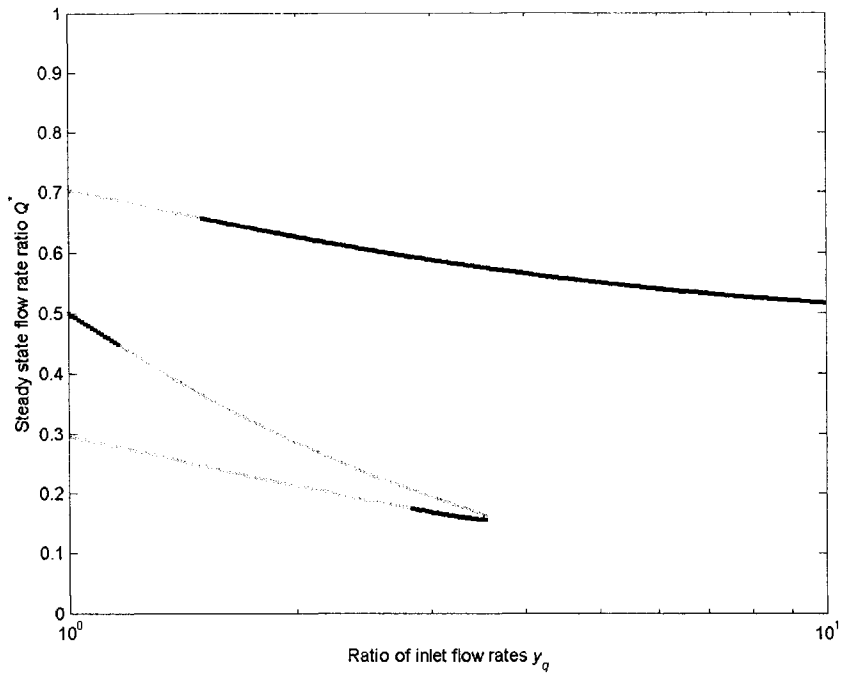
Figure 4.19 Stability of Steady States versus Varying Ratio of Inlet Flow Rates
$y_q = Q_2/Q_1$. The other parameters are: $H_1 = H_2 = 0.8$, Logit plasma skimming parameters $p_1 = p_2 = 2.0$, $d_A = d_B = 35\mu m$, $d_C = 50\mu m$, $l_A = l_B = 500\mu m$, $l_C = 1000\mu m$.

From Figure 4.19, it is noticed that when $y_q = 1$, i.e., $Q_1 = Q_2$, the system has three steady state flow ratios: one is equal to 1 and the others are exchangeable due to symmetry of the system. Then the increasing y_q destroys the symmetry, but there are still three steady states existing until y_q grows to a critical value about 3.5. When y_q is greater than about 3.5, the lower two branches of steady states disappear, and only one steady state remains. Meanwhile, the stability of steady states also changes with varying y_q. At the beginning, the middle steady state is stable, and the other two are unstable. Then the middle one turns to be unstable, and when y_q keeps increasing, the upper branch of steady states becomes stable. The lower branch is unstable but it switches to be stable when the ratio gets close to about 2.5.

86
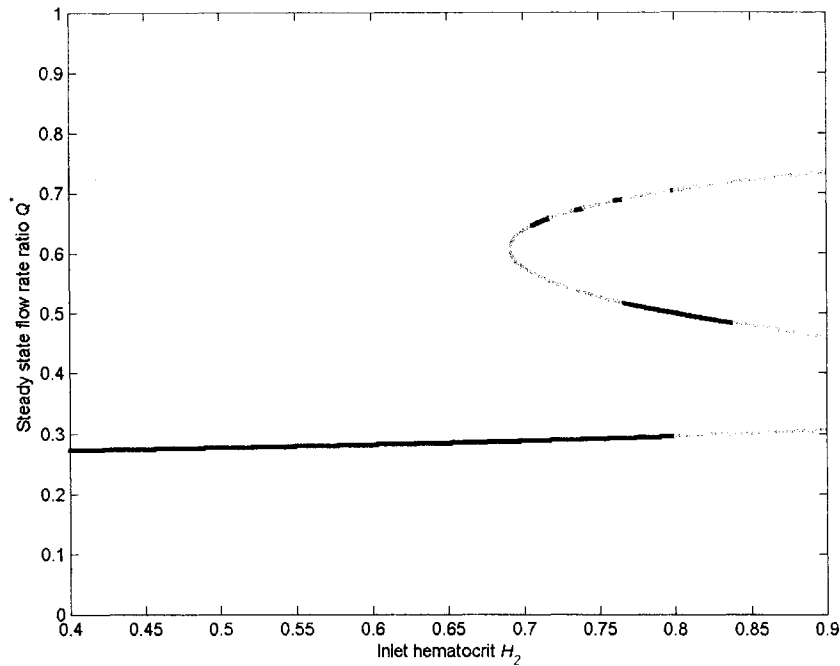
Figure 4.20 Stability Of Steady States versus Varying Hematocrit H_2.
The other parameters are: $H_1 = 0.8$, $Q_1 = Q_2$, Logit plasma skimming parameter $p_1 = p_2 = 2.0$, $d_A = d_B = 35\mu m$, $d_C = 50\mu m$, $l_A = l_B = 500\mu m$, $l_C = 1000\mu m$.

Figure 4.20 shows relatively complex changes of stability around steady states versus increasing inlet hematocrit H_2 as well. At first, one stable branch of steady states exists for the system. When the value of H_2 increases to about 0.68, two new branches emerge as unstable ones in the upper part of the graph. The middle branch turns to be stable first at $H_2 \approx 0.76$ and unstable again at $H_2 \approx 0.83$. The upper branch is mostly unstable but stable in a few discrete segments. The lower branch becomes unstable at $H_2 \approx 0.8$.

All the above numerical results indicate that the effects of heterogeneity of the conditions are complex. When one inlet condition changes, not only the number of steady states may change, but also the stability around steady states may change multiple times. Therefore, to facilitate the numerical studies on the three node system, the irregularity of inlet conditions will not considered, and the flow rates and hematocrits in two inlet branches can be set to be exactly equal.

87

CHAPTER V

CONCLUSIONS AND FUTURE WORK

By performing the stability analysis around steady states, it is found that spontaneous oscillations can occur in the simple microvascular networks with either the two node topology or the three node topology (two inlets). Fåhraeus effect and plasma skimming phenomena are considered in the mathematical modeling.

It is found that the dynamic behavior of the two node system is sensitive to physical parameters such as plasma skimming parameters, inlet hematocrits, inlet blood flow rates, diameters and lengths of branches, etc. The instability regions can be found when the logit plasma skimming model is applied. When the linear plasma skimming model is used instead, the necessary conditions for oscillations are not satisfied, and the system is stable around steady states always. The obtained instability regions are quite narrow in the $p - H$ plane, and the inlet hematocrits are quite high (about 0.8 when $p = 2.0$). These strict physical conditions make experimental verification of this phenomenon very difficult in a two node network.

Numerical results for the three node system are more promising than those for the two node system. The three node system has instabilities over much wider parameter ranges than the two node system with lower inlet hematocrits. Besides, the three node system is more robust for plasma skimming models than the two node system, and when either the logit model or the linear one is applied, the three node system can exhibit instability over certain parameter ranges.

88

Some interesting dynamic behaviors like multiple frequency oscillations and non-oscillation windows are found in the three node system, which are absent in the two node system. These changes may be as a result of the increasing topological complexity of the three node network. Unfortunately, the inlet hematocrits are still quite high (about 0.76 when using the logit plasma skimming model with p = 2.0; about 0.74 when using the linear plasma skimming model with p = 2.0), and experimental verification under the inlet conditions are still too difficult to be carried out.

To conclude, the stability analysis approach presented in this thesis is reasonable and feasible, and stability predictions produced by the approach can mostly be verified by the direct simulation program (Carr and LeCoin, 2000)[1]. Since the stability analysis is based on the linearization around steady states, and higher order terms are neglected during the process, the theoretical prediction may not be accurate in some cases. For example, when the real parts of rightmost characteristic roots are close to zero, deviations exist between the results of the stability analysis and the direct simulation. Although the linear stability analysis shows slight deviation from the direct numerical simulation in a few cases, the approach does provide meaningful directions toward finding instability regions for the future experimental verifications.

There are some directions for the future work: continuing the search in wider parameter ranges for the symmetric three node system; examining the three node systems with asymmetric structures; moving to new topologies, for instance, three node networks with one inlet and two outlets, four node networks, etc; building simple microvascular networks using soft lithography approach, and conducting *in vitro* experiments when realizable conditions are discovered.

REFERENCES

1. M. F. Kiani, A. R. Pries, L. L. Hsu, I. H. Sarelius, and G. R. Cokelet, Fluctuations in microvascular blood flow parameters caused by hemodynamic mechanisms. *Am. J. Physiol*, 266, pp. H1822-1828 (1994)

2. R. T. Carr and M. LeCoin, Nonlinear dynamics of microvascular blood flow. *Ann. Biomed. Eng.*, 28, pp. 641-652 (2000)

3. R. E. McCall and C. M. Tankersley, *Phelebotomy Essentials*. Philedelphia, Lippincott Williams & Wilkins, Third Edition, pp.184~188 (2002)

4. Glenn Elert, *The Physics Fact Book*™ (Online): Available from http://hypertextbook.com/facts/2004/MichaelShmukler.shtml .

5. H. L. Goldsmith, G. R. Cokelet, and P. Gaehtgens, R. Fåhraeus: evolution of his concepts in cardiovascular physiology. *Am. J. Physiol.*, 257, pp. H1005-1015 (1989)

6. Y. C. Fung, Blood flow in the capillary bed. *J. Biomechanics*, 2, pp. 353-372 (1969)

7. H. S. Lew and Y. C. Fung, Entry flow into blood vessels at arbitrary Reynolds number. *J. Biomechanics*, 3, pp. 23-38 (1970)

8. H. L. Goldsmith, Red cell motions and wall interactions in tube flow. *Federation Proceedings*, 30, 5, pp. 1578-1588 (1971)

9. R. T. Carr, Estimation of hematocrit profile symmetry recovery length downstream from a bifurcation. *Biorheology*, 26, pp. 907-920 (1989)

10. R. Fåhraeus, The suspension stability of the blood. *Physiol. Rev.*, Vol. 9, pp. 241-274 (1929)

11. R. Fåhraeus and T. Lindqvist, The viscosity of blood in narrow capillary tubes. *Am. J. Physiol.*, 96, pp. 562-568 (1931)

12. M. F. Kiani and A. G. Hudetz, A semi-empirical model of apparent blood viscosity as a function of vessel diameter and discharge hematocrit. *Biorheology*, 28, pp. 65-73 (1991)

13. A.R. Pries, D. Neuhaus and P. Gaehtgens, Blood viscosity in tube flow: dependence on diameter and hematocrit. *Am. J. Physiol.*, 263, pp. H1770-1778 (1992)

14. A. R. Pries, T. W. Secomb, T. Gessner, M. B. Sperandio, J. F. Gross and P. Gaehtgens, Resistance to blood flow in microvessels *in vivo*. *Circ. Res.*, 75, pp. 904-915 (1994)

15. R. B. Bird, W. E. Stewart, and E. N. Lightfoot, *Transport Phenomena*. New York, John Wiley & Sons, Second Edition, pp. 51 (2002)

16. A. Krogh, *The anatomy and physiology of capillaries*. New Haven, Yale University Press (1929)

17. G. R. Cokelet, Blood flow through arterial microvascular bifurcations. In *Microvascular Networks: Experimental and theoretical studies*, Basel [Switzerland] ; New York, Karger, pp. 155-167 (1986)

18. R. T. Carr, Plasma skimming in replicas of microvascular bifurcations. *Ph.D. Dissertation*, University of Rochester, Rochester, NY (1984)

19. A. R. Pries, K. Ley, M. Claassen, P. Gaehtgens, Red cell distribution at microvascular bifurcations. *Microvasc. Res.*, 38, pp. 81-101 (1989)

20. B. M. Fenton, D. W. Wilson and G. R. Cokelet, Analysis of the effects of measured white cell entrance times on hemodynamics in a computer model of microvascular bed. *Pflueg. Arch.*, 403, pp. 396-401 (1985)

21. J. W. Dellimore, M. J. Dunlop, P. B. Canham, Ratio of cells and plasma in blood flowing past branches in small plastic channels. *Am. J. Physiol.*, 244, pp. H635-642 (1983)

22. H. Wayland and P. C. Johnson, Erythrocyte velocity measurement in microvessels by a two slit photometric method. *J. Appl. Physiol.*, 22, pp. 333-337 (1967)

23. G. P. Rodgers, A. N. Schechter, C. T. Noguchi, H. G. Klein, A. W. Nienhuis, and R. F. Bonner, Periodic microcirculatory flow in patients with sickle-cell disease. *New Eng. J. Med.*, 311, pp. 1534-1538 (1984)

24. C. A. Wiederhelm et al., Pulsatile pressures in the microcirculation of frog mesentery, Am. J. Physiol., 207, pp. 173-176 (1964)

25. C. A. Giller and M. Mueller, Linearity and non-linearity in cerebral hemodynamics. *Medical Engineering & Physics*, 25, pp. 633-646 (2003)

26. P. C. Johnson and H. Wayland, Regulation of blood flow in single capillaries. *Am. J. Physiol.*, 212, pp. 1405-1415 (1967)

27. M. Intaglietta, R. F. Pawula and W. R. Tompkins, Pressure measurements in the mammalian microvasculature. *Microvas. Res.*, 2, pp. 212-220 (1969)

28. B. W. Zweifach, Quantitative studies of microcirculatory structure and function I: Analysis of pressure distribution in the terminal vascular bed in cat mesentery. *Circ. Res.*, 34, pp. 843-857 (1974)

29. D. W. Slaaf, R. S. Reneman, C. A. Wiederhielm, Pressure regulation in muscle of unanesthetized bats. *Microvas. Res.*, 33, pp. 315-326 (1987)

30. A. Colantuoni, S. Bertuglia, and M. Intaglietta, Quantitation of rhythmic diameter changes in arterial microcirculation. *Am. J. Physiol.*, 246, pp. H508-517 (1984)

31. D. W. Slaaf, G. J. Tangelder, H. C. Teirlinck, and R. S. Reneman, Arteriolar vasomotion and arterial pressure reduction in rabbit tenuissimus muscle. *Microvas. Res.*, 33, pp. 71-80 (1987)

32. D. Parthimos, D. H. Edwards, and T. M. Griffith, Comparison of chaotic sinusoidal vasomotion in the regulation of microvascular flow. *Cardiovas. Res.*, 31, pp. 388-399 (1996)

33. A. Hessellund, P. Jeppesen, C. Aalkjaer and T. Bek, Characterization of vasomotion in porcine retinal arterioles. *Acta Ophthalmol. Scand.*, 81, pp. 278-282 (2003)

34. J. U. Meyer, L. Lindbom, and M. Intaglietta, Coordinated diameter oscillations at arteriolar bifurcations in skeletal muscle. *Am. J. Physiol.*, 253, pp. H568-573 (1987)

35. D. Parthimos, K. Osterloh, A. R. Pries and T. M. Griffith, Deterministic nonlinear characteristics of *in vivo* blood flow velocity and arteriolar diameter fluctuations. *Physics in Medicine and biology*, 49, pp. 1789-1802 (2004)

36. R. Letienne, C. Julien, Z. Zhang, and C. Barres, Characterization of a major slow oscillation in the mesenteric circulation of conscious rats. *Clin. Exp. Pharmacol. and Physiol.*, 25, pp. 820-824 (1998)

37. F. C. Moon, *Chaotic and Fractal Dynamics: An introduction for applied scientists and engineers*. New York, Wiley (1992)

38. S. H. Strogatz, *Nonlinear dynamics and chaos*. Cambridge, Westview (2000)

39. Y. C. Fung, Stochastic flow in capillary blood vessels. *Microvas. Res.*, 5, pp. 34-48 (1973)

40. A. R. Pries, K. Ley, and P. Gaehtgens, Generalization of the Fahraeus principle for microvessel networks. *Am. J. Physiol.*, 251, pp. H1324-H1332 (1986)

41. A. R. Pries, T. W. Secomb, and P. Gaehtgens, Stucture and hemodynamics of microvascular networks: heterogeneity and correlations. *Am. J. Physiol.*, 269, H1713-1722 (1995)

42. A. R. Pries, T. W. Secomb, and P. Gaehtgens, Relationship between structural and hemodynamics heterogeneity in microvascular networks. *Am. J. Physiol.*, 270, H545-553 (1996)

43. D. C. Duffy, J. C. McDonald, O. J. A. Schueller, and G. M. Whitesides, Rapid prototyping of microfluidic systems in poly(dimethylsiloxane). *Analyst Chem*, 70, pp. 4974-4984 (1998)

44. Y. Xia and G. M. Whitesides, Soft lithography. *Angew Chem Int Ed*, 37, pp. 550-575 (1998)

45. M. Clarner, Fabrication of optically functional micro sensors by sol-gel soft lithography. *Master Thesis*, University of New Hampshire, Durham, NH (2000)

46. F. Wu, R. T. Carr, J. B. Geddes, and Y. Lao, Stability analysis of blood flow in microvascular networks. *Experimental Biology 2005/XXXV* (Abstract), San Deigo (2005)

47. F. Wu, R. T. Carr, J. B. Geddes, and Y. Lao, Stability analysis of blood flow in three node microvascular networks. *Microcirculation 2005* (Abstract), Durham (2005)

48. R. T. Carr, J. B. Geddes, and F. Wu, Oscillation in a simple microvascular network. *Ann. Biomed. Eng.*, 33, pp. 764-771 (2005)

49. J. B Geddes, G. Withington, R. T Carr, and F. Wu, Oscillations in microvascular blood flow. *Dynamics Days Arizona* (Abstract) (2003)

50. L. Class and M. C. Mackey, *From clocks to chaos*. Chichester, Princeton University Press, pp. 192 (1988)

51. E. Kreyszig, *Advanced Engineering Mathematics*. New York, John Wiley & Sons, seventh edition, pp. 472-474 (1993)

52. J. K. Hale and S. M. V. Lunel, Introduction to functional differential equations. *Applied Mathematical Sciences*, 99, New York, Springer-Verlag, pp. 38-39 (1993)

53. T. Luzyanina, K. Engelborghs, and D. Roose, Numerical bifurcation analysis of differential equations with state-dependent delay. *International Journal of Bifurcation and Chaos*, 11, 3, pp. 737-753 (2001)

54. E. Kreyszig, *Advanced engineering mathematics*. New York, seventh Edition, John Wiley & Sons, pp. 802-807 (1993)

55. J. K. Hale, Theory of functional differential equations. *Applied Mathematical Sciences*, 3, New York, Springer-Verlag (1977)

56. K. Engelborghs, T. Luzyanina, and G. Samaey, DDE-BIFTOOL v. 2.00: a Matlab package for bifurcation analysis of delay differential equations. *Report TW 330,* Department of Computer Science, K. U. Leuven, Leuven, Belgium (2001): Available from www.cs.kulenven.ac.be/~koen/delay/ddebiftool.shtml

57. K. Engelborghs, T. Luzyanina, and D. Roose, Numerical bifurcation analysis of delay differential equations using DDE-BIFTOOL. *ACM Transactions on Mathematical Software*, 28, 1, pp. 1-21 (2002)

58. R. G. Rice and D. D. Do, *Applied mathematics and modeling for chemical engineers*. New York, John Wiley & Sons, pp. 632-635 (1994)

59. Y. Xia, J. McClelland, R. Gupta, D. Qin, X. Zhao, L. Sohn, R. J. Cellotta, and G. M. Whitesides, Replica molding using polymeric materials: A practical step toward nanomanufacturing. *Adv. Mater.*, 9, pp.147-149 (1997)

60. P. Grassberger and I. Procaccia, Measuring the strangeness of strange attractors. *Physica D.*, 9, pp. 189-208 (1983)

APPENDICES

APPENDIX A. DEFINITIONS OF RHS FUNCTIONS AND THEIR FIRST ORDER DERIVATIVES OF GOVERNING DDE'S

Details of the specification required by DDE-BIFTOOL are available from the user manual – Report TW 330 (Engelborghs *et al.*, 2001)[50]. Definitions of right hand sides (RHS) functions and their first order derivatives of governing DDE's are given as follows.

● **The two node network**

First, we treat the delays as state-dependent ones. Let x_l denote Q, τ_l denote τ_A, τ_2 denote τ_B, the following equations are obtained from (2.4.16) and (2.4.10),

$$
\begin{aligned}
\frac{dx_1(t)}{dt} = &-\frac{d_B^4}{l_B d_A^6}\frac{4Q_1 H_1}{\pi}\frac{\beta_A(\bar{H}_A(t))}{\mu_B(\bar{H}_B(t))}x_1^3(t)[\frac{F(x_1(t))}{x_1(t)} - \frac{F(x_1(t-\tau_1(t)))}{x_1(t-\tau_1(t))}] \\
&+\frac{1}{l_B d_B^2}\frac{4Q_{in}H_{in}}{\pi}\frac{\beta_B(\bar{H}_B(t))}{\mu_B(\bar{H}_B(t))}x_1(t)(1-x_1(t))^2 \\
&\times[\frac{1-F(x_1(t))}{1-x_1(t)} - \frac{1-F(x_1(t-\tau_2(t)))}{1-x_1(t-\tau_2(t))}]
\end{aligned}
$$
(A.1)

$$
\int_{t-\tau_1(t)}^{t} k_1 x_1(t)ds = 1
$$
(A.2)

$$
\int_{t-\tau_2(t)}^{t} k_2[1-x_1(t)]ds = 1,
$$
(A.3)

where $k_1 = 4Q_1/(\pi d_A^2 l_A)$, $k_2 = 4Q_1/(\pi d_B^2 l_B)$.

By differentiating the threshold conditions, and let $x_2(t) = \tau_1(t)$, $x_3(t) = \tau_2(t)$, Eq.(A.2) and Eq.(A.3) are transformed into Eq.(A.4) and Eq.(A.5) respectively.

$$
\frac{dx_2(t)}{dt} = 1 - \frac{x_1(t)}{x_1(t-\tau_1(t))}
$$
(A.4)

$$
\frac{dx_3(t)}{dt} = 1 - \frac{1-x_1(t)}{1-x_1(t-\tau_2(t))}.
$$
(A.5)

Let $x_4(t) = \bar{H}_A(t), x_5(t) = \bar{H}_B(t)$, (2.4.9) combined with (2.4.15) are rewritten as

$$
\frac{dx_4(t)}{dt} = k_1 H_1 x_1(t)[\frac{F(x_1(t))}{x_1(t)} - \frac{F(x_1(t-\tau_1(t)))}{x_1(t-\tau_1(t))}]
$$
(A.6)

$$
\frac{dx_5(t)}{dt} = k_2 H_1(1-x_1(t))[\frac{1-F(x_1(t))}{1-x_1(t)} - \frac{1-F(x_1(t-\tau_2(t)))}{1-x_1(t-\tau_2(t))}]
$$
(A.7)

The definitions of the two node network are given by Eq.(A.1) and Eq.(A.4-7). To conclude, the above system has five state variables $(x_1, x_2, x_3, x_4, x_5)$, two state-dependent delays (τ_1, τ_2), and six parameters $(p, H_1, d_A, d_B, k_1, k_2)$.

Note RHS of Eq.(A.1) and Eq.(A.4-7) as $f(1,1), f(2,1) f(3,1), f(4,1), f(5,1)$ in order. The first order derivatives of the RHS function $f(i,1)$ with respect to state variables are listed as follows , where $J_{i,j} = \partial f(i,1) / \partial x_j$.

1) With respect to $x(t)$,

$$J_{1,1} = -(\frac{d_B}{d_A})^6 k_2 H_1 \frac{\beta_A(x_4(t))}{\mu_B(x_5(t))} \{3x_1^2(t)[\frac{F(x_1(t))}{x_1(t)} - \frac{F(x_1(t-\tau_1(t)))}{x_1(t-\tau_1(t))}]$$

$$+ x_1^2(t)[\frac{dF(x_1(t))}{dx_1(t)} - \frac{F(x_1(t))}{x_1(t)}]\} \tag{A.8}$$

$$+ k_2 H_1 \frac{\beta_B(x_5(t))}{\mu_B(x_5(t))} \{(1-x_1(t))(1-3x_1(t))[\frac{1-F(x_1(t))}{1-x_1(t)} - \frac{1-F(x_1(t-\tau_2(t)))}{1-x_1(t-\tau_2(t))}]$$

$$+ x_1(t)(1-x_1(t))[\frac{1-F(x_1(t))}{1-x_1(t)} - \frac{dF(x_1(t))}{dx_1(t)}]\}$$

$$J_{1,4} = -(\frac{d_B}{d_A})^6 k_2 H_1 \frac{d\beta_A(x_4(t))/dx_4(t)}{\mu_B(x_5(t))} x_1^3(t)[\frac{F(x_1(t))}{x_1(t)} - \frac{F(x_1(t-\tau_1(t)))}{x_1(t-\tau_1(t))}] \tag{A.9}$$

$$J_{1,5} = (\frac{d_B}{d_A})^6 k_2 H_1 \frac{\beta_A(x_4(t))\beta_B(x_5(t))}{\mu_B^2(x_5(t))} x_1^3(t)[\frac{F(x_1(t))}{x_1(t)} - \frac{F(x_1(t-\tau_1(t)))}{x_1(t-\tau_1(t))}]$$

$$+ k_2 H_1 [\frac{d\beta_B(x_5(t))/dx_5(t)}{\mu_B(x_5(t))} - \frac{\beta_B^2(x_5(t))}{\mu_B^2(x_5(t))}] x_1(t)(1-x_1(t))^2 \tag{A.10}$$

$$[\frac{1-F(x_1(t))}{1-x_1(t)} - \frac{1-F(x_1(t-\tau_2(t)))}{1-x_1(t-\tau_2(t))}]$$

$$J_{2,1} = -\frac{1}{x_1(t-\tau_1(t))} \tag{A.11}$$

$$J_{3,1} = \frac{1}{1-x_1(t-\tau_2(t))} \tag{A.12}$$

$$J_{4,1} = k_1 H_1 [\frac{dF(x_1(t))}{dx_1(t)} - \frac{F(x_1(t-\tau_1(t)))}{x_1(t-\tau_1(t))}] \tag{A.13}$$

97

$$J_{5,1} = k_2 H_1 [\frac{1 - F(x_1(t - \tau_2(t)))}{1 - x_1(t - \tau_2(t))} - \frac{dF(x_1(t))}{dx_1(t)}] \ . \tag{A.14}$$

2) With respect to $x(t - \tau_1(t))$

$$J_{1,1} = (\frac{d_B}{d_A})^6 k_2 H_1 \frac{\beta_A(x_4(t))}{\mu_B(x_5(t))} \frac{x_1^3(t)}{x_1(t - \tau_1(t))} [\frac{dF(x_1(t - \tau_1(t)))}{dx_1(t - \tau_1(t))} - \frac{F(x_1(t - \tau_1(t)))}{x_1(t - \tau_1(t))}] \tag{A.15}$$

$$J_{2,1} = \frac{x_1(t)}{x_1^2(t - \tau_1(t))} \tag{A.16}$$

$$J_{4,1} = k_1 H_1 \frac{x_1(t)}{x_1(t - \tau_1(t))} [\frac{F(x_1(t - \tau_1(t)))}{x_1(t - \tau_1(t))} - \frac{dF(x_1(t - \tau_1(t)))}{dx_1(t - \tau_1(t))}]. \tag{A.17}$$

3) With respect to $x(t - \tau_2(t))$

$$J_{1,1} = k_2 H_1 \frac{\beta_B(x_5(t))}{\mu_B(x_5(t))} \frac{x_1(t)(1 - x_1(t))^2}{1 - x_1(t - \tau_2(t))} [\frac{dF(x_1(t - \tau_2(t)))}{dx_1(t - \tau_2(t))} - \frac{1 - F(x_1(t - \tau_2(t)))}{1 - x_1(t - \tau_2(t))}] \tag{A.18}$$

$$J_{3,1} = - \frac{1 - x_1(t)}{(1 - x_1(t - \tau_2(t)))^2} \tag{A.19}$$

$$J_{5,1} = k_2 H_1 \frac{1 - x_1(t)}{1 - x_1(t - \tau_2(t))} [\frac{dF(x_1(t - \tau_2(t)))}{dx_1(t - \tau_2(t))} - \frac{1 - F(x_1(t - \tau_2(t)))}{1 - x_1(t - \tau_2(t))}] \tag{A.20}.$$

The other undefined first derivatives are equal to zero.

It is noticed that $J_{i,j} = 0$ $(j > 1)$ at steady states, which means RHS functions do not change with the delays and the average hematocrit at steady states. Therefore, the delays and the average hematocrit can be treated as constants for the use of DDE-BIFTOOL. The definition of the two node system is rewritten as

$$\frac{dx_1(t)}{dt} = -(\frac{d_B}{d_A})^6 k_2 H_1 \frac{\beta_A(\tilde{H}_A)}{\mu_B(\tilde{H}_B)} x_1^3(t) [\frac{F(x_1(t))}{x_1(t)} - \frac{F(x_1(t - \tilde{\tau}_1))}{x_1(t - \tilde{\tau}_1)}]$$
$$+ k_2 H_1 \frac{\beta_B(\tilde{H}_B)}{\mu_B(\tilde{H}_B)} x_1(t)(1 - x_1(t))^2 [\frac{1 - F(x_1(t))}{1 - x_1(t)} - \frac{1 - F(x_1(t - \tilde{\tau}_2))}{1 - x_1(t - \tilde{\tau}_2)}] \tag{A.21}$$

where $\tilde{H}_A$, $\tilde{H}_B$, $\tilde{\tau}_1$, $\tilde{\tau}_2$ are $\overline{H}_A$, $\overline{H}_B$, τ_1, τ_2 evaluated at steady states.

The first derivatives of the RHS functions

1) With respect to $x(t)$

$$J_{1,1} = -(\frac{d_B}{d_A})^6 k_2 H_1 \frac{\beta_A(\tilde{H}_A)}{\mu_B(\tilde{H}_B)} x_1^2(t)[\frac{dF(x_1(t))}{dx_1(t)} - \frac{F(x_1(t))}{x_1(t)}]$$

$$+ k_2 H_1 \frac{\beta_B(\tilde{H}_B)}{\mu_B(\tilde{H}_B)} x_1(t)(1 - x_1(t))[\frac{1 - F(x_1(t))}{1 - x_1(t)} - \frac{dF(x_1(t))}{dx_1(t)}]$$

(A.22)

2) With respect to $x(t - \tau_1(t))$

$$J_{1,1} = (\frac{d_B}{d_A})^6 k_2 H_1 \frac{\beta_A(\tilde{H}_A)}{\mu_B(\tilde{H}_B)} \frac{x_1^3(t)}{x_1(t - \tau_1(t))}[\frac{dF(x_1(t - \tau_1(t)))}{dx_1(t - \tau_1(t))} - \frac{F(x_1(t - \tau_1(t)))}{x_1(t - \tau_1(t))}] \quad \text{(A.23)}$$

3) With respect to $x(t - \tau_2(t))$

$$J_{1,1} = k_2 H_1 \frac{\beta_B(\tilde{H}_B)}{\mu_B(\tilde{H}_B)} \frac{x_1(t)(1 - x_1(t))^2}{1 - x_1(t - \tau_2(t))}[\frac{dF(x_1(t - \tau_2(t)))}{dx_1(t - \tau_2(t))} - \frac{1 - F(x_1(t - \tau_2(t)))}{1 - x_1(t - \tau_2(t))}] \quad \text{(A.24)}$$

● The three node network with two inlets and one outlet

Based on the same argument, the definitions are given by assuming constant delays in the two three node networks.

Let τ_1 denote τ_A, τ_2 denote τ_B, τ_3 denote τ_C, $\tau_4 = \tau_B + \tau_C$, $\Rightarrow$

$$\frac{dx_1(t)}{dt} = \frac{d_C^4}{l_C \mu_C(\tilde{H}_C)} \frac{4Q_1 H_1}{\pi} \frac{x_1(t)}{1 + \tilde{y}_{com}} \{-x_1^2(t) \frac{\beta_A(\tilde{H}_A)}{d_A^6}[\frac{F(x_1(t))}{x_1(t)} - \frac{F(x_1(t - \tilde{\tau}_1))}{x_1(t - \tilde{\tau}_1)}]$$

$$+ (1 + y_q - x_1(t))^2 \frac{\beta_B(\tilde{H}_B)}{d_B^6}[\frac{y_h + (1 - x_1(t))\frac{1 - F(x_1(t - \tilde{\tau}_3))}{1 - x_1(t - \tilde{\tau}_3)}}{1 + y_q - x_1(t)}$$

$$- \frac{y_h + (1 - x_1(t - \tilde{\tau}_2))\frac{1 - F(x_1(t - \tilde{\tau}_4))}{1 - x_1(t - \tilde{\tau}_4)}}{1 + y_q - x_1(t - \tilde{\tau}_2)}]$$

$$+ (1 - x_1(t))^2 \frac{\beta_C(\tilde{H}_C)}{d_C^6}[\frac{1 - F(x_1(t))}{1 - x_1(t)} - \frac{1 - F(x_1(t - \tilde{\tau}_3))}{1 - x_1(t - \tilde{\tau}_3)}]\}$$

(A.25)

where $\tilde{H}_A, \tilde{H}_B, \tilde{H}_C, \tilde{\tau}_1, \tilde{\tau}_2, \tilde{\tau}_3, \tilde{y}_{comb}$ are $\bar{H}_A, \bar{H}_B, \bar{H}_C, \tau_1, \tau_2, \tau_3, y_{com}$ evaluated at steady states.

99

APPENDIX A (CONTINUED)

The first derivatives of the RHS functions

1) With respect to $x(t)$

$$J_{1,1} = \frac{d_C^4}{l_C \mu_C(\tilde{H}_C)} \frac{4Q_1 H_1}{\pi(1 + \tilde{y}_{com})} \{-3x_1^2(t) \frac{\beta_A(\tilde{H}_A)}{d_A^6} [\frac{F(x_1(t))}{x_1(t)} - \frac{F(x_1(t - \tilde{\tau}_1))}{x_1(t - \tilde{\tau}_1)}]$$

$$-x_1^2(t) \frac{\beta_A(\tilde{H}_A)}{d_A^6} [\frac{dF(x_1(t))}{dx_1(t)} - \frac{F(x_1(t))}{x_1(t)}] + (1 + y_q - x_1(t))(1 + y_q - 3x_1(t)) \frac{\beta_B(\tilde{H}_B)}{d_B^6}$$

$$[\frac{y_h + (1 - x_1(t)) \frac{1 - F(x_1(t - \tilde{\tau}_3))}{1 - x_1(t - \tilde{\tau}_3)}}{1 + y_q - x_1(t)} - \frac{y_h + (1 - x_1(t - \tilde{\tau}_2)) \frac{1 - F(x_1(t - \tilde{\tau}_4))}{1 - x_1(t - \tilde{\tau}_4)}}{1 + y_q - x_1(t - \tilde{\tau}_2)}] \qquad (A.26)$$

$$+x_1(t) \frac{\beta_B(\tilde{H}_B)}{d_B^6} [y_h - y_q \frac{1 - F(x_1(t - \tilde{\tau}_3))}{1 - x_1(t - \tilde{\tau}_3)}] + (1 - x_1(t))(1 - 3x_1(t)) \frac{\beta_C(\tilde{H}_C)}{d_C^6}$$

$$[\frac{1 - F(x_1(t))}{1 - x_1(t)} - \frac{1 - F(x_1(t - \tilde{\tau}_3))}{1 - x_1(t - \tilde{\tau}_3)}] + x_1(t)(1 - x_1(t)) \frac{\beta_C(\tilde{H}_C)}{d_C^6} [\frac{1 - F(x_1(t))}{1 - x_1(t)} - \frac{dF(x_1(t))}{dx_1(t)}]\}$$

2) With respect to $x(t - \tau_1(t))$

$$J_{1,1} = \frac{d_C^4}{l_C \mu_C(\tilde{H}_C)} \frac{4Q_1 H_1}{\pi(1 + \tilde{y}_{com})} \frac{\beta_A(\tilde{H}_A)}{d_A^6} \frac{x_1^3(t)}{x_1(t - \tilde{\tau}_1)} [\frac{dF(x_1(t - \tilde{\tau}_1))}{dx_1(t - \tilde{\tau}_1)} - \frac{F(x_1(t - \tilde{\tau}_1))}{x_1(t - \tilde{\tau}_1)}] \qquad (A.27)$$

3) With respect to $x(t - \tau_2(t))$

$$J_{1,1} = \frac{-d_C^4}{l_C \mu_C(\tilde{H}_C)} \frac{4Q_1 H_1}{\pi(1 + \tilde{y}_{com})} \frac{\beta_B(\tilde{H}_B)}{d_B^6} x_1(t) [\frac{1 + y_q - x_1(t)}{1 + y_q - x_1(t - \tilde{\tau}_2)}]^2$$

$$[y_h - y_q \frac{1 - F(x_1(t - \tilde{\tau}_4))}{1 - x_1(t - \tilde{\tau}_4)}] \qquad (A.28)$$

4) With respect to $x(t - \tau_3(t))$

$$J_{1,1} = \frac{d_c^4}{l_C \mu_C(\tilde{H}_C)} \frac{4Q_1 H_1}{\pi(1 + \tilde{y}_{com})} \frac{x_1(t)(1 - x_1(t))}{1 - x_1(t - \tilde{\tau}_3)} [(1 + y_q - x_1(t)) \frac{\beta_B(\tilde{H}_B)}{d_B^6}$$

$$-(1 - x_1(t)) \frac{\beta_C(\tilde{H}_C)}{d_c^6}][\frac{1 - F(x_1(t - \tilde{\tau}_3))}{1 - x_1(t - \tilde{\tau}_3)} - \frac{dF(x_1(t - \tilde{\tau}_3))}{dx_1(t - \tilde{\tau}_3)}] \qquad (A.29)$$

5) With respect to $x(t - \tau_4(t))$

$$J_{1,1} = \frac{-d_C^4}{l_C \mu_C(\tilde{H}_C)} \frac{4Q_1 H_1}{\pi(1 + \tilde{y}_{com})} \frac{\beta_B(\tilde{H}_B)}{d_B^6} \frac{x_1(t)(1 - x_1(t))(1 + y_q - x_1(t))^2}{(1 - x_1(t - \tilde{\tau}_4))(1 + y_q - x_1(t - \tilde{\tau}_2))}$$

$$[\frac{1 - F(x_1(t - \tilde{\tau}_4))}{1 - x_1(t - \tilde{\tau}_4)} - \frac{dF(x_1(t - \tilde{\tau}_4))}{dx_1(t - \tilde{\tau}_4)}] \qquad (A.30)$$

100

APPENDIX B. DEFINITIONS FOR DDE-BIFTOOL WRITTEN IN MATLAB® SUBROUTINES

According to specification available from Report TW 330 (Engelborghs *et al.*, 2001), the required RHS functions and the first order derivatives of RHS functions presented in Appendix A need to be written in MatLAB® (Mathworks, Natick, MA)[i] subroutines for DDE-BIFTOOL. The MatLAB® subroutines as well as other required definitions are partially listed here.

● Two node networks

Here the subroutines for the two node topology are only given when delays are dealt with as state-dependent ones.

```
function [name,dim]=sys_init()
name='two_node';
dim=5;
path(path,'mypath\ddebiftool');
return;


function ntau=sys_ntau()
% xx: x1,x2,x1_tau1,x1_tau2,x3,x4,x5
% par: p,Hin,da,db,k1,k2
ntau=2;
return;


function tau=sys_tau(delay_nr,xx,par)
% xx: x1,x2(tau1),x3(tau2),x4,x5,x1_tau1,x1_tau2
% par: p,Hin,da,db,k1,k2
if delay_nr==1
    tau=xx(2,1);
elseif delay_nr==2
    tau=xx(3,1);
end;
return;


function dtau=sys_dtau(delay_nr,xx,par,nx,np)
% xx: x1,x2,x1_tau1,x1_tau2,x3,x4,x5
% par: p,Hin,da,db,k1,k2
%    dtau result of derivatives on delay function
dtau=[];
% first order derivatives wrt state variables:
if length(nx)==1 & length(np)==0
  if nx==0 % derivative wrt x(t)
    if delay_nr==1
```

```
        dtau(1:3)=0;
        dtau(2)=1;
    elseif delay_nr==2
        dtau(1:3)=0;
        dtau(3)=1;
    else
        dtau(1:3)=0;
    end;
  elseif nx==1 % derivative wrt x(t-tau1)
      dtau(1:3)=0;
  elseif nx==2 % derivative wrt x(t-tau2)
      dtau(1:3)=0;
  else
      dtau(1:3)=0;
  end;
% first order derivatives wrt parameters:
elseif length(nx)==0 & length(np)==1
    dtau(1:3)=0;
% second order derivatives wrt state variables:
elseif length(nx)==2 & length(np)==0
    dtau=zeros(3);
% mixed state parameter derivatives:
elseif length(nx)==1 & length(np)==1
    dtau(1:3)=0;
end;
if isempty(dtau)
    [delay_nr nx np]
    error('SYS_DTAU: requested derivative does not exist!');
end;
return;


function f=sys_rhs(xx,par)
% xx: x1,x2,x1_tau1,x1_tau2,x3,x4,x5
% par: p,Hin,da,db,k1,k2
x1=xx(1,1); x2=xx(2,1); x3=xx(3,1); x4=xx(4,1); x5=xx(5,1);
x1_tau1=xx(1,2); x1_tau2=xx(1,3);
p=par(1); Hin=par(2); da=par(3); db=par(4); k1=par(5); k2=par(6);
f(1,1)=-(db/da)^6*k2*Hin*dmu(x4,da)/mu(x5,db)*x1^3*(Fs(x1,p)/x1-Fs(x1_tau1,p)/x1_tau1)...
+k2*Hin*dmu(x5,db)/mu(x5,db)*x1*(1-x1)^2*((1-Fs(x1,p))/(1-x1)-(1-Fs(x1_tau2,p))/(1-x1_tau2
));
f(2,1)=1-x1/x1_tau1;
f(3,1)=1-(1-x1)/(1-x1_tau2);
```

f(4,1)=k1*Hin*x1*(Fs(x1,p)/x1-Fs(x1_tau1,p)/x1_tau1);
f(5,1)=k2*Hin*(1-x1)*((1-Fs(x1,p))/(1-x1)-(1-Fs(x1_tau2,p))/(1-x1_tau2));
return;

function J=sys_deri(xx,par,nx,np,v)
% xx: x1,x2,x1_tau1,x1_tau2,x3,x4,x5
% par: p,Hin,da,db,k1,k2
%   J result of derivatives on right hand side multiplied with v
J=[];
x1=xx(1,1); x2=xx(2,1); x3=xx(3,1); x4=xx(4,1); x5=xx(5,1);
x1_tau1=xx(1,2); x1_tau2=xx(1,3);
p=par(1); Hin=par(2); da=par(3); db=par(4); k1=par(5); k2=par(6);
% first order derivative discretisation parameters:
n=size(xx,1);
% first order derivatives wrt state variables
if length(nx)==1 & length(np)==0 & isempty(v)
    if nx==0 % derivative wrt x(t)
        J(1,1)=-(db/da)^6*k2*Hin*dmu(x4,da)/mu(x5,db)...
            *(3*x1^2*(Fs(x1,p)/x1-Fs(x1_tau1,p)/x1_tau1)+x1^2*(dFs(x1,p)-Fs(x1,p)/x1))...
            +k2*Hin*dmu(x5,db)/mu(x5,db)*((1-x1)*(1-3*x1)*((1-Fs(x1,p))/(1-x1)-(1-Fs(x1_tau2,p))/(
            1-x1_tau2))...
            +x1*(1-x1)*((1-Fs(x1,p))/(1-x1)-dFs(x1,p)));
        J(1,2)=0; J(1,3)=0;
        J(1,4)=-(db/da)^6*k2*Hin*ddmu(x4,da)/mu(x5,db)*x1^3*(Fs(x1,p)/x1-Fs(x1_tau1,p)/x1_tau
        1);
        J(1,5)=(db/da)^6*k2*Hin*dmu(x4,da)*dmu(x5,db)/mu(x5,db)^2*x1^3*(Fs(x1,p)/x1-Fs(x1_t
        au1,p)/x1_tau1)...
            +k2*Hin*(ddmu(x5,db)/mu(x5,db)-dmu(x5,db)^2/mu(x5,db)^2)*x1*(1-x1)^2 ...
                *((1-Fs(x1,p))/(1-x1)-(1-Fs(x1_tau2,p))/(1-x1_tau2));
        J(2,1)=-1/x1_tau1;
        J(2,2)=0; J(2,3)=0; J(2,4)=0; J(2,5)=0;
        J(3,1)=1/(1-x1_tau2);
        J(3,2)=0; J(3,3)=0; J(3,4)=0; J(3,5)=0;
        J(4,1)=k1*Hin*(dFs(x1,p)-Fs(x1_tau1,p)/x1_tau1);
        J(4,2)=0; J(4,3)=0; J(4,4)=0; J(4,5)=0;
        J(5,1)=k2*Hin*((1-Fs(x1_tau2,p))/(1-x1_tau2)-dFs(x1,p));
        J(5,2)=0; J(5,3)=0; J(5,4)=0; J(5,5)=0;
    elseif nx==1 % derivative wrt x(t-tau1)
        J(1,1)=(db/da)^6*k2*Hin*dmu(x4,da)/mu(x5,db)*x1^3/x1_tau1...
                *(dFs(x1_tau1,p)-Fs(x1_tau1,p)/x1_tau1);
        J(1,2)=0; J(1,3)=0; J(1,4)=0; J(1,5)=0;
        J(2,1)=x1/x1_tau1^2;

```
     J(2,2)=0; J(2,3)=0; J(2,4)=0; J(2,5)=0;
        J(3,1)=0; J(3,2)=0; J(3,3)=0; J(3,4)=0; J(3,5)=0;
        J(4,1)=k1*Hin*x1/x1_tau1*(Fs(x1_tau1,p)/x1_tau1-dFs(x1_tau1,p));
        J(4,2)=0; J(4,3)=0; J(4,4)=0; J(4,5)=0;
        J(5,1)=0; J(5,2)=0; J(5,3)=0; J(5,4)=0; J(5,5)=0;
     elseif nx==2 % derivative wrt x(t-tau2)
        J(1,1)=k2*Hin*dmu(x5,db)/mu(x5,db)*x1*(1-x1)^2/(1-x1_tau2)...
                *(dFs(x1_tau2,p)-(1-Fs(x1_tau2,p))/(1-x1_tau2));
        J(1,2)=0; J(1,3)=0; J(1,4)=0; J(1,5)=0;
        J(2,1)=0; J(2,2)=0; J(2,3)=0; J(2,4)=0; J(2,5)=0;
        J(3,1)=-(1-x1)/(1-x1_tau2)^2;
        J(3,2)=0; J(3,3)=0; J(3,4)=0; J(3,5)=0;
        J(4,1)=0; J(4,2)=0; J(4,3)=0; J(4,4)=0; J(4,5)=0;
        J(5,1)=k2*Hin*(1-x1)/(1-x1_tau2)*(dFs(x1_tau2,p)-(1-Fs(x1_tau2,p))/(1-x1_tau2));
        J(5,2)=0; J(5,3)=0; J(5,4)=0; J(5,5)=0;
     end;
return;


●   Three node networks with two inlets
```

Here the subroutines for the three node topology are only given when delays are dealt with as state-dependent ones.

```
function [name,dim]=sys_init()
name='three_node';
dim=1;
path(path,'mypath\ddebiftool');
return;


function ntau=sys_ntau()
% xx: x1,x1_tau1,x1_tau2,x1_tau3,x1_tau4
% par: p1,p2,H1,H2,Q1,Q2,da,db,dc,la,lb,lc,tau1,tau2,tau3,tau4,Qs
ntau=4;
return;


function tau=sys_tau(delay_nr,xx,par)
% xx: x1,x1_tau1,x1_tau2,x1_tau3,x1_tau4
% par: p1,p2,H1,H2,Q1,Q2,da,db,dc,la,lb,lc,tau1,tau2,tau3,tau4,Qs
if delay_nr==1
    tau=par(13);
elseif delay_nr==2
    tau=par(14);
elseif delay_nr==3
```

```
    tau=par(15);
elseif delay_nr==4
    tau=par(16);
end;
return;


function f=sys_rhs(xx,par)
% xx: x1,x1_tau1,x1_tau2,x1_tau3,x1_tau4
% par: p1,p2,H1,H2,Q1,Q2,da,db,dc,la,lb,lc,tau1,tau2,tau3,tau4,Qs
x1=xx(1,1);
x1_tau1=xx(1,2); x1_tau2=xx(1,3); x1_tau3=xx(1,4); x1_tau4=xx(1,5);
p1=par(1); p2=par(2); H1=par(3); H2=par(4);
Q1=par(5); Q2=par(6); da=par(7); db=par(8); dc=par(9);
la=par(10); lb=par(11); lc=par(12);
tau1=par(13); tau2=par(14); tau3=par(15); tau4=par(16);
Qs=par(17);
Has=H1*Fs(Qs,p1);
Hbs=(Q2*H2+Q1*H1*(1-Fs(Qs,p1)))/(Q2+Q1*(1-Qs));
Hcs=H1*(1-Fs(Qs,p1))/(1-Qs);
correctH(Has);
correctH(Hbs);
correctH(Hcs);
yq=Q2/Q1;
yh=H2*Q2/(H1*Q1);
ycombs=(1+yq)*mu(Hbs,db)*lb*dc^4/(mu(Hcs,dc)*lc*db^4);
f(1,1)=dc^4/(lc*mu(Hcs,dc))*4*Q1*H1/pi*x1/(1+ycombs)...
        *(-x1^2*dmu(Has,da)/da^6*(FsQs(x1,p1)-FsQs(x1_tau1,p1))...
        +(1+yq-x1)^2*dmu(Hbs,db)/db^6*((yh+(1-x1)*Fs_Qs(x1_tau3,p1))/(1+yq-x1)...
        -(yh+(1-x1_tau2)*Fs_Qs(x1_tau4,p1))/(1+yq-x1_tau2))...
        +(1-x1)^2*dmu(Hcs,dc)/dc^6*(Fs_Qs(x1,p1)-Fs_Qs(x1_tau3,p1)));
return;


function J=sys_deri(xx,par,nx,np,v)
% calculate the derivatives of rhs functions wrt state variables and par
% variables in the three node system
%     J result of derivatives on righthandside multiplied with v
% xx: x1,x1_tau1,x1_tau2,x1_tau3,x1_tau4
% par: p1,p2,H1,H2,Q1,Q2,da,db,dc,la,lb,lc,tau1,tau2,tau3,tau4,Qs
x1=xx(1,1);
x1_tau1=xx(1,2);
x1_tau2=xx(1,3);
x1_tau3=xx(1,4);
```

```
x1_tau4=xx(1,5);
p1=par(1); p2=par(2);
H1=par(3); H2=par(4); Q1=par(5); Q2=par(6);
da=par(7); db=par(8); dc=par(9);
la=par(10); lb=par(11); lc=par(12);
tau1=par(13); tau2=par(14); tau3=par(15); tau4=par(16);
Qs=par(17);
Has=H1*Fs(Qs,p1)/Qs;
Hbs=(Q2*H2+Q1*H1*(1-Fs(Qs,p1)))/(Q2+Q1*(1-Qs));
Hcs=H1*(1-Fs(Qs,p1))/(1-Qs);
correctH(Has); correctH(Hbs); correctH(Hcs);
yq=Q2/Q1; yh=H2*Q2/(H1*Q1);
ycombs=(1+yq)*mu(Hbs,db)*lb*dc^4/(mu(Hcs,dc)*lc*db^4);
% first order derivative discretisation parameters:
n=size(xx,1);
alpha=dc^4/(lc*mu(Hcs,dc))*4*Q1*H1/(pi*(1+ycombs));
% first order derivatives wrt state variables
if length(nx)==1 & length(np)==0 & isempty(v)
    if nx==0 % derivative wrt x(t)
        J(1,1)=dc^4/(lc*mu(Hcs,dc))*4*Q1*H1/(pi*(1+ycombs))...
        *(-3*x1^2*dmu(Has,da)/da^6*(FsQs(x1,p1)-FsQs(x1_tau1,p1))...
        -x1^2*dmu(Has,da)/da^6*(dFs(x1,p1)-FsQs(x1,p1))...
        +(1+yq-x1)*(1+yq-3*x1)*dmu(Hbs,db)/db^6*((yh+(1-x1)*Fs_Qs(x1_tau3,p1))/(1+yq-x1)...
        -(yh+(1-x1_tau2)*Fs_Qs(x1_tau4,p1))/(1+yq-x1_tau2))...
        +x1*dmu(Hbs,db)/db^6*(yh-yq*Fs_Qs(x1_tau3,p1))...
        +(1-x1)*(1-3*x1)*dmu(Hcs,dc)/dc^6*(Fs_Qs(x1,p1)-Fs_Qs(x1_tau3,p1))...
        +x1*(1-x1)*dmu(Hcs,dc)/dc^6*(Fs_Qs(x1,p1)-dFs(x1,p1)));
    elseif nx==1 % derivative wrt x(t-tau1)
        J(1,1)=dc^4/(lc*mu(Hcs,dc))*4*Q1*H1/(pi*(1+ycombs))*dmu(Has,da)/da^6*x1^3/x1_tau1...
        *(dFs(x1_tau1,p1)-FsQs(x1_tau1,p1));
    elseif nx==2 % derivative wrt x(t-tau2)
        J(1,1)=-dc^4/(lc*mu(Hcs,dc))*4*Q1*H1/(pi*(1+ycombs))*dmu(Hbs,db)/db^6*x1...
                *((1+yq-x1)/(1+yq-x1_tau2))^2*(yh-yq*Fs_Qs(x1_tau4,p1));
    elseif nx==3 % derivative wrt x(t-tau3)
        J(1,1)=dc^4/(lc*mu(Hcs,dc))*4*Q1*H1/(pi*(1+ycombs))*x1*(1-x1)/(1-x1_tau3)...
        *((1+yq-x1)*dmu(Hbs,db)/db^6-(1-x1)*dmu(Hcs,dc)/dc^6)*(Fs_Qs(x1_tau3,p1)-dFs(x1_tau
        3,p1));
    elseif nx==4 % derivative wrt x(t-tau4)
        J(1,1)=-dc^4/(lc*mu(Hcs,dc))*4*Q1*H1/(pi*(1+ycombs))*dmu(Hbs,db)/db^6...
        *x1*(1-x1)/(1-x1_tau4)*(1+yq-x1)^2/(1+yq-x1_tau2)*(Fs_Qs(x1_tau4,p1)-dFs(x1_tau4,p1));
    end;
    return;
```

106

APPENDIX C. APPLICATIONS OF SUCCESSIVE SUBSTITUTION METHODS IN FINDING CHARACTERISTIC ROOTS

Two numerical approaches can be applied to obtain the rightmost roots of the characteristic equations of the simple networks, i.e., eigenvalues of the dynamics of the systems. One is the successive substitution method (Rice and Do, 1994)[52]. The other is to utilize a MatLAB® package "DDE-BIFTOOL" to find out the rightmost eight values of the systems. The first method is discussed briefly here and its computational results are compared with those from DDE-BIFTOOL by an example in the two node network. Obviously, the characteristic equations in a form of (2.6.10) and (2.6.18) are nonlinear.

Since λ is a complex number, the equation

$$\lambda = \mathbf{F}(\lambda) \qquad (C.1)$$

can be manipulated into iteration forms as

$$r = f_1(r, \omega) \qquad (C.2)$$

$$\omega = f_2(r, \omega). \qquad (C.3)$$

r and ω are the real and imaginary part of the eigen value λ respectively. A well-known disadvantage of the successive substitution method is that there is no guarantee of convergence. By making some improvement, the equations (C.2) and (C.3) can be solved using the modified successive substitution method.

The computational approach is as follows:

1) Guess initial values $r^{(0)}, \omega^{(0)}$ and calculate $r^{(1)}, \omega^{(1)}$ from the iteration equation (C.2) and (C.3).

2) Repeating the above procedure and compute $\overline{r}, \overline{\omega}$ from $r^{(k)}, \omega^{(k)}$, where the superscript k denotes the iteration number.

3) If $\sqrt{\left|\overline{r} - r^{(k)}\right|^2 + \left|\overline{\omega} - \omega^{(k)}\right|^2} > \sqrt{\left|r^{(k)} - r^{(k-1)}\right|^2 + \left|\omega^{(k)} - \omega^{(k-1)}\right|^2}$, let $r^{(k+1)} = \overline{r}$,

$\omega^{(k+1)} = \overline{\omega}$ and go to step 2); otherwise, let $r^{(k+1)} = \phi\overline{r} + (1 - \phi)r^{(k)}$ and

$\omega^{(k+1)} = \phi\overline{\omega} + (1 - \phi)\omega^{(k)}$ to satisfy the inequality, where ϕ is a real number less than 1.

4) When both $r^{(n)}$ and $\omega^{(n)}$ converges satisfyingly, stop the computation and

return $r^{(n)}$ and $\omega^{(n)}$ as the final roots of the characteristic equation.

107

- Application in the two node network

Substitute $\lambda = r + i\omega$ into the characteristic equation (2.6.10) $\Rightarrow$

$$r + i\omega = -b - c + be^{-\gamma(r+i\omega)} + ce^{-(r+i\omega)} \qquad (C.4)$$

$$\Rightarrow (1+\alpha) + i\beta = e^{-\gamma r}e^{-i\gamma w} \qquad (C.5)$$

where $\alpha = \dfrac{r}{b} + \dfrac{c}{b} - \dfrac{c}{b}e^{-r}\cos\omega$ and $\beta = \dfrac{\omega}{b} + \dfrac{c}{b}e^{-r}\sin\omega$.

From the nature of complex numbers $\Rightarrow$

$$r = -\frac{1}{2\gamma}\ln[(1+\alpha)^2 + \beta^2] \qquad (C.6)$$

$$\omega = -\frac{1}{\gamma}\arctan(\frac{\beta}{1+\alpha}) \qquad (C.7)$$

The equations (C.6) and (C.7) are applied to perform the successive substitution method.

Although we have the iteration forms on hand, how to guess good initial values remains an issue. If λ_0 at γ_0 is available, λ_0 is used as an initial one for computing λ_1 at γ_1. Finally, λ at $\gamma_m = \gamma$ can be obtained by repeating the process with increasing γ, where $\lambda_k = k\Delta\lambda$, $k \in \square$.

Especially, at $\gamma = 0$, the equation (2.6.10) is reduced to

$$\lambda = -c + ce^{-\lambda} \qquad (C.8)$$

Let $\lambda' = \lambda + c$ and $c' = ce^c$, the equation (C.8) is rewritten as

$$\lambda' = c'e^{-\lambda'}. \qquad (C.9)$$

Replace $\lambda' = r' + i\omega'$ into (C.9) $\Rightarrow$

$$r' = -\omega / \tan\omega \qquad (C.10)$$

$$\omega' = |c| e^{\omega'\cot\omega'} / \sqrt{1 + \cot^2\omega'} \quad . \qquad (C.11)$$

The above two equations can be solved to get λ' using graphical methods without difficulties, and consequently lead to λ at $\gamma = 0$.

108

● Application in the three node network

Substitute $\lambda = r + i\omega$ into the characteristic equation (2.6.18) and conduct several algebraic manipulations. ⇒

$$r = -\frac{1}{2\gamma}\ln[(1+\alpha)^2 + \beta^2] \qquad\qquad (C.12)$$

$$\omega = -\frac{1}{\gamma}\arctan(\frac{\beta}{1+\alpha}), \qquad\qquad (C.13)$$

where $\alpha = \frac{\kappa_1\kappa_3 - \kappa_2\kappa_4}{\kappa_1^2 + \kappa_2^2}$, $\beta = \frac{\kappa_2\kappa_3 + \kappa_1\kappa_4}{\kappa_1^2 + \kappa_2^2}$, and $\kappa_1 = d + ae^{-r}\cos\omega$, $\kappa_2 = ae^{-r}\sin\omega$,

$\kappa_3 = r - be^{-r\gamma}\cos(\omega\gamma) - ce^{-r}\cos\omega + b + c$, $\kappa_4 = \omega + be^{-r\gamma}\sin(\omega\gamma) + ce^{-r}\sin\omega$.

Like the two node situation, good initial value of λ is preferred while using the iteration form (C.12) and (C.13). Similarly, if λ_0 at δ_0 is available, λ at $\delta_m = \delta$ can be obtained by the modified successive substitution method with increasing δ, where

$$\lambda_k = k\Delta\delta, \quad k \in \mathbf{N}^1.$$

Especially, at $\delta = 0$, the equation (2.6.18) is reduced to

$$\lambda = -(b+c) + be^{-\gamma\lambda} + ce^{-\lambda}, \qquad\qquad (C.14)$$

which is the same as (2.6.10), thus the procedures used in the last part can be applied to compute the initial value of λ at $\delta = 0$.

● Comparison between results from the successive substitution method and DDE-BIFTOOL

In the application of successive substitution methods, the DDEs are linearized and normalized around steady states to generate characteristic equations; while in the DDE-BIFTOOL, the characteristic equations are derived from linearized DDEs directly. Thus, some correlations exist between the eigenvalues found from the two methods, which is shown in the below example.

The investigated system is the two node network with Pries's *in vitro* viscosity model and Logit plasma skimming model. The physical parameters are

$$(p, H_1, Q_1, d_A, d_B, l_A, l_B) = (2.0, 0.80, 10^5, 35, 20, 50, 250).$$

The unit of diameters and are μm, those of lengths are mm, and the unit of flow rate is μm³/sec.

It is found at the steady state,

$$\tilde{Q} = 0.77033, \quad \tilde{\tau}_A = \frac{\pi}{4} d_A^2 l_A / Q_1 \tilde{Q} = 0.62448 \text{sec}, \tilde{\tau}_B = \frac{\pi}{4} d_B^2 l_B / Q_1 (1 - \tilde{Q}) = 3.4197 \text{sec}.$$

$$\gamma = \tilde{\tau}_A / \tilde{\tau}_B = 0.18257$$

and

$$b = -6.63193, c = 0.33104.$$

Solve the characteristic equation Eq.(C.14)

$$\lambda = -(b + c) + b e^{-\gamma \lambda} + c e^{-\lambda}$$

using the successive substitution method $\Rightarrow$ $\lambda = 0.24882 \pm 1.83747 i$.

In the application of DDE-BIFTOOL, it is calculated that $A_0 = 1.8419$, $A_1 = -1.9388$, $A_2 = 0.0968$ in the characteristic equation

$$\lambda = A_0 + A_1 e^{-\lambda \tau_A} + A_2 e^{-\lambda \tau_B}, \tag{C.15}$$

and the rightmost roots are $\lambda = 0.07260 \pm 0.5379 i$ generated from the DDE-BIFTOOL.

Check the relationship between the two methods,

$$\lambda = A_0 + A_1 e^{-\lambda \tau_A} + A_2 e^{-\lambda \tau_B}$$

$$\underset{\lambda \tau_B = \lambda'}{\Leftrightarrow} \frac{\lambda'}{\tau_B} = A_0 + A_1 e^{-\frac{\lambda'}{\tau_B} \tau_A} + A_2 e^{-\frac{\lambda'}{\tau_B} \tau_B} \tag{C.16}$$

$$\underset{\gamma = \tau_A / \tau_B}{\Leftrightarrow} \lambda' = A_0 \tau_B + A_1 \tau_B e^{-\lambda' \gamma} + A_2 \tau_B e^{-\lambda'} \tag{C.17}$$

$$\underset{A_0 \tau_B = -(b+c) \quad A_1 \tau_B = b \quad A_2 \tau_B = c}{\Leftrightarrow} \lambda' = -(b + c) + b e^{-\lambda' \gamma} + c e^{-\lambda'}. \tag{C.18}$$

Coefficents b, c, γ, A_0, A_1, A_2 and rightmost eigenvalues λ and λ' are listed in the Table C.1. From the table, it is found that eigenvalues generated from the two methods are inherently equal to each other.

Table C.1   Compare Results Generated from Successive Substitution Methods and DDE-BIFTOOL Package

| DDE-BIFTOOL Package	Successive Substitution Methods
$A_0 \tau_B = 6.29874$	$-(b + c) = 6.30068$
$A_1 \tau_B = -6.63011$	$b = -6.63193$
$A_2 \tau_B = 0.33103$	$c = 0.33104$
$\text{Re}(\lambda) \tau_B = 0.2483$	$\text{Re}(\lambda') = 0.2489$
$\text{Im}(\lambda) \tau_B = 1.839$	$\text{Im}(\lambda') = 1.838$

110

APPENDIX D. SOFT LITHOGRAPHY PROCEDURE FOR MANUFACTURING SIMPLE MICROVASCULAR NETWORKS

Soft lithography approach has been under rapid development over the past decade, which can be used to generate micro-structures with critical dimensions of about 30nm to 500μm. (Y. Xia and G. M. Whitesides, 1998)[38]. Compared with traditional photolithography used in microelectronics, the soft lithography is a low cost and simple technique, and it is ideal for common laboratories to carry out. Several soft lithography techniques can be used to construct microchannels. Among these techniques, a strategy called rapid prototyping is less expensive and has a quicker turn-around-time, which is suitable to develop systems with feature sizes greater or equal to 20μm.

Some experiments have been conducted to fabricate *in vitro* replicas of two node networks and three node networks (see Figure 2.2 and Figure 2.3). A general procedure for manufacturing the simple microvascular networks via rapid prototyping techniques are stated briefly as following.

1) Design patterns

Desired patterns were drawn by using Adobe® Illustrator® (Adobe, San Jose, CA), which were save in high quality Portable Document Format (PDF) files. Negative images of designed patterns for the two node network and the three node network are demonstrated in Figure D.1 and Figure D.2 respectively.
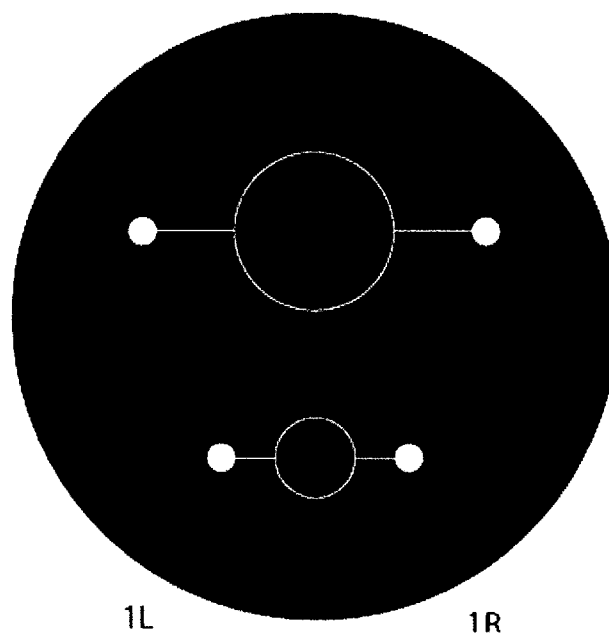
Figure D.1 A Negative Image Showing Two Node Network Patterns

111

APPENDIX D   (CONTINUED)

7L   7R
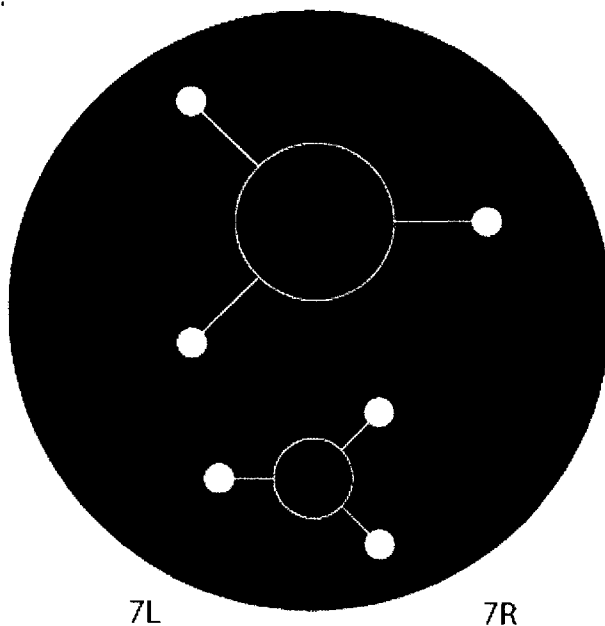
Figure D.2   A Negative Image Showing Three Node Network Patterns

These patterns are shown here as their actual sizes. Dimensions of each image are equal to those of a silicon substrate with diameter about 3.2 inches. Each image presents two same patterns but different dimensions. The bigger one includes microchannels with 50μm width and the smaller one includes the ones with 35μm width.

2) Prepare mask

The saved PDF files were sent to PageWorks Company (PageWorks, Cambridge, MA)[ii]. The files were then printed onto transparent as positive films on a 5080 dpi laser printer. A positive film displays the images in black with a clear background. Usually, eight images may be included on a 9" x 12" sheet, and a cost of each sheet is $47.95.

After the transparent with designed images were ready, a desired image was cut off from a sheet for use in the following step.

3) Fabricate master

Negative photoresist SU-8 2000[iii,iv] (MicroChem, Newton, MA)[v] was used to fabricate masters. A normal process of applying SU-8 2000 can be found in process guidelines provided by MicroChem, Inc..[vi] Roughly, the process consists of steps such as pretreating substrate, spin coating, soft baking, exposure under UV, post expose baking (PEB), developing, and follow-up steps.

This fabrication process began with cleaning a silicon substrate (diameter ≈3.2 inches) with acetone, isopropyl alcohol (IPA), and ethanol. After the substrate was dry, it was put into 40% NaOH solution to treat the smoother surface for about ten minutes. The substrate was then washed with water and baked in an oven (temperature 60 – 70 °C) to remove moisture.

112

The substrate was placed on a spin coater with the smoother face up, and around 3mL photoresist was poured directly on to the surface. To obtain channels with desired 50μm depth, spin speeds were set to be 500 RPM for 7 seconds and 2000RPM for next 30 seconds.

The substrate with coated photoresist was heated in the oven (temperature 60 – 70 °C) for 3 minutes and then in another oven (temperature 90 – 100 °C) for 15 minutes.

A prepared negative film was put on the substrate and covered by a large glass slides (around 0.25 inches thickness) to keep them in place, and they were placed below a UV light source (Chemical Engineering Department, UNH, Dr. Nivedita Gupta). The exposure time was 4 x 20 seconds, and the substrate was rotated 90 degrees every 20 seconds to ensure uniform exposure.

PEB was done in the oven (temperature 60 – 70 °C) for 3 minutes and then in the oven (temperature 90 – 100 °C) for 5 minutes.

The substrate was placed in SU-8 developer after PEB. The developing time was approximately ten minutes and probably longer until white film on the master was gone. The substrate was rinsed by IPA and then heated to be dry, and a pattern master was obtained.

4) Make stamps

Silicon polydimethylsiloxane (PDMS) (Dow, Sylgard 184 Elastomer) were mixed with a curing agent (Dow, Sylgard 184 Elastomer Curing Agent) at a 10:1 ratio. The master was placed in a Petri dish. After all bubbled were removed in a vacuum oven, approximate 6 mL PDMS solution was poured over the master to form a thin layer. The Petri dish was placed in the vacuum oven to remove possible bubbles, and then it was placed in the oven (temperature 60 – 70 °C) for about 1 hour or until fully cured. When the PDMS layer was peeled off the master, a stamp with etched channels in desired pattern were obtained.

5) Finish models

The obtained stamp needed to be sealed before experimental uses. A hole puncher was used to punch out wells as entrances or exits for fluid on the stamp. A second layer was cured for 30 minutes and them the stamp was placed on its top with channels face down. The two layers were heated for around 60 minutes until they were bonded tightly. A third layer was used to seal the wells by repeat the preceding steps. Tiny plastic tubes were then inserted into the wells to create entrances and exits. Drops of PDMS solution were then placed on the joints, and the PDMS model was heated for about 1 hour to seal the joints.

6) Check sealing and connectivity

After the PDMS models were finished, a syringe filled with water was used to check the sealing and connectivity of the models under an Olympus BHS microscope (Olympus Optical, Tokyo, Japan). Any models with leaks or poor connectivity were discarded.

Images of microchannels with designed 50μm width and 35μm width are shown in Figure D.3 and Figure D.4. It is found that the actual sizes are equal to 90$\pm$2μm and 65$\pm$2μm. Several factors may be potential reasons leading to deviation of sizes, such as the exposure time under UV, baking time, and the PEB time. Future adjustment needs to be done on the process parameters to achieve optimal results.
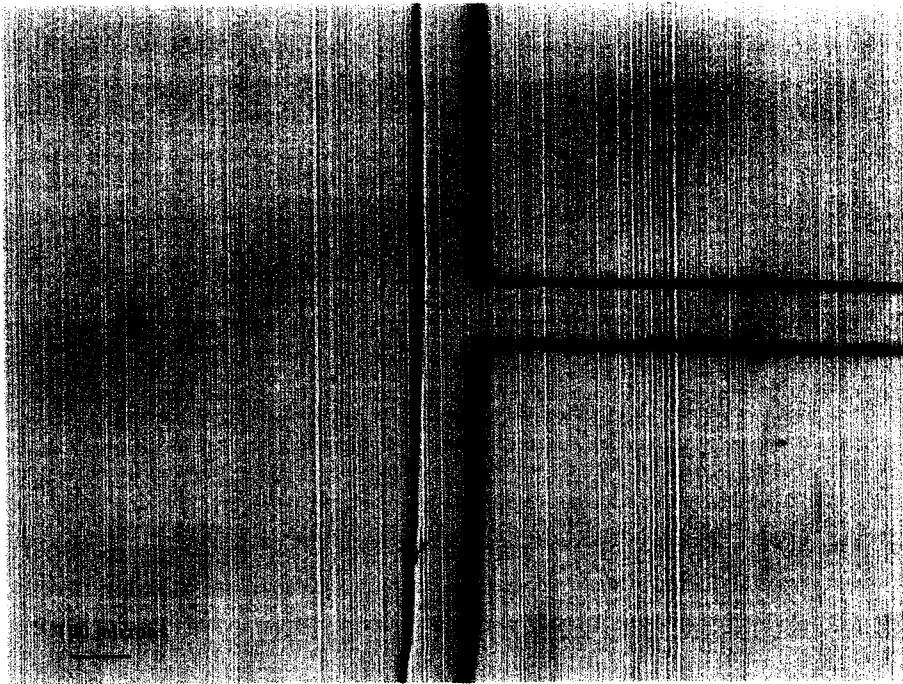
Figure D.3   An Image of Microchannels with 90±2μm Width.
The designed width is 50μm.
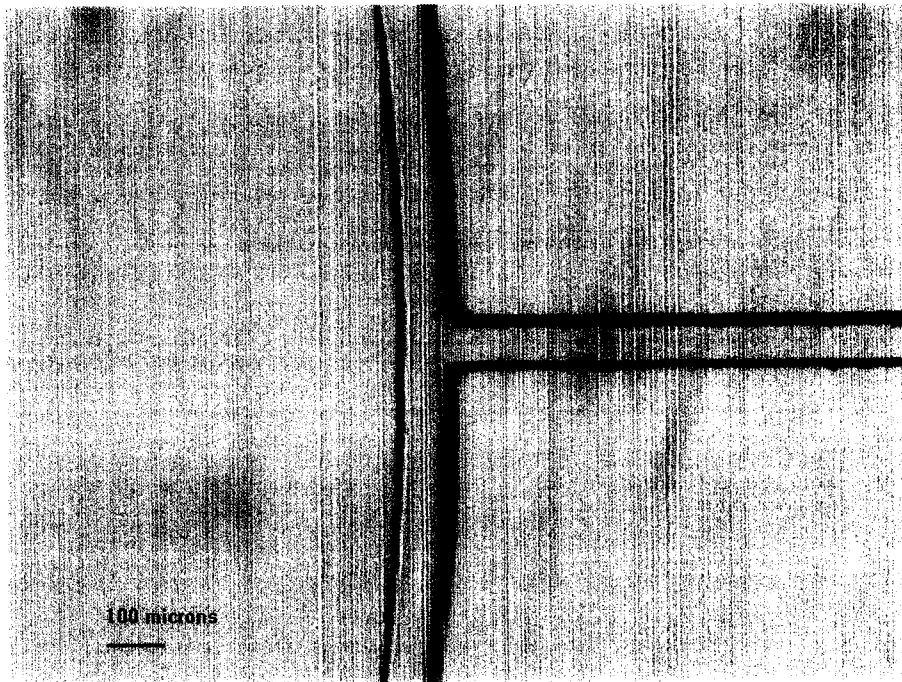
Figure D.4   An Image of Microchannels with 65±2μm Width.
The designed width is 35μm.

114

i.   http://www.mathworks.com/

ii.   http://www.pageworks.com/

iii.   http://www.microchem.com/resources/su8_process_capability_paper_1.pdf

iv.   http://www.microchem.com/resources/su8_process_capability_paper_2.pdf

v.   http://www.microchem.com/

vi.   http://www.microchem.com/products/pdf/SU8_2035-2100.pdf